

UNIVERSITÀ DEGLI STUDI DI ROMA “TOR VERGATA”
Facoltà di Scienze Matematiche Fisiche e Naturali

Dottorato di Ricerca in Fisica
Ciclo: XXVII

Fragmentation measurements with the **FIRST** experiment

Marco Toppi

Relatore Interno:

Prof.ssa Annalisa D'Angelo

Relatore Esterno:

Prof. Vincenzo Patera

Coordinatore di dottorato:

Prof. Maurizio De Crescenzi

Anno Accademico 2014/2015

Contents

Foreword	v
1 Interaction of ions in matter for particle therapy applications	1
1.1 Radiotherapy and particle therapy: an introduction	1
1.1.1 Biological aspects for particle therapy	4
1.2 Physics for particle therapy	8
1.2.1 Stopping power of high energy ions	8
1.2.2 Range	12
1.2.3 Energy and Range Stragglng	14
1.2.4 Multiple scattering	15
2 Nuclear fragmentation	19
2.1 Hadronic interactions and nuclear fragmentation processes	19
2.2 Hadronic interaction models in FLUKA	22
2.2.1 Hadron-nucleon (h-N) interactions	23
2.2.2 Hadron-nucleus (h-A) interactions	23
2.2.3 Nucleus-nucleus (A-A) interactions	28
2.3 Fragmentation cross sections measurements and benchmarking with MC	31

2.4	Nuclear fragmentation effects in particle therapy applications	37
3	The FIRST experiment	41
3.1	The experimental setup	42
3.1.1	The Start Counter	47
3.1.2	The Beam Monitor	48
3.1.3	The Vertex Detector	50
3.1.4	The ALADIN magnet	55
3.1.5	The ToF-Wall detector	55
3.2	The DAQ and the trigger	66
3.3	The Monte Carlo simulation	68
3.4	The data/MC reconstruction	71
4	FIRST Analysis	73
4.1	The reconstruction algorithm	74
4.1.1	Global tracking	74
4.1.2	Improving the Z_{ID} algorithm with VTX cluster size	77
4.1.3	Rating of the candidate tracks	79
4.1.4	TW hits clustering	81
4.2	Tracking algorithm performances	82
4.2.1	The angular and kinetic energy resolutions	83
4.2.2	The tracking efficiencies	86
4.2.3	Kinetic energy distribution unfolding	86
4.3	Cross section measurements	88
4.3.1	Combinatorial background evaluation	89
4.3.2	Fragment yield measurement	90
4.3.3	Cross feed evaluation	91

4.3.4	Cross sections results	94
4.4	Systematic uncertainties	100
5	A possible upgrade for the FIRST detector	105
5.1	A possible upgrade of the FIRST setup: the FINUDA drift chambers	107
5.1.1	Monte Carlo Simulation	109
5.1.2	FINUDA drift chambers test with cosmic rays	111
5.1.3	Final considerations	119
	Conclusions	121
	A Isotopic cross sections	125
	Bibliography	135

Foreword

The study of the nuclear fragmentation processes occurring in the interaction of highly energetic ions in matter is of great interest both in basic research (e.g. to improve the understanding of hadronic showers development in the atmosphere) and in applied physics, in particular in cancer therapy and space radiation protection fields. For these applications accurate fragmentation cross section measurements are needed to develop radiation treatment planning for tumor therapy and particles transport codes in shielding materials to estimate health risks for human missions in space.

The use of light ion beams ($Z \leq 10$) and in particular carbon ions to treat tumors (particle therapy or hadrontherapy) is motivated by a highly localized dose deposition pattern and a higher biological efficiency with respect to the conventional radiotherapy with photons [1]. In fact charged particles, slowing down in matter, release the great part of their energy at the end of their path in a very narrow region, due to the electromagnetic interactions with the atomic electrons: this highly localized energy deposition is called Bragg peak [2]. However, ion beams in the energy range from tens of MeV/nucleon to hundreds of MeV/nucleon, undergo inelastic nuclear reactions in patient tissue and produce a significant yield of secondary fragments: only $\sim 50\%$ of the heavy ions directed to the patient actually reach a deep tumor due to the fragmentation process [3].

Since the fragments have higher ranges and larger angular distributions with respect to primary ions, they produce a tail of damaging ionization beyond the Bragg peak. So the fragmentation process modifies the delivered dose map in patient's

body with respect to that one due only to primary ions radiation. Since the standard accuracy of a radiotherapy on the release dose is of the order of 3% [4], it's evident that a more precise knowledge of the dose map due to the fragments mixed radiation fields is of fundamental importance in order to achieve the needed dose control, especially when treating tumors nearby organs at risk.

High precision measurements of nuclear fragmentation cross sections, in the range of therapeutic energies (up to 400 MeV/nucleon for ^{12}C ion projectiles), are essential to achieve such accuracy in treatment planning, allowing an accurate prediction of fragments fluences and a precise simulation of the spatial dose distribution in the patient's body.

The nuclear fragmentation studies in the energy range of 100-1000 MeV/nucleon are of interest also for radiation protection in human space flight. The nuclear fragmentation properties of the materials used in the spacecrafts need to be known with high accuracy in order to provide the required shielding of the astronauts against the cosmic radiation [5]. The space radiation can also affect the stability of electronic devices on long duration space missions, causing Single Event Effects (SEE) that can damage electronics systems and instrumentations [6]: also these effects are modulated by the fragmentation of the cosmic radiation on the materials surrounding the electronics.

The stable source of radiation in space are galactic or extragalactic Cosmic Rays (CR). CR consist of protons and heavier nuclei emitted from supernovae within our galaxy or by highly energetic extragalactic objects: the peak of CR spectrum is in the GeV range, but has a long tail up to the highest energies in the ZeV region (10^{21} eV). Occasionally a stochastic burst of radiation from the sun, called Solar Particle Event (SPE), can happen. The radiation produced during SPE consists essentially of protons and light ions emitted from the Sun during coronal mass ejection (CME) or solar flares with energies up to few GeV.

Carbon ions are a significant component of both CR and SPE. When the incident radiation interacts with the spacecraft hull and internal materials, nuclear fragmentation modifies the composition of CR and SPE spectra, producing a build-

up of secondary fragments. This process must be taken into account to minimize the dose delivered to astronauts as well as to prevent damages to electronic systems and instrumentations.

In the quoted applications complex computations are needed to obtain dose release in patient or shielding efficiency in space. Key ingredients of these calculations are the algorithms that describes the transport of particles in matter. These algorithms can be implemented either by using deterministic codes, based on Boltzmann-type transport equations, or by using Monte Carlo (MC) codes that sample the interaction process on a event-by-event basis. Both approaches rely on the achieved precision of the nuclear interaction cross sections measurements.

MC particles transport codes are valuable tools to predict ions radiation fields in tissue and to calculate fluences and dose distribution in patient-like geometries. At the moment MC codes cannot be extensively used for treatment planning optimization, as they are currently too time consuming, so treatment plans are generally based on deterministic codes [7, 8, 9], but the great accuracy required makes necessary several inter-comparisons of the codes with MC calculations [10, 11, 12, 13, 14].

The nuclear interaction models, used by these MC codes, have been developed using measured nuclear fragmentation cross sections of light ions in water or tissue-equivalent materials, mostly performed in USA (LBL-Berkeley), Japan (HIMAC-Chiba) and Germany (GSI) [15]. The agreement between predictions of nuclear reaction models implemented in transport codes and experimental data is encouraging but there is room for improvement, mainly due to the lack of available data and to their limited precision. So far, only yields or total and partial charge-changing fragmentation cross sections have been measured with high precision and in a variety of target and beam energy configurations, while the most valuable results, the double differential cross section (DDCS) measurements, that would allow a stringent test of the nuclear model predictions, are still missing.

In particular, while the fluences and the total cross sections are well described by current computer codes, the production of light fragments and their angular distribution is affected by large uncertainties and different algorithms currently yield

prediction that can differ up to an order of magnitude [16].

Similar problems are found in the algorithms used for space radiation transport in shielding materials: despite the large data sample that can provide several measurements of the fragmentation cross sections in the range of interest of space radioprotection (reviewed in [5]), the MC simulations of angular distributions are not yet reproduced with the required precision. The same is also true when studying the production of different He isotopes, mesons, and γ -rays. NASA recently completed a survey of a large data base [17] of measured nuclear fragmentation cross sections including approximately 50000 datasets, and concluded that several experimental data are missing, including DDCS for carbon ions at energies below 400 MeV/nucleon, which are those needed also for improving treatment planning in therapy.

Accurate measurements of DDCS of light ions in the energy range 100–1000 MeV/nucleon are, hence, urgently needed to improve nuclear interaction models. In order to provide the necessary information to MC simulations a small set of measurements is needed: the interpolation of DDCS for different energies and composition of target materials allows, starting from a selected number of target/energy combinations, to build a model covering all the application needs. Two measurements of single and double differential fragmentation cross sections of carbon ions on different thin targets have been performed recently in this framework at LNS [18] and GANIL [19, 20], at 62 MeV/nucleon and 95 MeV/nucleon beam energies respectively.

The FIRST (Fragmentation of Ions Relevant for Space and Therapy) experiment at the Helmholtz Center for Heavy Ion research (GSI) was designed and built by an international collaboration from France, Germany, Italy and Spain in order to perform precise measurements of the fragmentation cross sections of a ^{12}C ion beam with different thin targets. The experiment main purpose is to measure the fragmentation DDCS at different angles and energies between 100 MeV/nucleon and 1000 MeV/nucleon [21]. The FIRST scientific program start was on summer 2011 at the GSI laboratory and was focused on the measurement of 400 MeV/nucleon ^{12}C beam fragmentation on thin targets.

The Phd thesis presented here documents the work performed within the FIRST collaboration. The research work was focused on the analysis of data collected for the interaction of a ^{12}C beam at 400 MeV/nucleon on the thin targets. In particular I have dealt with the calibration of some detectors of the FIRST apparatus, the charge identification algorithm, the tracks reconstruction and the background studies. The results of this analysis work are the differential fragmentation cross sections, here presented, measured as a function of the fragment angle and kinetic energy in the forward angular region ($\theta \lesssim 6^\circ$). Furthermore, I have also studied a possible upgrade of the FIRST experimental apparatus with an improved detector setup to enhance the fragments reconstruction and identification performances. In chapter 1 an introduction to particle therapy will be given and the mechanisms of interaction of ions with matter will be reviewed with a particular focus on the energy range of interest for particle therapy applications. Chapter 2 will deal with the nuclear fragmentation models and measurements. In chapter 3 the FIRST apparatus and the detector calibration strategies will be described. In chapter 4 the analysis techniques used for the reconstruction of fragment tracks in the forward angular region of FIRST and the results of the elemental and isotopic single differential cross sections with respect to angle and energy will be discussed. Finally, in chapter 5, a possible upgrade of the FIRST apparatus will be proposed.

Chapter 1

Interaction of ions in matter for particle therapy applications

1.1 Radiotherapy and particle therapy: an introduction

The current knowledge about matter and the fundamental interactions has been allowed by the development of particle accelerators of higher and higher energies.

Since the X-rays discovery by W.C. Roentgen in 1895, the affinity between technologies developed as a tool for fundamental research and medical applications has been evident: shortly after their discovery, X-rays were also used as a tool for the treatment of malignant tissues [22]. This started from the X-rays tubes in the first years of 1900 and nowadays proton and light ions accelerators present a major interest in the medical application field, in particular for the radiation oncology.

Nowadays radiotherapy is widely used all around the world and plays an important role in the treatment of cancer. After surgery it is the most frequently and most successfully applied form of therapy. More than 50% of all patients with localized malignant tumors are treated with radiation. However the total cure rate, obtained by using combinations of different therapeutic means (the surgery, the chemiother-

apy and the radiotherapy) is just around 45%. The main reasons for the failure of the treatments for the 55% of the patients, are the lack of local control on the tumor and the development of metastases.

The X-rays therapy, or radiotherapy, is used in clinical practice since the seventies. In the radiotherapy development the clinical results improved whenever a better conformity of the applied radiation to the target tumor volume and an increased biological effectiveness of the radiation could be achieved.

In radiotherapy the most critical part related to the patient treatment planning is the dose (energy released per mass unit) delivery. The treatment has to be planned in such a way that the target volume receives the dose needed to kill the tumor cells, while the surrounding healthy tissues have to be spared as much as possible. In the conventional radiotherapy the beams are made by (6 - 25) MeV photons, and the energy deposition of the beam in the patient tissues follows an exponential law. The healthy tissues on the path of the photon beam to the tumor are unavoidably hit. Fig. 1.1 shows the dose deposition induced by different projectiles with respect to the penetration depth in liquid water. The previously discussed effect is particularly severe in case of low energy X-rays dose profile that shows a steep exponential decrease with depth, with a maximum of the deposition located at a small penetration depth, near the entrance surface. In the past 50 years many progresses have been made to improve dose delivery towards the ideal situation and to thereby increase the tumor control rate. In order to overcome the limitations of an exponentially decreasing depth dose distribution of electromagnetic radiation numerous techniques have been developed and applied.

To reduce the dose to the healthy tissues in front of the target volume, the energy of the photons was increased for the treatment of deep-seated tumors. The originally used X-rays tubes were replaced by high energy gamma rays, after ^{60}Co sources could be produced in nuclear reactors (gamma rays of 1.17 MeV and 1.33 MeV). Years later, the ^{60}Co sources have been replaced by compact linear accelerators which deliver high energy X-rays and gamma rays. In these devices electrons are accelerated and sent to a conversion target: photons are produced by the bremsstrahlung process induced by the slowing down of the high energy electrons in the conversion target.

CHAPTER 1. INTERACTION OF IONS IN MATTER FOR PARTICLE THERAPY APPLICATIONS

The resulting photons beam has an energy of about 15-20 MeV that delivers a radiation dose in the patient that slows down exponentially after a maximum shifted of some centimeters from the input surface. For these high energy photons (mostly used in conventional therapy nowadays) the initial dose build-up is mainly caused by forward scattered Compton electrons that transport some of the transferred energy from the surface to greater depth yielding an increase in dose in the first few centimeters. In this way the maximum delivered dose is distant respect to the patient skin that is particularly photo-sensitive, saving it by radiation damage. In addition, the exponential decay becomes less steep improving the ratio of entrance dose to target dose for the treatment of deep-seated tumors. An important improvement

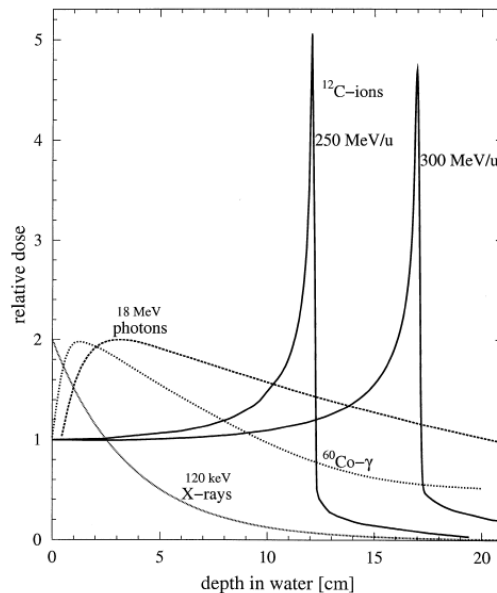


Figure 1.1: Dose profile for different photons and carbons beams energies [22]

has been given by the Intensity Modulated Radio Therapy (IMRT), that uses 6-10 X-rays beams and multi-leaf collimators in order to conform the irradiation field to the external shape of the tumor. The intensity and the direction of each beam are optimized according to a complex system of software named TPS (Treatment Planning System).

While the potential of X-rays for treating cancer was recognized soon after their discovery in 1895, it was not until 1946 that Robert R. Wilson proposed that high energy beams of heavy charged particles like protons and light ions could be used for localized cancer therapy, thank to their favorable tissue depth-dose distribution. In fact he investigated the depth dose profile of protons produced at the Berkeley cyclotron and observed a steep increase of energy deposition i.e. of dose at the end of the particle range [23]. This increase in ionization density had been already measured in 1903 by Bragg for alpha particle in air and is known as Bragg profile [2]. The increase in ionization density towards the end of the particle trajectory allows to transport a higher dose to a deep seated tumor than would be possible using conventional photons beams: differently from photons charged particles deposit little energy at the body's surface (from 10% to 20% of the maximum), when their velocity is high, and instead deposit most of their energy just before they come to rest.

Calibrating the initial energy of the beam is possible to change the range of the beam in the patient and then to deliver the dose at different depths: the location of the maximum of the dose deposition, the Bragg peak, depends on the particle incident energy. In Fig. 1.1 the dose profiles of two ^{12}C -ions beams with initial kinetic energy of 250 MeV/nucleon and 300 MeV/nucleon are shown. Since the Bragg peak for particles of a given energy is very narrow, different beam energies are necessary to fill the volume of a tumor: the plateau resulting from the combination of different beam energies is called the Spread Out Bragg Peak (labeled SOBP), as illustrated in Fig. 1.2. In that case, the dose deposition before the SOBP may be quite large (more than 50% of the maximum) depending on the size of the tumor and the number of beams used to paint it. The therapy that uses charged particles beams to irradiate malignant tissues is called particle therapy, to distinguish it from the traditional X-rays and γ -rays therapy, usually called just radiotherapy.

1.1.1 **Biological aspects for particle therapy**

A great advantage of the particle therapies is given by the biological effects induced by the charged particles. To kill the same amount of cells lower doses are needed

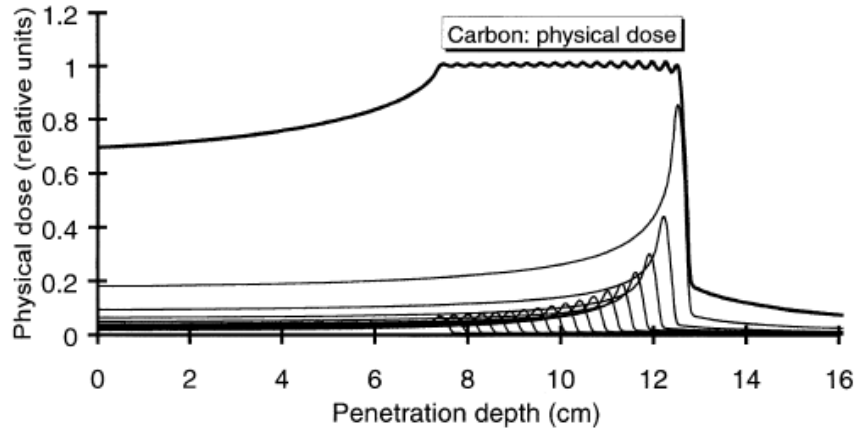


Figure 1.2: Irradiation of extended target volumes by superimposing several Bragg peaks of different beam energy and intensity [24]

compared to photons. This effect is parametrized by the Relative Biological Efficiency factor (RBE). It is defined as the ratio of the dose D_γ needed to kill a given amount of cells for photons to the dose D_{part} needed to kill the same amount of cells for the particle under interest:

$$RBE = \frac{D_\gamma}{D_{part}} \quad (1.1)$$

The Fig. 1.3 shows different survival curves (the rate of surviving cells with respect to the dose) for photons (full line) and for heavy ions (dashed line): depending on the survival rate the RBE can range from 1.5 (1% of surviving cells) to 2.1 (10% of surviving cells). The average RBE is around 1.1 for protons. The assumed RBE value for carbons is around 3. Another biological effect is the so called *Oxygen Effect*: the cells with a low oxygenation rate (hypoxic cells) are more resistant to radiations than cells with a normal oxygenation rate (normoxic or aerobic cells). As a consequence, more dose is needed to destroy hypoxic cells. Unfortunately resistant hypoxic cells are located in the cancer tumors. This effect is parametrised by the *Oxygen Enhancement Ratio* (OER) which is defined as follows:

$$OER = \frac{D_{hypoxic}}{D_{aerobic}} \quad (1.2)$$

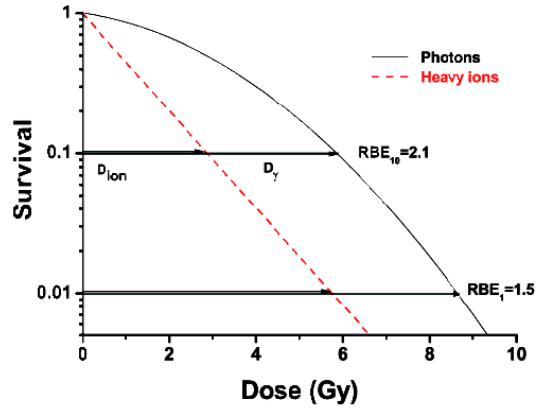


Figure 1.3: Survival curves and relative RBE for cells inactivation for 10% and 1% survival level for a typical heavy ion irradiation [15]

where $D_{hypoxic}$ is the dose needed for heavy ions to kill a fixed amount of hypoxic cells and $D_{aerobic}$ is the dose needed to kill the same amount of aerobic cells. The Fig. 1.4 shows the survival curves for X-rays and for charged particles with different stopping power values, for aerobic cells (full lines) and hypoxic cells (dashed lines). The OER value clearly depends on the stopping power value for charged particles. For X-rays the OER values is around 3. For particles with low stopping power values like carbon ions at high energies, the OER value is around 2.6. For high stopping power values like carbon at low energies, close to the Bragg peak, the OER value decreases down to 2. RBE and OER values are summarized on Fig. 1.5.

The main motivation in using protons for radiation therapy is their ballistics since protons RBE and OER values are close to the ones of X-rays, so biological effects of photons and protons on cancerous cells are very similar. A major improvement in radiation therapy may be achieved by using heavier ions: due to the increased RBE and decreased OER less dose is necessary to kill cancerous cells and no additional dose is needed to kill hypoxic radio-resistant cells. One can also notice that neutrons are very efficient in killing cancerous cells. Unfortunately, neutrons have a very poor ballistics and an accurate sighting of a tumor is very difficult.

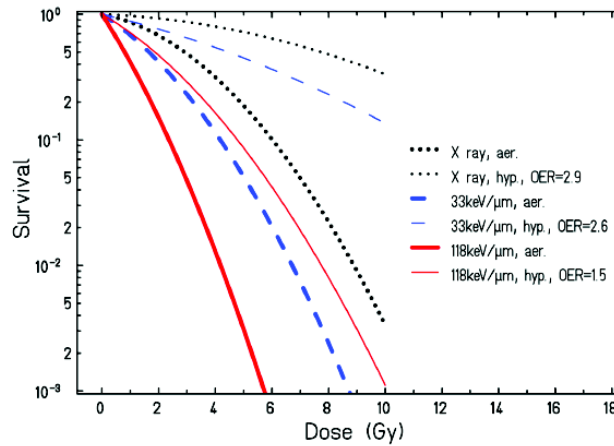


Figure 1.4: Influence of the oxygen level on cell survival of human kidney T-1 cells for carbon ions with different stopping powers [15]

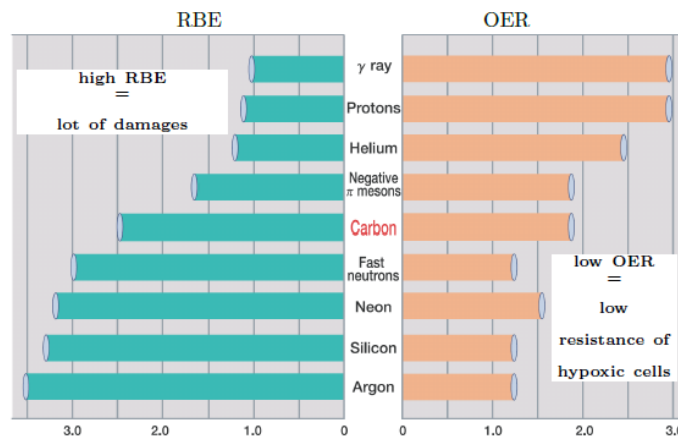


Figure 1.5: RBE (left) and OER (right) values of different particles

All these physical (ballistics) and biological (high RBE and low OER values) properties make heavy ions good candidates for their use in radiation therapy. They can be used for cancers with a low success rate with conventional therapeutic means: the main indications for charge particle therapy are radio resistant and inoperable tumors like brain, head and neck tumors. Unfortunately, also the biological prop-

erties of a hadron beam depend on the ion species of the beam. The fragmentation process modify also the biological properties of the beam inside the patient.

Summarizing both the ballistic (dose distribution) and the biological features of the light ions beam ask for an accurate knowledge of the nuclear fragmentation inside the patient.

1.2 Physics for particle therapy

As shown in last section, the main reasons for using heavy charged particles in radiotherapy are their favorable depth-dose profile and their increase in RBE respect to photons.

The use of charged particles in clinical practice requires a very strict dose control: the Bragg peak location has to be known within 1 mm and the dose in the tumor has to be delivered within 3%. In next paragraphs the basic physical concepts which are necessary to compute the dose deposition and the range of charge particles in matter are reviewed.

1.2.1 Stopping power of high energy ions

The dose deposited in tissues is the most important physical quantity in radiotherapy. The process of energy loss of light ions in matter is as well one of the most important in view of their detection and identification in the FIRST apparatus. We start then to review the dose concept, that is defined [25] as the mean energy $d\epsilon$ deposited by ionizing radiation in a mass element dm (unit Gray [Gy]):

$$D = \frac{d\epsilon}{dm} \quad [1 \text{ Gy} = 1 \text{ J/Kg}] \quad (1.3)$$

The equation (1.3) can be written emphasizing the energy lost per unith lenght by a charged particle slowing down in an absorber medium:

$$D = \frac{dN}{dS} \frac{(dE/dx)}{\rho} \quad (1.4)$$

where dN/dS is the fluence of the beam and dE/dx is the energy-loss rate or stopping power of the particle in the matter and ρ the material's density. Since the fluence can be measured and the material's density is known, one only has to know the stopping power to compute the physical dose [26, 27, 28, 29].

In the early 1930s Bethe studied the problem of the energy loss of a particle slowing-down in matter in the framework of the quantum mechanics. Let's focus now on the specific problem of a light nucleus ($Z_p \leq 10$) in the framework of the particle therapy, where ion beam ranges up to 30 cm are necessary to irradiate the tumor. These ranges correspond to specific energies (kinetic energy per unit mass) up to 220 MeV/nucleon for protons and helium ions and 430 MeV/nucleon for carbon ions in water, with particle velocities $\beta = v/c \approx 0.7$. At these velocities the energy-loss rate dE/dx in the slowing-down process is dominated by the inelastic collisions with the target electrons due to the electromagnetic interaction. The electronic interactions of a heavy charged particle occur in single collisions with energy losses ν that lead atomic excitation or ionization. So the main contribution to the process $N + e \rightarrow N + e$ comes from the exchange of a virtual photon with 4-momentum $q = (\nu/c, \vec{q})$, being the nucleus N considered as a whole at these energies.

A light nucleus can be treated as an heavy charged projectile with charge Z_p and with mass $M_p \gg m_e$ that slowing down in matter transfers a part of its momentum to the atomic electrons of the medium: the momentum transferred to each electron is small so that the trajectory of the incident particle is essentially imperturbate. Moreover the atomic electrons can be considered free and initially at rest and it is supposed they move very slightly during the interaction with the heavy particle. Under these assumptions the 4-momentum of the electron before and after the interaction is respectively $p_i = (m_e c, 0)$ and $p_f = (E_e/c, \vec{p}_e)$ and from the conservation of the 4-momentum: $p_f = p_i - q$ is possible to see that the 4-momentum transferred from the nucleus to the electron is:

$$q^2 = (2p_i \cdot q) = 2m_e \nu \quad (1.5)$$

1.2. PHYSICS FOR PARTICLE THERAPY

The maximum energy transferred is the one produced by a head-on collision:

$$\nu_{max} = \frac{2m_e c^2 \beta^2 \gamma^2}{1 + 2\gamma \frac{m_e}{M_p} + \left(\frac{m_e}{M_p}\right)^2} \approx 2m_e c^2 \beta^2 \gamma^2 \quad (1.6)$$

where the approximation is always valid for the energies used in particle therapy for which $\gamma m_e/M_p \ll 1$. Experimentally most frequently the energy losses are small and $\nu \ll \nu_{max}$. In this case the cross section of the process is given by the Rutherford formula:

$$\frac{d\sigma}{dq^2} = \frac{4\pi\alpha^2 (\hbar c)^2 Z_p^2}{c^2 \beta^2 q^4} \quad (1.7)$$

where $\alpha = e^2/4\pi\epsilon_0\hbar c$ is the fine structure constant. Substituting (1.5) in the Rutherford cross section (1.7) we obtain the cross section $d\sigma/d\nu(E, \nu)$ for an incident nucleus with energy E that loses an energy ν in a single collision with a free electron:

$$\frac{d\sigma}{d\nu}(E, \nu) = \frac{2\pi\alpha^2 (\hbar c)^2 Z_p^2}{m_e c^2 \beta^2} \frac{1}{\nu^2} \quad (1.8)$$

Thus, for small energy transfers, the cross section only depends on the energy of the recoiling electron ν and the velocity of the incident particle β . When $\nu \sim E$ the spin of the electron plays an important role and the Rutherford formula has to be substituted with Mott scattering formula simply multiplying the (1.8) with the factor $(1 - \beta^2\nu/\nu_{max})$. Let's introduce the electron density factor:

$$n_e = Z_t n_a = Z_t \frac{\rho N_A}{A} \quad (1.9)$$

where Z_t is the target atomic number and n_a is the number of atoms in unit volume in the target material, with N_A Avogadro's number and A the atomic weight of the absorbing material. The probability that an incident particle with energy E colliding with an electron will lose energy between ν and $\nu + d\nu$ while traversing an infinitesimal thickness dx of absorber is:

$$\phi(\nu) d\nu dx = n_e dx \left(\frac{d\sigma}{d\nu}(E, \nu) \right) d\nu \quad (1.10)$$

From the infinitesimal probability (1.10) it is possible now to define the moments:

$$M_n(\beta) = n_e dx \int \nu^n \frac{d\sigma}{d\nu}(E, \nu) d\nu \quad (1.11)$$

so that M_0 is the mean number of collisions in dx , M_1 is the mean energy loss in dx , $M_2 - M_1^2$ is the variance and so on. The mean rate of energy loss by charged heavy particles is M_1/dx and the resulting formula is the Bethe-Bloch formula [30]:

$$\frac{dE}{dx} = \frac{4\pi\alpha^2(\hbar c)^2}{m_e c^2} n_e \frac{Z_p^2}{\beta^2} \left[\ln \frac{2m_e c^2 \beta^2}{\langle I \rangle} - \ln(1 - \beta^2) - \beta^2 - \frac{C}{Z_t} - \frac{\delta}{2} \right] \quad (1.12)$$

where $\langle I \rangle$, C and δ are three parameters. The parameter $\langle I \rangle$ is the mean ionization energy of the target atom or molecule and is essentially the average orbital frequency $\bar{\nu}$, averaged over all the bound electron states of the atoms of the absorbing material, each with frequency ν . It is a very difficult quantity to calculate, however it can be determined from experimental data. For liquid water the values obtained from energy-loss measurements for protons and different heavier ions are in the range $\langle I \rangle = 75 - 78$ eV [31, 32, 33, 34]. The shell correction C/Z_t accounts for effects which arises when the velocity of the incident particle is comparable or smaller than the orbital velocity of bound electrons. At such energies, the assumption that the electron is stationary with respect to the incident particle is no longer valid and the Bethe-Bloch formula breaks down. The density correction δ takes into account that the electric field of the particle tends to polarize the atoms along its path. Because of this polarization, electrons far from the path of the particle are screened and so for distant collisions there is a reduction of the energy loss. This effect becomes more and more important as the particle energy increases and depends strongly on the density of the absorbing material.

The Bethe-Bloch formula (1.12) has been here obtained with the approximations discussed above and it's valid in the region of $0.05 \lesssim \beta \cdot \gamma \lesssim 1000$ with an accuracy of about 1% if the shell and density corrections are included. In this $\beta \cdot \gamma$ region the Bethe-Bloch equation depends on the material linearly through the electron density factor n_e and logarithmically through the mean ionization potential $\langle I \rangle$. The dE/dx depends on the charge Z_p and the velocity β of the projectile, but not on its mass. It increases with particle charge according to Z_p^2 . The minimum of ionization with $dE/dx \sim 2$ MeV/g·cm² corresponds to $\beta \cdot \gamma \sim 3$. At lower energies the energy-loss rate is dominated by the $1/\beta^2$ factor: the particle will release most of its energy at the end of its path in the medium. This increase in the energy loss is referred to as

Bragg peak. At the Bragg peak the particle velocity is comparable to the velocity of the orbital electrons of the material (for light ions below about 10 MeV/nucleon) and the stopping-power reaches a maximum and then drops sharply again. Here a number of complicated effects come into play, the most important of which is the possibility to pick up electrons: the effective charge of the particle decreases due to the interplay of ionization and recombination processes and Z_p in Bethe-Bloch formula has to be replaced by the effective charge Z_{eff} , which can be described by the empirical formula:

$$Z_{eff} = Z_p[1 - \exp(-125\beta Z_p^{-2/3})] \quad (1.13)$$

This effect decreases the effective charge and so the stopping power of the projectile.

A fundamental process to take into account for ion projectiles is the nucleus-nucleus collision which produces secondary particles with longer ranges than the projectile. This process influences significantly the dose map and become more and more important with the increasing of the ion mass number A . The nucleus-nucleus collisions and the nuclear fragmentation processes will be discussed in depth in next chapter 2.

Stopping power curves for protons and ^{12}C ions in water are shown in Fig. 1.6. For protons, the inelastic collision on the electrons is the dominant process for all energies. For ^{12}C ions this process is also dominant except for the last few μm of path where the nucleus-nucleus interactions become dominant: the maximum occurs at a specific energy of ~ 350 keV/nucleon.

1.2.2 Range

The energy loss rate dE/dx of a heavy particle that slows down in matter changes as its kinetic energy changes. In a sufficiently thick material the particle will deposit all its energy and stop. The mean distance that a charged particle travels before coming to rest is called range R . This is related to the energy loss by:

$$R(E) = \int_0^E \left(\frac{dE'}{dx} \right)^{-1} dE' \quad (1.14)$$

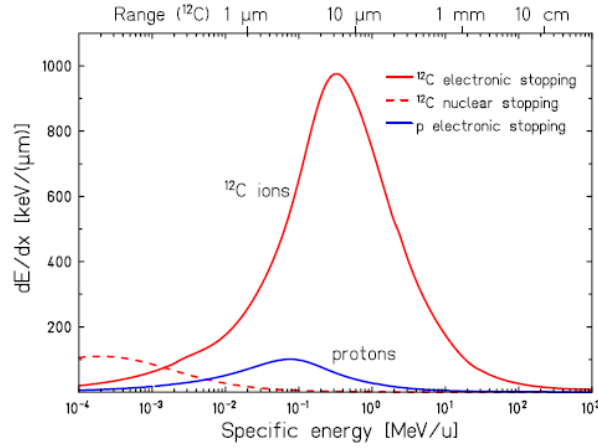


Figure 1.6: Stopping power curves for protons and ^{12}C ions in water. The range of ^{12}C ions in water corresponding to their specific energy (MeV/u corresponds to MeV/nucleon) is indicated at the top [15].

where E is the energy of the particle. This quantity differs from the thickness of the absorber crossed by the particle because of multiple scattering (see § 1.2.4). However a pure beam of ions travels approximately the same range in matter (when electromagnetic scattering represents the dominant source of energy loss).

It is possible to find a scaling relation between ranges of different particles, since the stopping power in a given material is a function of the only charge and the velocity $dE/dx = Z_p^2 f(\beta)$. Differentiating the relation $E = M_p \gamma c^2$ respect to β :

$$\frac{dE}{d\beta} = M_p c^2 \frac{\beta}{(1 - \beta^2)^{\frac{3}{2}}} = M_p \cdot g(\beta) \quad (1.15)$$

where $g(\beta)$ is another function of β . The range can be now written as:

$$R(E) = \frac{M_p}{Z_p^2} \int_0^\beta \frac{g(\beta)}{f(\beta)} d\beta = \frac{M_p}{Z_p^2} h(\beta) \quad (1.16)$$

where $h(\beta)$ is an universal function that depends only on the initial β of the particle. This is a scaling law for ranges of particles slowing down in matter: the range of ions with the same specific energy scales with a factor M_p/Z_p^2 or simply A_p/Z_p^2 , being A_p

the mass number of the projectile. The Fig. 1.7 shows the range of different particle type with respect to their incident energies.

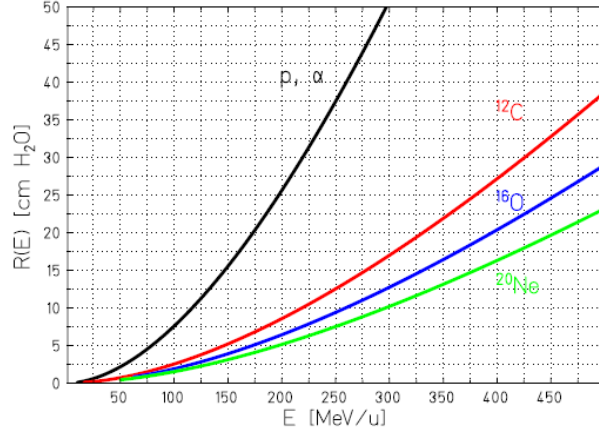


Figure 1.7: Mean ranges for different ions traversing water [15]

1.2.3 Energy and Range Straggling

The value of the dE/dx calculated in (1.12) is a mean value (coming from equation (1.11)). Actually the amount of energy lost by a charged particle that crosses a fixed thickness of absorber varies due to the statistical nature of its interactions with individual electrons in the material. For this reason, although the probability for an energy loss ν in an infinitesimal absorber layer dx is given by (1.10), the calculation of the corresponding probability for a finite thickness x of absorber is more complicated. The stochastic nature of the process transform the mean value of the dE/dx into the most probable value of energy loss, with unlikely large energy transfer events, associated with the production of high energy recoils electrons, called delta rays. The result is that the energy loss distribution will be asymmetric with a tail on the high energy side. This distribution has been described in the Vavilov-Landau theory for the energy fluctuations of charged particles passing through a thin absorber. In the limit of many collisions this distribution can be well

approximated by a Gaussian with σ given by:

$$\sigma_E = 4\pi Z_p^2 n_e \alpha^2 (\hbar c)^2 x \quad (1.17)$$

Because of these fluctuations in energy loss, a beam of particles of fixed energy will have a distribution of ranges in thick absorber. This phenomenon is known as range straggling. The two fluctuations are related by:

$$\sigma_E^2 = \left(\frac{dE}{dx} \right)^2 \sigma_R^2 \quad (1.18)$$

For a monoenergetic beam of particles the relative straggling σ_R/R increases with increasing Z_t of the absorber and decreases with increasing kinetic energy, approaching a constant value:

$$\frac{\sigma_R}{R} \sim \frac{1}{2} \left(\frac{m_e}{M_p} \right)^{1/2} \quad (1.19)$$

For light ions stopping in water the relative straggling is of the order of 10^{-3} and due to the $1/\sqrt{M_p}$ dependence it is smaller for heavier ions than for protons: for example is reduced by a factor 3.5 for ^{12}C ions with respect to protons with the same range (see Fig. 1.8).

1.2.4 Multiple scattering

The charged particles crossing a material undergo the process of multiple scattering, that deflects the projectile from the initial direction, and causes a lateral displacement of the tracks. As a result a beam will have a lateral spread mainly caused by elasting Coulomb interactions with target nuclei, while scattering due to electronic interactions, which dominate the dE/dx process, can be neglected. This is true especially for particle lighter than the target nuclei, when the small energy transfer to the nucleus is negligible, and the scattering is elastic. The scattering differential cross section for an ion that interacts in the Coulomb potential of a simple target nucleus is given by the Rutherford scattering formula:

$$\left(\frac{d\sigma}{d\Omega} \right)_{Ruth} = \frac{1}{4} \frac{\alpha^2 (\hbar c)^2 Z_p^2 Z_t^2}{c^2 \beta^2 |\vec{p}|^2} \frac{1}{\sin^4(\theta/2)} \quad (1.20)$$

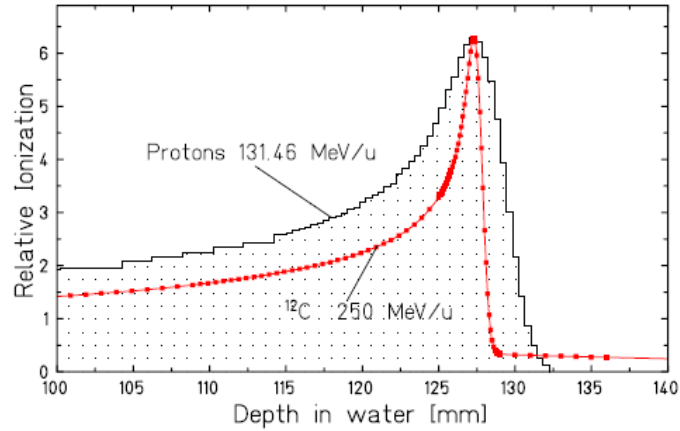


Figure 1.8: Measured Bragg peaks of protons and ^{12}C ions having the same mean range in water [35]

The main effect of Coulomb scattering is the angular deflection of the particle along its path, according to the $1/\sin^4(\theta/2)$ dependence of the Rutherford formula for a single collision. When a particle crosses a thick block of material the number of collisions increase producing the multiple Coulomb scattering. Most of these single collisions will result in a small angular deflection of the particle. The cumulative effect of these small angle scatterings is, however, a net deflection from the original particle direction.

A particle slowing down in matter thus will follow a random zig-zag trajectory, because of multiple scattering. If the average number of independent scattering is large and the energy loss is small or negligible, the problem can be treated statistically to obtain the probability distribution for the net angle of deflection as a function of the thickness of material traversed. Since each individual small angle scatter is a random process, we expect the mean scattering angle of a beam of particles with respect to the incident direction to be zero. On the other hand, the rms scattering angle θ_s will be in general nonzero. The Coulomb scattering distribution is roughly Gaussian for small deflection angles, but at larger angles, greater than a few θ_s , it behaves like Rutherford scattering (1.22), having larger tails than does a Gaussian

distribution. The expectation value of θ^2 due to multiple scattering of a particle, while crossing a length x of the material is $\theta_s^2 = \int \theta^2 (d\sigma/d\Omega)_{Ruth} d\Omega$, and the rms scattering angle is [36]:

$$\theta_s = \frac{E_s}{pc\beta} \cdot Z_p \cdot \sqrt{\frac{x}{X_0}} \quad (1.21)$$

where the particle's velocity has been assumed not appreciably reduced while crossing the material. The absorber material is characterized by the thickness x and the radiation length X_0 . Tabulated values of the radiation length X_0 exists for different materials [37]: target containing heavy elements cause a larger angular spread than targets of light elements with same thickness. The E_s value has been computed using the Moliere theory of multiple scattering [38, 39]:

$$\theta_s = \frac{13.6 \text{ MeV}}{pc\beta} \cdot Z_p \cdot \sqrt{\frac{x}{X_0}} \cdot \left[1 + 0.038 \cdot \ln \left(\frac{x}{X_0} \right) \right] \quad (1.22)$$

The angular spread decreases with the projectile mass, but increases significantly towards low energy due to the $pc\beta$ term in the denominator of equation (1.22).

Comparing beams with the same range in water (for example 150 MeV protons and 285 MeV/nucleon ^{12}C ions with $R = 15.6$ cm) the angular spread θ_s due to multiple scattering for protons is more than three times larger than for carbons (see Fig. 1.9). The small lateral deflection of heavy ions penetrating through an absorber is a particular advantage of heavy ions in comparison to protons and is of clinical relevance for treatments near organs at risk.

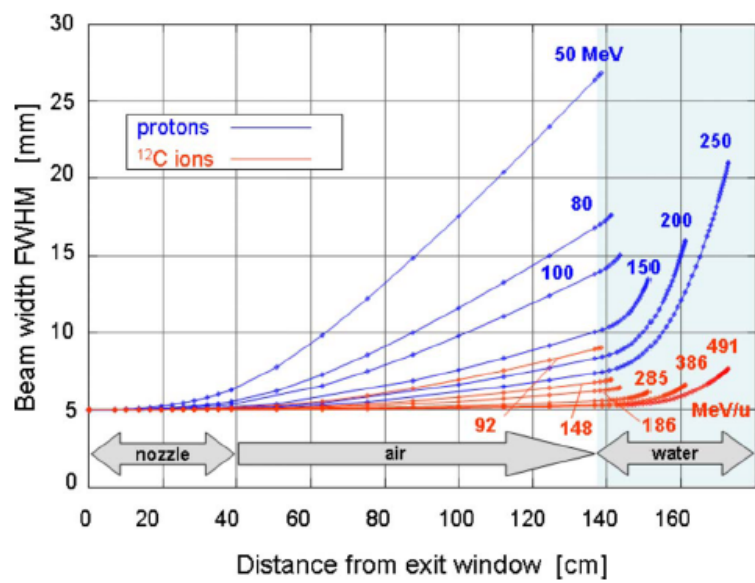


Figure 1.9: Calculated beam spread for protons and ¹²C ions traversing 1 m of air before entering in water. Carbon ions show a much smaller spread than protons at the same penetration depth [15].

Chapter 2

Nuclear fragmentation

2.1 Hadronic interactions and nuclear fragmentation processes

The stopping process of charged particles penetrating an absorber is driven by the electromagnetic interaction in the collisions with atomic electrons. The probability of nuclear reactions, driven by strong interactions, is much smaller, but leads to significant effects at large penetration depths.

At energies of several hundred MeV/nucleon nuclear spallation reactions may result in a complete disintegration of both projectile and target nuclei (e.g. in central head-on collisions), or in partial fragmentations.

In central head-on collisions all nucleons in both target and projectile are supposed to participate to the reaction and so this will be characterized by a high fragments multiplicity. For geometrical reasons peripheral collisions, where the beam particle loses one or more nucleons, are the most frequent nuclear reactions occurring along the stopping path of the ions. Only few nucleons in the overlap zone between the projectile and target nuclei are supposed to effectively interact during this kind of collision, so the number of participant nucleons and the energy and the momentum transfers are relatively small. As a result, in the frame of reference

2.1. HADRONIC INTERACTIONS AND NUCLEAR FRAGMENTATION PROCESSES

of the laboratory, just few fragments are observed, mostly in the forward direction, with velocities approximately equal to that of the projectile. These particles can be scraped off from the direct overlap of the nuclei or can originate from the de-excitation of the projectile residue (projectile fragmentation). Also another family of particles is observed in these reactions: light particles that have an almost isotropic distribution in the laboratory frame and that are evaporation products from the excited target residue (target fragmentation).

The fragmentation process of peripheral collisions can be described with the two steps model of *abrasion-ablation* which occur in two different time scales [40, 41]. This model is a simplification of nucleus-nucleus collision and is schematically illustrated in Fig. 2.1. The first stage is the *abrasion*, when a projectile hits a target nucleus, the nucleons within the overlap zone (*fireball*) interact with each other and are sheared away from either the projectile or the target. At this stage light particles are promptly emitted and excited quasi-projectile and quasi-target are formed. The projectile fragments follow the initial trajectory with approximately the same initial velocity, while the target fragments slowly recoil.

The remnants of the colliding nuclei are called pre-fragments and are excited as a result of the *abrasion*. The characteristic time of this reaction step is several times 10^{-23} s, that is the typical value of strong interactions [42, 41].

In the second reaction step (*ablation*) the system reorganizes, that means it thermalizes and de-excites by the evaporation of neutrons, protons and light nuclei as well as by fission and emission of gamma rays or by a simultaneous break-up with IMFs (Intermediate Mass Fragments) emissions (see Fig. 2.2). During the whole de-excitation phase there is a competition between these different processes. According to the statistical models used for ablation process the characteristic time for the emission of particles varies between $\sim 10^{-16}$ s at an excitation energy of 10 MeV and $\sim 10^{-21}$ s at 200 MeV [43, 44].

For both *abrasion* and *ablation* steps, several models have been developed. A complete nucleus-nucleus collision modeling is achieved by a combination of a model describing the *abrasion* (or entrance channel) and a model describing the *ablation* (or

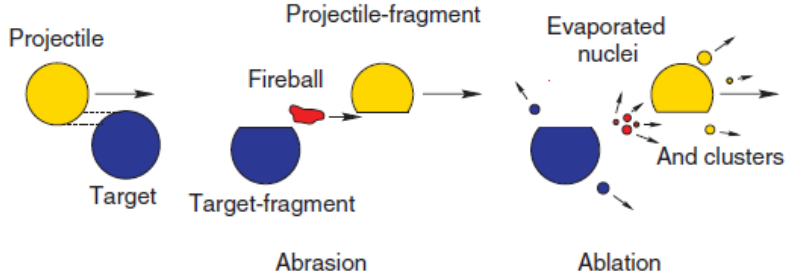


Figure 2.1: Schematic view of a nucleus-nucleus collision

decay phase). Various MC codes for particle transport implement different models to describe the hadron-nucleus and the nucleus-nucleus interactions. Such models are based on the described ablation-abration process to take into account inelastic nuclear interaction and the fragmentation process.

MC codes that simulate the transport of ions in tissue-equivalent materials in the energy range of interest for particle therapy include FLUKA [45, 46], PHITS [47], GEANT4 [48], MCNP eXtended (MCNPX) [49] and SHIELD-HIT [50]. Among these MC codes, FLUKA is the MC code used for the MC simulation of the FIRST experiment. An overview of the hadronic models implemented in this code are presented in the next section, with a particular focus in hadron-nucleus and nucleus-nucleus interactions in the energy range of interest for particle therapy. FLUKA code can also be considered to represent the typical scheme of a generic MC code, as most multi-purpose MC implementations follow a similar model to describe the hadronic cascade and subsequent reaction processes. A detailed description of hadronic interactions in FLUKA can be found in several papers and references

therein [51, 52, 53, 54, 55].

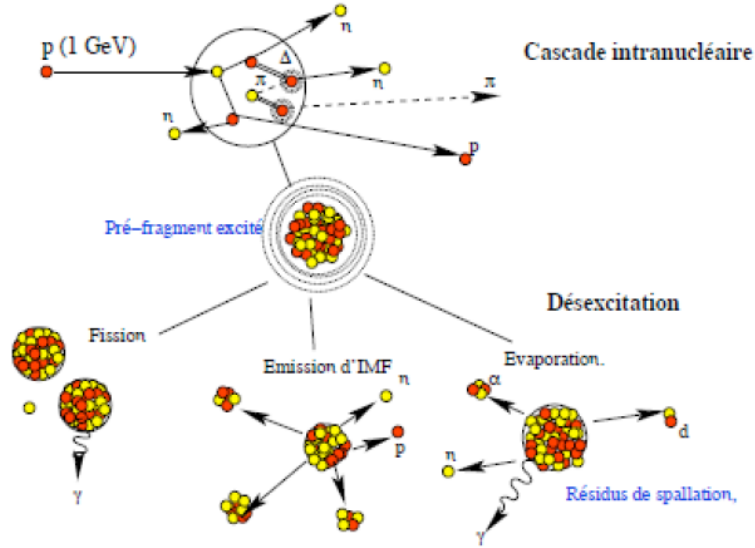


Figure 2.2: Schematic view of different de-excitation processes in a nucleus-nucleus collision

2.2 Hadronic interaction models in FLUKA

The FLUKA code is a general purpose Monte Carlo code for the interaction and transport of hadrons, heavy ions, and electromagnetic particles from few keV to cosmic ray energies in a wide range of materials [45]. Energies for neutron transport ranges from thermal energies to 20 MeV. Transport in arbitrarily complex geometries, including magnetic field, can be accomplished using the FLUKA combinatorial geometry. Both electromagnetic and hadronic interactions are supported up to 10 PeV, including nucleus-nucleus interactions up to 10 PeV/nucleon. FLUKA code is built and maintained with the aim of including the best possible physical models in terms of completeness and precision. The validity of its physical models has been benchmarked against a variety of experimental data over a wide range of energies,

ranging from accelerator data to cosmic ray showers in the earth atmosphere. In the field of particle therapy the hadron-nucleus and nucleus-nucleus interaction models are fundamental to achieve an accurate dose calculation of the dose released in the patient body. In what follows an overview of the hadronic models implemented in FLUKA is given, with a particular focus in the energy range of interest for particle therapy applications (up to 400 MeV/nucleon for carbon ion projectile). A detailed description of the hadronic models is beyond the purpose of this thesis work.

2.2.1 Hadron-nucleon (h-N) interactions

A satisfactory description of hadron-nucleus and nucleus-nucleus processes requires an exhaustive understanding of hadron-nucleon collisions over a wide energy range. In FLUKA h-N inelastic collisions are described in terms of resonance production and decays up to a few GeV [51] and in terms of Dual Parton Model (DPM), coupled to a hadronization scheme, up to several tens of TeV [56]. DPM allows a successful description of soft collision processes for which QCD perturbation theory cannot be applied. This model is a particular quark/parton string model, in which hadron-hadron interactions results in the creation of two or more QCD color strings, from which hadrons are generated.

2.2.2 Hadron-nucleus (h-A) interactions

Hadron-Nucleus interaction process in FLUKA can be schematically described as a sequence of the following steps:

- Glauber-Gribov cascade (> 5 GeV) or a detailed Generalized Intra-Nuclear Cascade (GINC) for lower energies
- Pre-equilibrium emission
- Evaporation, Fission, Fragmentation (Fermi break-up) and final γ de-excitation

The first stage is a cascade phase that describes the interaction between the two systems in terms of interaction between the nucleons. This stage corresponds to the

entrance channel or *abrasion* process. The last three stages represent the processes for which the excited system, formed after the first cascade stage, de-excites and reaches thermal equilibrium through a sequence of two-body elastic interactions. This process is called nuclear thermalization and correspond to the decay phase or *ablation* process. The mechanism describing the interaction in the first cascade stage is described by two different models depending on the energy of the process. A Glauber-Gribov cascade formalism [51, 54] is used for energies greater than 5 GeV/nucleon. Hadron–nucleus interactions models for lower energies, of interest for therapeutic applications, are described in FLUKA by the pre-equilibrium-cascade model PEANUT (Pre-Equilibrium Approach to NUclear Thermalization) [51]. The two main components of the PEANUT model are a generalized Intra-Nuclear Cascade (GINC), for the description of the initial hadron-nucleus non-elastic interaction stage, and the subsequent pre-equilibrium stage model, which de-excites the hot nuclear components by emission of nucleons and light nuclei ($A < 5$), until thermal equilibrium is reached.

Glauber-Gribov cascade The Glauber-Gribov cascade is a field theory formulation of the Glauber model [57, 58, 59], that is a quantum mechanical method to obtain elastic, quasi-elastic and absorption hadron-nucleus cross sections from free hadron-nucleon cross section and nuclear ground state only: inelastic interaction are thought as multiple interactions of the projectile with ν target nucleons.

Generalized Intra-Nuclear Cascade (GINC) At energies high enough to consider coherent effects between nucleons as corrections, h-A interaction can be described by the GINC model, based on the same original Intra-Nuclear Cascade (INC) mechanism assumptions, summarized in the following [51]. In INC h-A interactions are described as a cascade of two-body collisions, concerning the projectile and the reaction products, where the target nucleus is described as a cold Fermi gas of nucleons in their potential well. The particle motion is formulated in a classical way. It can be subject to an average nuclear and Coulomb mean potential, which must be added to the free particle kinetic energy when tracking through the nucleus. The

radial and energy dependence of such field are model- and particle-dependent. The effect of the nuclear mean field on the particle motion can produce curved trajectories in a semiclassical approach, according to energy and momentum conservation, depending on the model. In INC models the hadrons propagate like free particles in the nuclear medium, with interaction probability per unit length given by free space h-N cross sections σ_{hN} , properly averaged over the Fermi motion of the target nucleons, times the local nuclear density. So the hadron multiple collision process in nuclei is described as the incoherent sum of the two body processes h-N: this means that the interactions occur like in free space in the center of mass system of the two colliding hadrons in a completely incoherent and uncorrelated way. The previous assumptions translate in the requirement that the wavelength associated to hadron motion λ_h must be much shorter than the hadron mean free path inside the target nucleus (free h-N cross sections), and also much shorter than the average distance among two neighboring nucleons (incoherence):

$$\lambda_h = \frac{2\pi\hbar}{p_h} \ll \frac{1}{\sigma_{hN}\rho} \quad (2.1)$$

$$\lambda_h = \frac{2\pi\hbar}{p_h} \ll \left(\frac{3}{4\pi\rho}\right)^{\frac{1}{3}} \quad (2.2)$$

where p_h is the hadron momentum and ρ is the nuclear density ($\approx 0.17 \text{ fm}^{-3}$ in the nucleus core). The first condition set the lower limit of validity of INC models at the energy of 200 MeV, that corresponds to the pion production energy, but the second requires a particle momentum greater than 1 GeV/c, that would make INC models unuseful. Fortunately Pauli blocking and other nuclear quantum effects, together to an accurate modelization of the target nuclear density, contribute to increase the mean free path and so to diminish the lower energy limit of validity of INC (this energy range is of particular interest because is where the great part of the processes take place during an h-A interaction). Intra-Nuclear Cascade models have been of great success in the past for describing the basic features of nuclear interactions in the 0.2 – 2 GeV range, being also able to compute reaction cross sections. Recently they have been generalized (GINC) to describe reactions at higher and lower energies,

thank to the inclusion of many quantum effects [52, 54] and especially of the pre-equilibrium emission process. In addition, nuclear densities specific to protons and neutrons are chosen, binding energies are obtained from mass tables and updated after each particle emission. The conservation of additive quantum numbers, energy and momentum is ensured on an event-by-event basis including the recoil of the residual nucleus [46]. Secondary particles produced in the cascade of collisions are treated the same way as primaries.

Pre-equilibrium emission The cascade simulation proceeds until all nucleons are below an energy cut-off around 50 MeV and all particles but nucleon (typically pions) have been emitted or absorbed. The nuclear configuration at this point is used as starting condition for the pre-equilibrium stage. Pre-equilibrium particle emission is described according to the statistical exciton formalism of M.Blann [60] with some modification [51]. At the end of GINC stage the nuclear configuration is characterized by the number of protons and neutrons, by particle-like excitons n_P (nucleons excited above the Fermi level) and hole-like excitons n_H (holes in the Fermi sea) and by the compound nucleus excitation energy E_{tot} . The pre-equilibrium process is described as a chain of steps that follow the statistical assumption that any partition of the excitation energy E_{tot} among n excitons ($n = n_P + n_H$), has the same probability to occur. So the nucleus proceeds in the chain through nucleon-nucleon collisions which increase the number of pairs hole- particle-like excitons. Excitons of a certain type and energy, have at each step a certain probability to be emitted in the continuum. The chain stops, and equilibrium is reached, when either the exciton number n is sufficiently high ($n = 2 \cdot g \cdot E_{tot}$), where g is the single particle level density, or when the excitation energy is below any emission threshold.

Equilibrium stage At the end of the pre-equilibrium stage the residual nucleus is assumed to be in an equilibrium state, with the excitation energy being shared among a large number of nucleons. The compound nucleus is now characterized by its mass, charge and excitation energy (typically from few MeV to several tens of MeV). The excitation energy can be higher than the separaton energy, so nu-

cleons and light fragments (α , ${}^2\text{H}$, ${}^3\text{H}$, ${}^3\text{He}$) can be still emitted: they constitute the low-energy part (few MeV) of the emitted particles by the residual nucleus. Neutron emission is favoured over charged particle emission, due to the Coulomb barrier, especially for medium-heavy nuclei [53]. This process can be described as an evaporation from a hot system based on the original statistical approach by Weisskopf-Ewing [44, 61]. The FLUKA implementation of this model is extended to allow the emission of about 600 possible nucleons and nuclei in various excited states with $A \leq 25$.

Evaporation is in competition with fission, that is another possible equilibrium process particularly effective for the description of residual nuclei production from heavy targets ($Z \gtrsim 70$). Fission is the consequence of a collective deformation of the compound nucleus due to the excitation energy. Due to this deformation the binding energy of the nucleus decreases and the nucleus can separate, most of the times into two heavy fragments, with a certain probability [62]. After scission, the fragments acquire kinetic energy from the Coulomb repulsion between them and their mass distribution depends on Z and on the excitation energy of the fissioning nucleus.

For light residual nuclei, where the excitation energy can overwhelm the total binding energy, a statistical fragmentation model (Fermi break-up) is more appropriate [63, 64] and in competition with evaporation process. In the frame of this model, light excited nuclei can break into two or more fragments. The probability for the branching ratios into all possible stable and unstable fragments including excited states is derived based on phase space, spin and Coulomb barrier considerations [52].

The evaporation/fission/fragmentation process continues until the nuclear excitation energy becomes lower than all separation energies for nucleons and fragments, and leaves generally the residual nucleus in an excited state. The residual excitation energy is then dissipated by emission of γ -rays. FLUKA describes prompt γ de-excitation through a cascade of consecutive photon emissions in the continuum, until the ground state is reached. Actually prompt γ emission occurs also during pre-equilibrium and evaporation stages, in competition with particles emission, but its relative probability is low, and it can safely neglected in most practical applications.

The de-excitation stage ends leaving the residual nuclei in their ground state. This process is supposed to depend only on the residual nucleus mass, Z and excitation energy after evaporation, and not on the details of the previous interaction history. These equilibrium processes represent the last stage of a nuclear interaction and so are critical for a correct calculation of residual nuclei distributions after the interactions: for example for activation and residual dose rate studies.

Radioactive decays of the residual nuclei are performed according to tabulated data of decay modes. The decay modelling is based mostly on tabulations from ENSDF1 (Evaluated Nuclear Structure Data File) [65].

2.2.3 Nucleus-nucleus (A-A) interactions

The probability function that a projectile nucleus will collide with a target nucleus within a certain distance x in the matter depends on the total reaction cross sections σ_R , defined as the total nuclear cross section σ_{tot} minus the elastic nuclear cross section σ_{el} of two colliding nuclei at a given energy E :

$$\sigma_R(E) = \sigma_{tot}(E) - \sigma_{el}(E) \quad (2.3)$$

In FLUKA, as in all particle and heavy ion transport codes, the total reaction cross section σ_R , and the lifetime of the particle for decay, are essential quantities in the determination of the mean free path of a transported particle: the next collision point is chosen using the calculated total reaction cross section. It is therefore crucial that accurate total reaction cross section models, based on reliable data, are used in the transport calculations [66]. Phenomenological data-driven models are generally used for the computation of σ_R in MC codes.

For energies below a few GeV down to the Coulomb barrier, FLUKA uses a semi-empirical modified model of the Tripathi parametrization of total nuclear reaction cross sections for A-A interaction [67, 68, 69]. For higher energies a complex matrix of A-A reaction cross sections has been computed with Glauber model prediction. Fig. 2.3 shows σ_R as predicted by FLUKA for carbon ions for the most frequent elements present in the human body in the energy range of interest for particle therapy.

The total reaction cross section σ_R shows a strong energy dependence at energies below about 20 MeV/nucleon, while at energies higher than 100-200 MeV/nucleon a nearly flat energy dependence is observed.

To generate the secondary particles of the collision, we need the information about the final states of the collision: such information comes from hadronic models. Nucleus-Nucleus interaction models follow essentially the same decay phase of h-A interactions described by PEANUT (evaporation/fission/fragmentation/ γ de-excitation and radioactive decays stages). Instead, for the initial cascade stage an extension of the INC approach or the use of alternative models is adopted, depending on the energy of the process. For energies greater than 5 GeV/nucleon the DPMJET-III model [72] is implemented for hadronic interactions. This model is based on the DPM (dual parton model), coupled to a hadronization scheme, in connection with the Glauber formalism [57]. DPMJET is called once per A-A interaction and a list of final state particles as well as up to two excited residual nuclei with their relevant properties are returned by DPMJET for transport to FLUKA.

In the energy range of interest for particle therapy a relativistic Quantum Molecular Dynamics model (rQMD) [70, 71] has been adopted in FLUKA in the energy range from 5 GeV/nucleon down to 100 MeV/nucleon [72, 73], while the Boltzmann Master Equation (BME) theory [72, 74] can be used for ion energies lower than 100 MeV/nucleon. In the following an overview of rQMD and BME models is reported [55].

rQMD model The h-A interactions, for which the potential generated by the projectile hadron can be neglected in first order, are well described by the INC approach, especially when the target nucleus is large. For such cases the projectile can be thought to move in the static mean field of the target nucleus while considering short-range correlations between the nucleons. The extension of the GINC approach to light projectile nuclei is relatively straightforward for energies higher than the binding energy of the light nucleus [51]. On the contrary, for the description of A-A interactions including heavier systems for both projectile and target nuclei, the potential field of the projectile nucleus should be taken into account. Hence, a

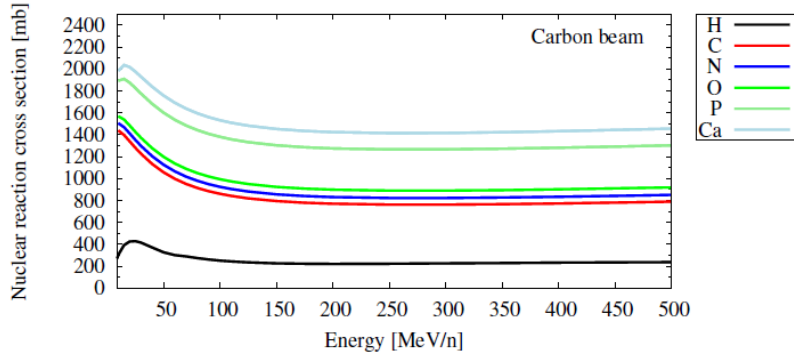


Figure 2.3: Reaction cross sections σ_R of carbon ions at therapeutic energies as predicted by FLUKA for the most frequent elements (by weight) present in the human body [55]

description in which each nucleon of the colliding nuclei is embedded in an average field due to the nucleons of both nuclei is more appropriate.

In QMD models the nuclear ground state is described as a set of nucleon configurations in which each nucleon is represented by a Gaussian wave function and moves according to its Fermi kinetic energy inside the potential originating from all other nucleons. When two nuclei, evolving according to classical Hamiltonian equations of motion of their constituent nucleons, come close to each other, the nucleons feel the effect of a global potential which influences the collision process.

For the description of A-A interactions, FLUKA is currently interfaced with a modified version of the rQMD-2.4 code (in cascade mode) [72] which is based on the original work by Sorge et al. [73]. Remaining excited pre-fragment leftovers are treated using the PEANUT de-excitation models.

BME theory The QMD approach can provide reliable results down to approximately 100 MeV/nucleon. In the region below this threshold the experimental data are quite well reproduced considering only the processes of complete fusion of projectile with the target nucleus and of incomplete fusion (or break-up-fusion) reaction in which projectile-like or target-like fragments, produced by a break-up process,

fuses with the partner nucleus [75]. The fusion process (complete or incomplete) creates an excited composite nucleus. Statistical equilibrium is reached through a cascade of nucleon–nucleon (N-N) elastic interactions during which nucleons or clusters of nucleons may be emitted with emission energies higher than those expected from evaporation of a system in equilibrium, and, in the case of IMF, with a much higher yield. This emission process is called *coalescence*. The BME theory describes the time evolution of the momentum distributions of the nucleons during the thermalization process of the composite excited nucleus [78, 79].

The BME theory has been used for evaluating such pre-equilibrium emissions for a representative set of ion pairs at different energies, carrying out a proper parametrization of the calculated ejectile multiplicities and double differential spectra and creating a database of the obtained parameters. By a proper interpolation of these parameters the pre-equilibrium emissions in fusion events, whose probability of occurrence is evaluated as a function of the incident energy and the mass and atomic numbers of the interacting nuclei, can be simulated along the reaction chain for any pair of interacting ions [72]. If interpolation from the pre-computed database is not feasible for a given composite nucleus, the PEANUT pre-equilibrium model is invoked for thermalization. Once the residual nuclei are in an equilibrium state, the PEANUT de-excitation models are applied.

2.3 Fragmentation cross sections measurements and benchmarking with MC

The study of the fragmentation processes in nucleus-nucleus collisions has been studied in the past for different combinations of targets, projectiles and beam energies. Most of these experiments measured the total fragments yield or total and partial charge-changing cross sections in thick targets, measuring the attenuation of the beam and the build up of secondary fragments [80, 81, 82, 83, 84]. The typical setup for such experiments (see Fig. 2.4) is constituted by a start counter (usually a scintillator) to count the number of primary ions, a target and a telescope of two

2.3. FRAGMENTATION CROSS SECTIONS MEASUREMENTS AND BENCHMARKING WITH MC

or more detectors (usually scintillator or silicon detectors) for tracking and charge identification of the fragments produced in the interaction with target. This typical setup measures a combination of the energy released ΔE , the time of flight ToF or the total energy E , depending on the detector configuration and on the ion beam energy.

Usually the setup was positioned along the beam axis to detect only the forward fragments emission [85]. In some cases few angle configurations have been exploited [86].

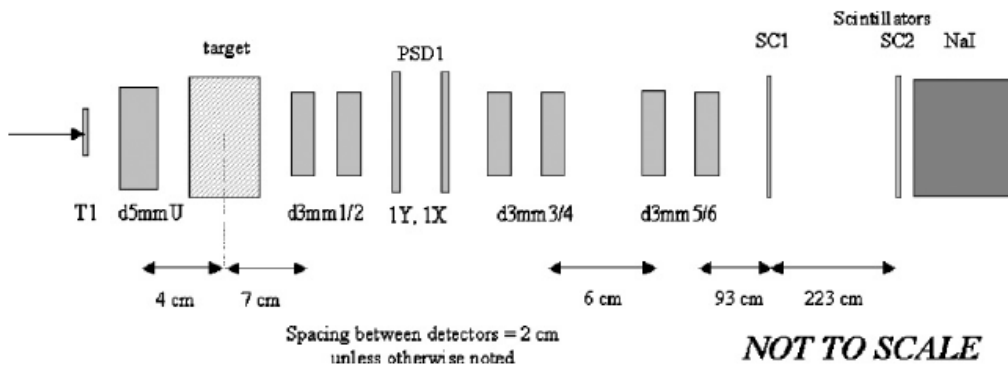


Figure 2.4: Schematic diagram of the apparatus used by Zeitlin et al., [86] for the measurement of fragmentation cross sections. The position of the detectors, as well as target material and thickness, depend on the projectile charge and energy and the target material. T1 gives the trigger; all other detector are silicon detectors with the exception of the most downstream three scintillator detectors

The total and partial charge-changing cross sections (TCC and PCC) are basic quantities characterizing ion beam fragmentation reactions in matter. The total charge-changing cross section is defined as:

$$\sigma_{tcc}(E) = \sigma_R(E) - \sigma_{nr}(E) \quad (2.4)$$

where σ_R is the total reaction cross section and σ_{nr} is the neutron-only removal cross section. σ_{tcc} is integrated over angles, energies and possible interaction channels of

the produced project-like and target-like fragments.

The charge changing cross section [82], denoted also by $\sigma_{\Delta Z \geq 1}$, is often defined to be the cross section to remove at least one charge from the projectile, or equally to produce fragments with a charge different from the projectile. This can refer to a specific fragment (PCC or elemental cross sections) or to the total charge changing cross section (TCC), which is the cross section of a reaction where the projectile nucleus is not observed in the reaction products.

TCC can be obtained measuring the attenuation of the primary particles due to the interaction with the target:

$$N_f = N_0 \exp(-x/\lambda) \quad (2.5)$$

where N_f and N_0 are the final and the initial number of projectile particles, x is the target thickness and λ is the interaction mean free path in the target from which the TCC can be calculated:

$$\sigma_{tcc} = \frac{A}{N_A \times \rho \times \lambda} \quad (2.6)$$

with A the mass number of the target, ρ the target density and N_A the Avogadro's number.

PCC cross sections quantify the probability to produce fragments with a given charge and σ_{tcc} is the sum of PCC cross section $\sigma_{pcc, \Delta Z}$:

$$\sigma_{tcc}(E) = \sum_{\Delta Z} \sigma_{pcc, \Delta Z}(E) \quad (2.7)$$

A deeper knowledge of the fragmentation process is provided by the measure of the isotopic cross sections that describe the production of a fragment with a given charge and mass. Aiming at the test of theoretical models, the isotopic cross section, which refers to production of a specific isotope, is a more stringent test than the PCC and TCC cross sections. Differential cross sections, measured as a function of one or more variables, provide stringent test of nuclear interaction models. However, most of the measurements performed in the past are related to the total number of fragments detected, providing in some cases the charge of the fragments and in some few other cases the isotopes [87, 88, 89].

2.3. FRAGMENTATION CROSS SECTIONS MEASUREMENTS AND BENCHMARKING WITH MC

Particle therapy application renewed the interest in fragmentation processes of light ions ($Z \leq 10$) and in particular in the measure of the angular and energy distribution of the produced fragments. To improve the knowledge on the ^{12}C fragmentation processes, measurements of light charged fragment production in thick target of water and PMMA have been performed by the Japanese treatment centers (Chiba and Hyogo) [90, 91] and by the GSI biophysics department [83, 92, 93] in the energy range from 200 to 400 MeV/nucleon. These measurements were used to determine the integrated flux and energy distributions of the fragments relative to the penetration depth in water. In the last years such measurements have been used to benchmark nuclear interaction models of different particle transport codes [10, 11, 12, 13, 14]: data from [91, 87, 83, 94, 95] have been compared with FLUKA and GEANT4 simulations [13], taking into account experimental condition and techniques used to select fragments. In GEANT4, differently from FLUKA, the user can choose different theoretical models for the nuclear interactions. In the following we present some results for the GEANT4 QMD ([96]) model and BIC LI (BINARY Cascade Light Ions, [97]) model for the entrance channel phase. For the decay phase the GEANT4 default model is used ([98]). Fig. 2.5 and Fig. 2.6 show respectively the TCC and PCC cross sections for ^{12}C in water and polycarbonate ($\text{C}_{16}\text{H}_{14}\text{O}_3$) simulated by FLUKA and GEANT4 compared with experimental data ([91, 87, 83]). In Fig. 2.7 the fragment yields at different depths for a carbon beam at 400 MeV/nucleon in water is shown for FLUKA, GEANT4 and experimental data ([94, 95]). The build-up curves for charged fragments of primary ^{12}C ions with $Z = 1$ to 5 have been measured varying the thickness of the water target.

In conclusion, for integral quantities such as integral PCC and TCC cross sections and fragment yields at different depths in water, differences between measurements and FLUKA and GEANT4 predictions of the order of some tens of percent were found. Comparisons between other MC simulation codes ([12, 101]) have shown similar discrepancies with experimental data. The same happens for the angular and energy distributions. In principle the nuclear models are not well constrained by thick target data, that superimpose different energies effects. In order to improve the models, experiments on thin targets were planned. A new generation of frag-

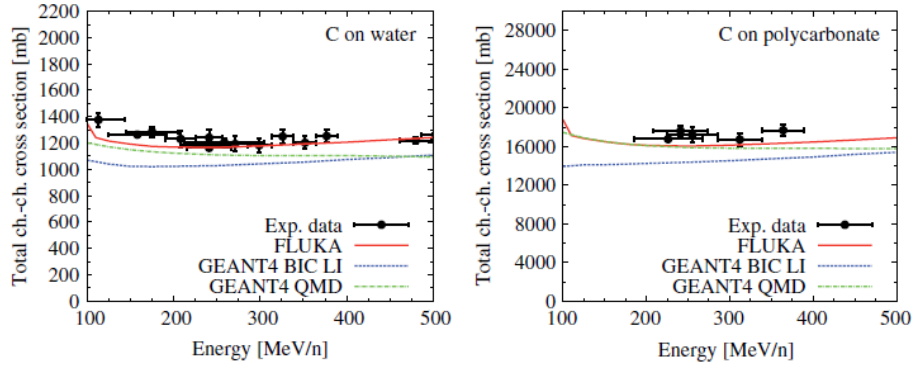


Figure 2.5: Total charge-changing cross sections for carbon ions interacting with water and polycarbonate. Vertical error bars indicate the statistical error of the experimental data ([87, 83, 91]) [13]

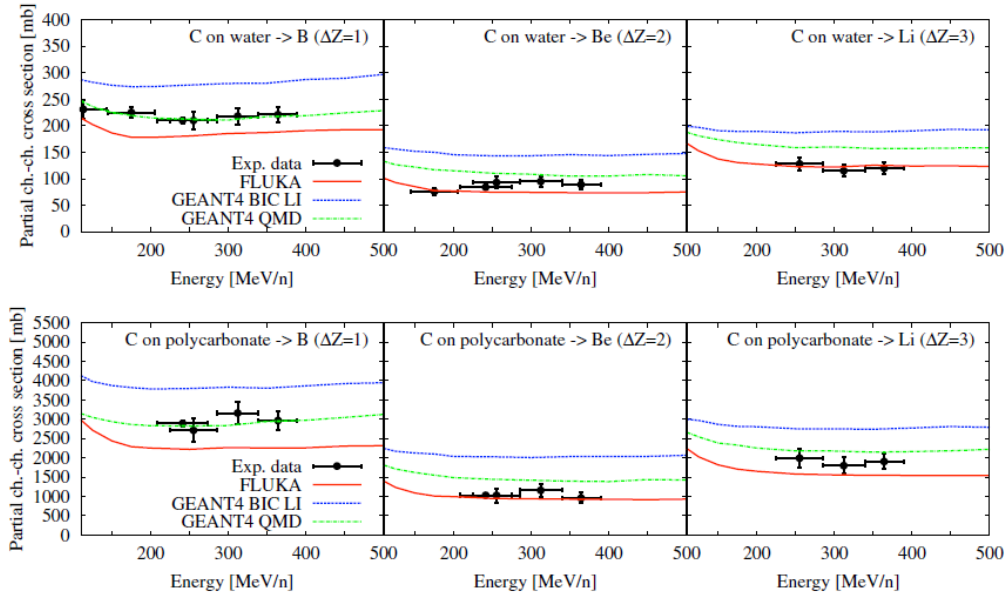


Figure 2.6: PCC cross sections for carbon ions interacting with water and with polycarbonate for Li, Be and B. Vertical error bars indicate the statistical error of the experimental data ([87, 91]) [13]

2.3. FRAGMENTATION CROSS SECTIONS MEASUREMENTS AND BENCHMARKING WITH MC

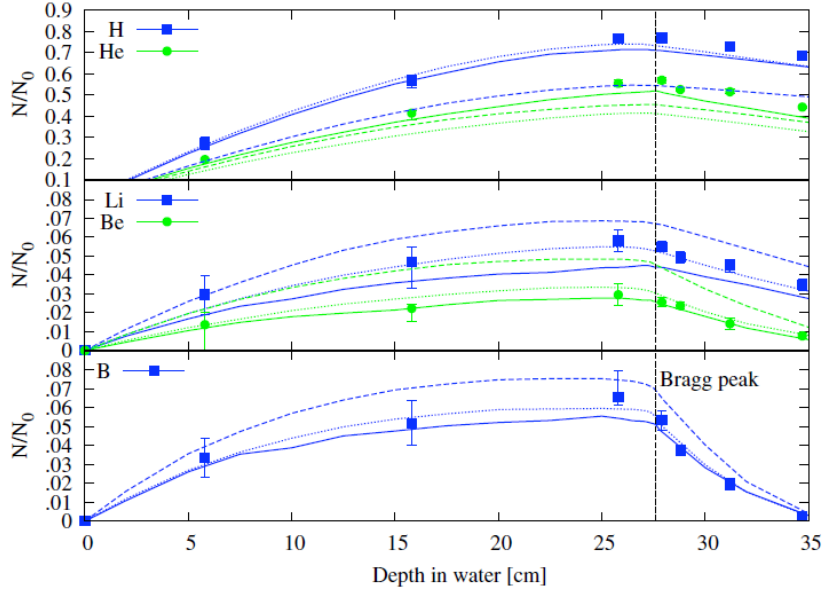


Figure 2.7: Fragment build-up curves in water of a 400 MeV/nucleon carbon beam as a fraction of primary carbon ions N/N_0 . Experimental data are shown as points ([94]). Simulations done for FLUKA (solid) and for GEANT4 using the BIC LI (dashed) and the G4QMD (dotted) model are displayed as lines. The dashed vertical line indicates the position of the Bragg peak [13]

mentation experiments aims to measure the double differential fragmentation cross section respect to the emission angle θ and kinetic energy E of the fragments.

Recently two measurements of single and double differential fragmentation cross sections of carbon ions on different thin targets have been performed at LNS [18] and GANIL [19, 20] at 62 MeV/nucleon and 95 MeV/nucleon carbon beam energies respectively, using detectors with large acceptance and high resolution. Large discrepancies have been observed with respect to existing nuclear models, implemented in MC codes, for differential and double-differential cross sections [99]. In Fig. 2.8 the DDCS measurements for a 95 MeV/nucleon carbon beam energy impinging on a carbon target [19, 20] are compared with the ones obtained using different GEANT4 nuclear models.

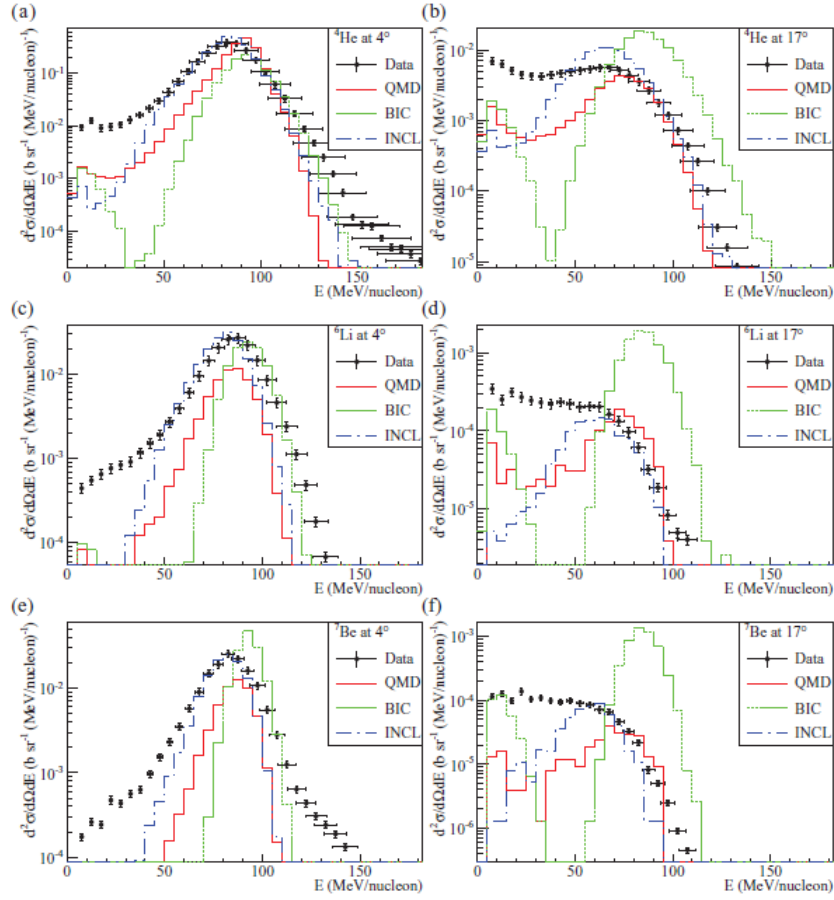


Figure 2.8: DDCS for the production of ${}^4\text{He}$, ${}^6\text{Li}$, and ${}^7\text{Be}$ isotopes at 4° and 17° . Black points are experimental data [19]. Histograms are for simulations with QMD, BIC, and INCL models coupled to the Fermi Break-Up de-excitation model [99, 98]

2.4 Nuclear fragmentation effects in particle therapy applications

At the energies of several hundred MeV/nucleon, required for particle therapy applications, the radiation field is significantly affected by nuclear fragmentation processes. These processes lead to an attenuation of the primary beam flux and to the

2.4. NUCLEAR FRAGMENTATION EFFECTS IN PARTICLE THERAPY APPLICATIONS

build-up of lower Z fragments with the increasing penetration depth (Fig. 2.7). As a consequence of the first effect, a part of the beam particles will not deposit their energy up to the Bragg peak. Due to fragmentation of the primaries and subsequent de-excitation, a distributed fluence of mainly projectile-like nuclei, light clusters, nucleons and prompt γ is produced. Target nuclei fragmentation contributes generally with a negligible part to the overall fluences. Most of the charged fragments have smaller size but a similar velocity of the projectile. Because of the A/Z^2 scaling of the range for particles with the same velocity, these fragments will deposit their energy at penetration depths beyond the projectile Bragg peak. This produces a dose tail beyond the Bragg peak called fragmentation tail. The angular distributions of such fragments are mainly forward directed, but with an angular spread much larger than the lateral spread of the primary beam caused by multiple Coulomb scattering [100, 102].

The fragment build-up curves in water for a 400 MeV/nucleon carbon beam are shown in Fig. 2.7: hydrogen and helium fragments are the most abundant. The heavier fragments, from $Z = 3$ to $Z = 5$, have a range close to the range of the projectile and slow down shortly after the Bragg peak. Hydrogen and helium fragments have much longer ranges and produce the longer part of the dose tail. The FLUKA simulation [103] of the depth dose profile of the Bragg curve and the attenuation of the primary beam, shown in Fig. 2.9, reproduce very well the experimental values for all the depths. The actual dose distribution along the beam path (solid line in the left panel of Fig. 2.9) is different from that resulting by the passage of primary ions which did not undergo nuclear interactions (dashed line in the left panel of Fig. 2.9). The impact of these effects increases as a function of the beam energy or penetration depth (see Fig. 2.10). For example, for a ^{12}C beam of 200 MeV/nucleon, travelling in water, about 30% of the primary ions are involved in nuclear reactions and do not reach the Bragg peak, whereas at 400 MeV/nucleon (see the right panel of Fig. 2.9) this fraction goes to 70% [94]. This change of beam composition is partially present also for proton beam: for a proton beam at 150 MeV only the 80% of the primary particles reach the Bragg peak. Secondary fragments are due to target fragmentation only, so their velocity is very small: the

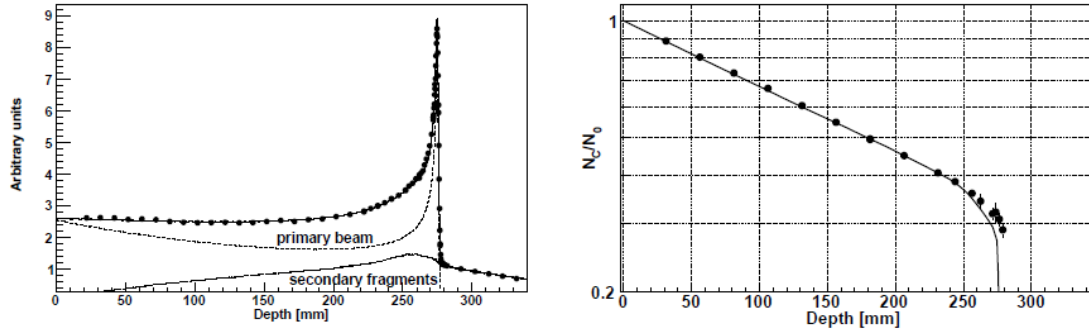


Figure 2.9: Bragg curve (left panel) and beam attenuation profile as a function of depth in water (right panel) for a 400 MeV/nucleon carbon beam. The points represent the experimental data [94] while the solid lines represent the FLUKA simulation [103]. In the left panel the simulated dose contribution from primary ^{12}C ions and secondary fragments is also reported [104]

range do not exceed few μm and they deposit their energy close to the collision location.

The nuclear interactions of the proton beam have an effect also on the total amount of energy which is deposited in the absorber: the energy needed for the fragment production results in a beam energy depletion. At the quoted example energy of 150 MeV, the integral of the Bragg Curve is only about the 97% of the total.

In summary, the intrinsic precision related to the physical dose-depth profile of a charge particle can be partially deteriorated by nuclear fragmentation processes. Nuclear interactions produce a distortion of the dose longitudinal and transverse profile, due mostly to the projectile-fragments build-up. These lighter fragments have different RBE and contribute to the deposited dose all along the primary carbon beam attenuation. For these reasons the physical beam models included in treatment planning programs for light ion irradiation of cancer patients have to take into account the effects of nuclear fragmentation and comparison with experimental data is needed for the validation process.

2.4. NUCLEAR FRAGMENTATION EFFECTS IN PARTICLE THERAPY APPLICATIONS

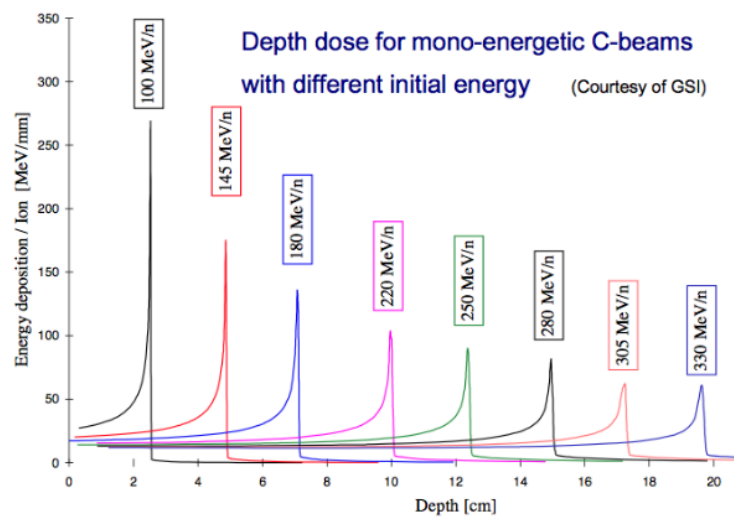


Figure 2.10: With increasing penetration depth the peak-to-entrance dose ratio becomes gradually smaller, mainly caused by the exponentially diminishing flux of primary ions. The buildup of lower-Z fragments is clearly visible in the dose tail behind the Bragg peak at larger depths. Additionally, the Bragg peaks are increasingly broadened by straggling.

Chapter 3

The FIRST experiment

The FIRST (Fragmentation of Ions Relevant for Space and Therapy) experiment [21] at the SIS accelerator of the Helmholtz Center for Heavy Ion research (GSI) was designed and built by an international collaboration to study the fragmentation of light ions on thin targets for particle therapy and space radiation applications. In particular, its purpose is to measure the double differential cross sections, with respect to kinetic energy and scattering angle, of fragments produced in nuclear inelastic interactions of ^{12}C ions with thin targets in the energy range between 100 and 1000 MeV/nucleon. An initial set of data was collected in August 2011 using a 400 MeV/nucleon ^{12}C beam impinging on a 0.5 mm gold target (about 4.5 M events) and on a 8 mm composite target (24 M events). In addition 7 M events have been collected for calibration and alignment studies, in special runs in which the target has been removed or the magnetic field switched off.

The elemental composition of the composite target is given in Table 3.1. In spite of the presence of heavy elements, C, O, P and Ca, that constitute the 85% of the elemental composition of the target, are elements constituting the human body, and so of interest for particle therapy applications. La and Cr are totally absent from human body and have to be considered a contamination.

A detailed description of the detectors used in the experiment and of the running conditions is presented in the following sections, including the main results from

element	percentage of atoms (%)
C	35 %
O	47 %
Cr	8 %
La	7 %
P	2 %
Ca	1 %

Table 3.1: Elemental composition of the composite target.

calibration studies made with the data collected at GSI. The complete analysis of the data collected by the FIRST experiment will be described in the following chapter 4.

3.1 The experimental setup

A MC simulation of a ^{12}C beam at 400 MeV/nucleon impinging on a carbon target has been developed using the FLUKA code [45] to design and optimize the detector [105]. The results of such simulation, concerning energy and angular distributions of the fragments produced in the collision with the target, are shown in Fig. 3.1 and in Fig. 3.2, respectively: the number of all the fragments produced in the target in a certain energy bin (N_{prod}) divided by the number of initial ^{12}C ions ($N_{\text{prim C}}$), normalized by the bin width (MeV/nucleon, sr) for the energy (angular) spectra, are shown as a function of the fragment energy (angle). While most of the fragments are forward emitted and with about the same kinetic energy of the ^{12}C beam, a not negligible fraction of the light $Z = 1, 2$ fragments are produced with large angles and a wider kinetic energy distribution. As expected from simulation (see chapter 2) the most of emitted particles are fragments forward peaked, due to projectile fragmentation, with energies/nucleon and velocities distributed around the ^{12}C beam energy/nucleon. The contribution from target-fragments, isotropically

distributed in the space, is expected to have lower energy.

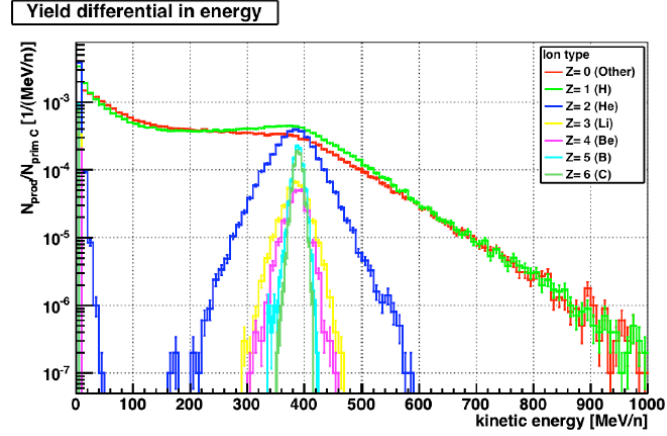


Figure 3.1: Kinetic energy distribution of the fragments produced by a 400 MeV/nucleon ^{12}C beam on a carbon target. $N_{\text{prod}}/N_{\text{prim C}}$ is the yield of fragments per primary carbon ion (FLUKA)

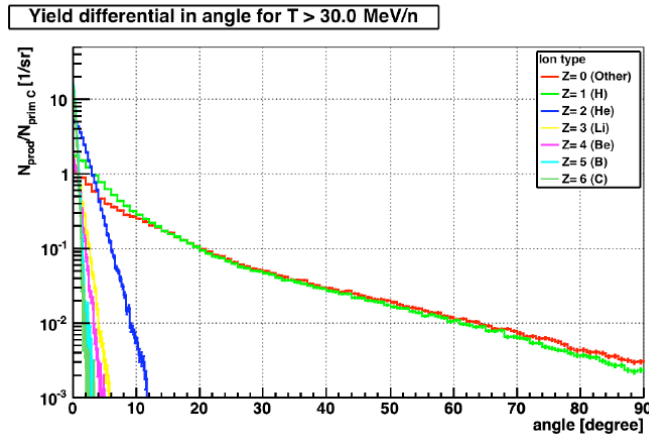


Figure 3.2: Angular distribution of the fragments produced by a 400 MeV/nucleon ^{12}C beam on a carbon target. $N_{\text{prod}}/N_{\text{prim C}}$ is the yield of fragments per primary carbon ion and steradian with a kinetic energy > 30 MeV/nucleon (FLUKA)

3.1. THE EXPERIMENTAL SETUP

A schematic view of the FIRST experiment set up is shown in Fig. 3.3. The detector is partly based on an already existing set up made of a dipole magnet (ALADIN), a time projection chamber (TPC-MUSIC IV), and a time of flight scintillator system (ToF-Wall). This pre-existing set up has been integrated with newly designed detectors in the Interaction Region (IR), around the target (placed in a target changer mechanical system), where the impinging beam and produced fragments are studied. The IR is in air: this choice greatly helps the design and the running of the IR detectors. Two regions with very different dimensions can be distinguished, as shown in Fig.3.3: the IR is of the order of some tens of centimeters, while the devices that detect the fragments, after magnetic bending, have typical dimension of meters.

In Fig. 3.4 a technical drawing of the IR is shown. All the detectors of this region have been tested at the 80 MeV/nucleon ^{12}C beam of the Superconducting Cyclotron at the LNS laboratory (Laboratori Nazionali del Sud) or at the BTF (Beam Test Facility) 510 MeV electron beam at the LNF laboratories (Laboratori Nazionali di Frascati) of the INFN [106, 113, 108].

The FIRST apparatus is composed of several subdetectors optimized for the detection of all the charged fragments produced by the interaction of a ^{12}C ion with the target up to a maximum aperture angle of 40° with respect to the beam axis. For each subdetector a wide dynamic range is required because the energy released by the fragments ranges from ~ 2 MIPs (Minimum Ionizing Particles) for protons to ~ 100 MIPs for carbons. Moreover all the detectors along the ^{12}C beam and the fragments trajectories were designed to minimize the secondary fragmentation inside them. A ^{12}C ion, before interacting with the target (TG), as a first step, impinges on the start counter (SC), a thin scintillator that monitors the number of ^{12}C ions in the beam, provides the trigger of the experiment and start the Time of Flight (ToF) measurement. Afterwards the beam goes through the Beam Monitor (BM), a drift chamber that measures the direction and the impact point on the target [106]. The fragmentation vertex produced in the interaction with the target is reconstructed with a silicon pixel detector (VTX), located just after the target, that has a track angular acceptance of $\theta = 40^\circ$ [107, 108]. The forward fragments

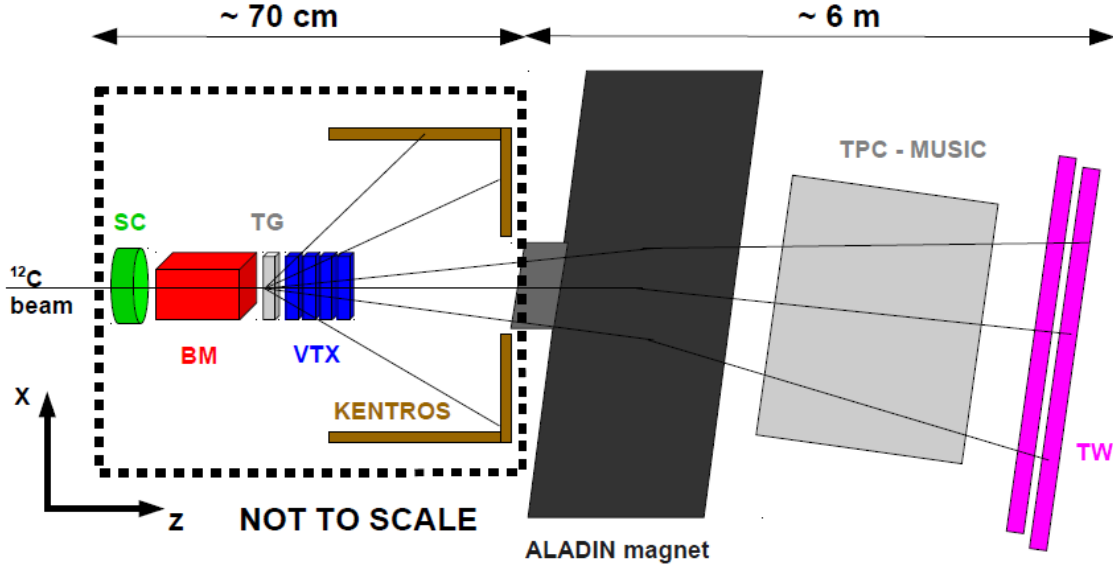


Figure 3.3: Schematic view of the FIRST detector set up. The lines show the path of the fragments produced in the target (TG). The detectors in the interaction region are a start counter (SC), a beam monitor (BM) a vertex detector (VTX) and a thick scintillator system (KENTROS). The fragments tracks bended by the ALADIN magnet are detected by the ToF-Wall (TW), a large area hodoscope of two walls of scintillator detectors

produced with polar angle $\theta \lesssim 6^\circ$ enter in the angular acceptance of the ALADIN dipole magnet [109]. The trajectory and the rigidity (momentum over charge ratio, pc/Z) of such fragments are reconstructed using the magnetic bending provided by the magnet, and by matching the fragments position on the ToF-Wall (TW), a large area hodoscope formed of two scintillator layers [110].

The large volume time projection chamber (TPC-MUSIC IV [111]), was placed after the ALADIN magnet and before the TW, aiming at the measures of track directions and energy releases, but could not be operated during the data taking due to an anomalous increase of the current in the main cathode. The effects of this lack on the tracking capability of the FIRST apparatus, on the fragments identification and on the FIRST results will be discussed in chapter 5, where a

3.1. THE EXPERIMENTAL SETUP

possible upgrade for the FIRST detector will be proposed. The experiment full simulation takes this detector into account in order to properly evaluate the material traversed by each fragment before reaching the TW and accounts for a possible secondary fragmentation.

The VTX and the TW detectors are the only two available detectors able to perform the cross section measurement for the forward emitted fragments in the angular acceptance of the ALADIN magnet ($\theta \lesssim 6^\circ$). The tracking algorithm uses an iterative procedure that matches the VTX tracks and the TW hits detected in each event: special care is needed while performing the extrapolation from the VTX to the far away (~ 6 m) TW. The tracking system alignment has been achieved using the data with non-interacting carbon ions, using dedicated runs without target.

The particle charge identification is performed measuring the energy loss and the ToF provided by the TW. These quantities allow the reconstruction of the velocity, of the momentum and of the mass of the produced fragments.

The fragments emitted outside the angular acceptance of the ALADIN magnet, mainly light ions (p, d, t, ^3He and ^4He ; see Fig. 3.2), are detected by KENTROS (Kinetic ENergy and Time Resolution Optimized on Scintillator [112]), a thick scintillators system organized in a cylindrical shape. The analysis described in this thesis is focused on the measurement of the differential cross sections for forward peaked fragments emitted in the magnet angular acceptance. For this reason the KENTROS detector is not used in the following analysis.

The data taking was performed using the beam provided by the SIS accelerator (Heavy Ion Synchrotron) of the GSI laboratories in Darmstadt (Germany) with the apparatus mounted in the Cave C, where the large dipole magnet (ALADIN) was placed. The reference system used in the experiment is shown in Fig. 3.3: the beam moves in z positive direction, x is in the horizontal direction, y defines the direction of the ALADIN magnetic field, so that tracks are bended in the x-z plane. The SIS accelerator beam rate was in the range of kHz with a Gaussian shape in the transverse plane of 5 mm size (FWHM). The beam rate was constrained by the long read-out time of the VTX pixel detector of about 115 μs . The SC has been used

to trigger the data acquisition (DAQ) using a minimum bias strategy: whenever a ^{12}C ion was detected inside the SC the event was acquired. The time acceptance windows of the TDCs (Time Digital Converter) and the duration of the ADC (Analog Digital Converter) gates are of the order of $1\ \mu\text{s}$ for all the detectors used in FIRST, with the exception of the VTX detector which integrates hits collected in a much longer time.

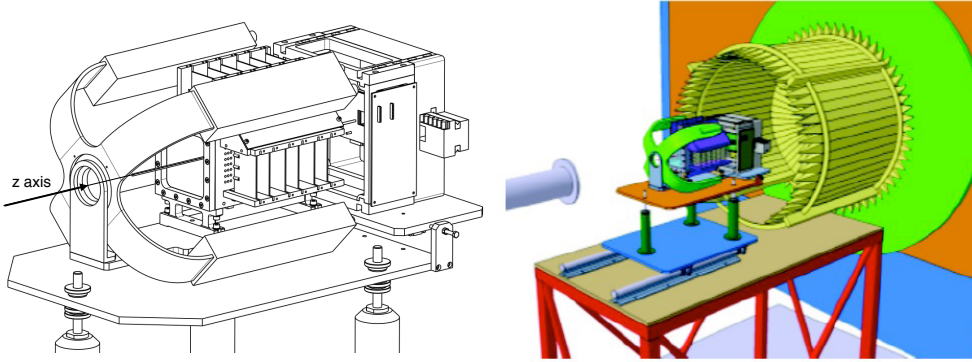


Figure 3.4: Details of the detectors in the IR. On the left the detectors along the beam z axis. In order are shown the SC, the BM and the aluminum box that encapsulates the target holder and the VTX. On the right also KENTROS (with cylindrical shape) and the ALADIN magnet are visible.

3.1.1 The Start Counter

The Start Counter (SC) [106, 113] is a $150\ \mu\text{m}$ thick scintillator, made of a EJ-228 fast scintillator foil, with a radius of 26 mm. As shown in Fig. 3.5, the light produced in the scintillator is collected radially by 160 optical fiber grouped in four bundles and read by fast PMT Hamamatsu H10721-210 with 40% of quantum efficiency. The thickness of the scintillator was minimized to reduce the pre-target particle interaction probability, that is less than 1% with respect to the on-target one. The SC, placed 20 cm before the target (Fig.3.4), provides the trigger signal to the whole experiment and the measurement of the total number of ^{12}C ions used for the cross

3.1. THE EXPERIMENTAL SETUP

section measurement. The SC also gives the reference time for all the other detectors, allowing the measurement of the drift time inside the BM and of the fragments ToF, matching the TW information. The SC performances have been evaluated with data collected with the FIRST experiment showing an excellent stability during the whole data taking. An efficiency with mean value of $(99.7 \pm 0.15)\%$ has been evaluated requiring a majority of three PMT signals out of four. A good time resolution with an average value of $\sigma_t = (150 \pm 2)$ ps has been measured applying a threshold of 120 mV.

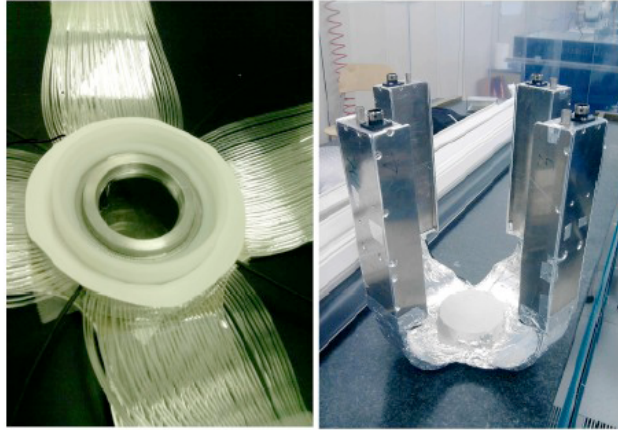


Figure 3.5: Details of the Start Counter: the thin scintillator foil and the optical fibers grouped in four different arms.

3.1.2 The Beam Monitor

The Beam Monitor (BM) is a drift chamber with twelve layers of wires, with three drift cells per layer, centered around the sense wires (Fig. 3.6). Planes with wires oriented along the x-axis and the y-axis alternate in such a way to reconstruct both the orthogonal profiles of the ^{12}C beam. The cell shape is rectangular ($16 \text{ mm} \times 10 \text{ mm}$) with the long side orthogonal to the beam. In each view two consecutive layers are staggered by half a cell to solve the left-right ambiguities in track reconstruction [106, 113]. The twelve planes (six on each “view”) provide tracking redundancy

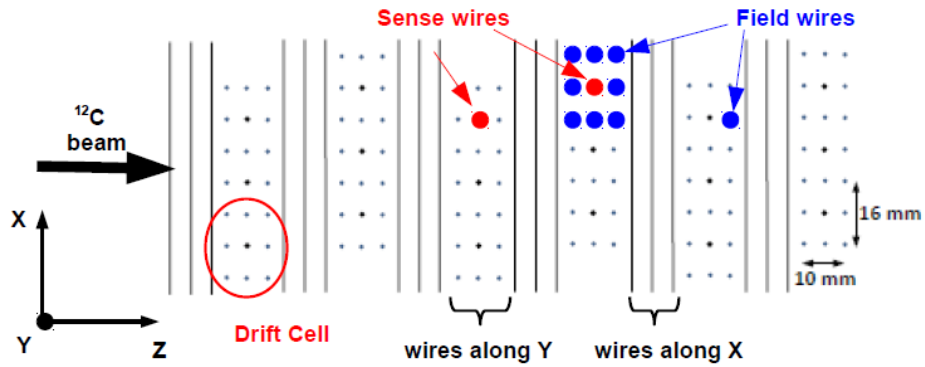


Figure 3.6: BM drift cells: in each view two consecutive layers are staggered by half a cell to solve the left-right ambiguities in track reconstruction

and ensure a high tracking efficiency and an excellent spatial resolution. The BM was operated at atmospheric pressure, at the working voltage of 1.8 kV in Ar/CO₂, 80/20 gas mixture. A technical drawing of the chamber is shown in Fig. 3.7.

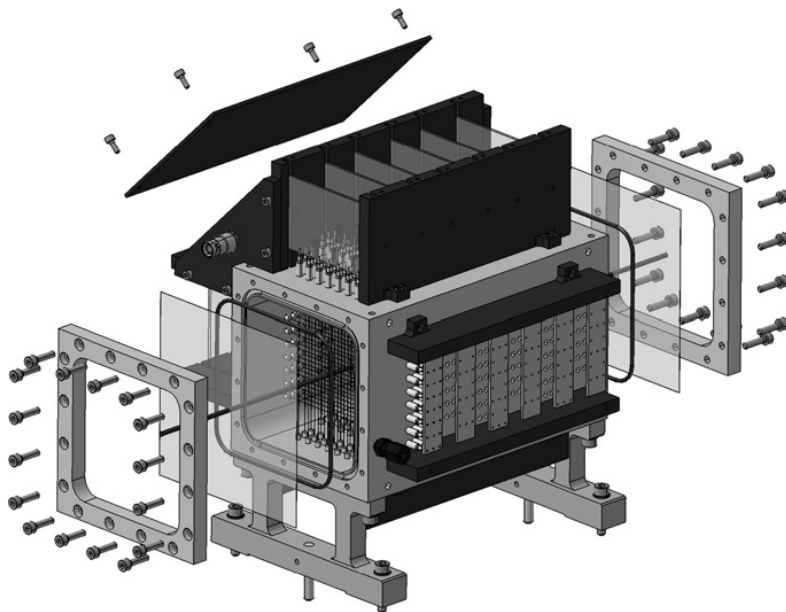


Figure 3.7: Technical drawing of the BM drift chamber.

3.1. THE EXPERIMENTAL SETUP

The BM detector is placed between the SC and the target and is used to measure the direction and impinging point of the ^{12}C ion on the target, a crucial information needed to address the pile-up ambiguity in the VTX detector, due to its long read-out time. In fact the BM read-out time is fast enough to ensure that tracks belonging to different events cannot be mixed.

In pile-up events, the vertices reconstructed in the VTX detector are randomly distributed with a Gaussian shape dictated by the transverse size of the beam of about 5 mm (FWHM). According to the vertexing algorithm (see § 3.1.3), the positions of the vertices reconstructed by the VTX for each event are compared with the position of the BM track extrapolated to the target, and only the closest vertex to the BM extrapolation is selected as matched vertex. For this reason a precision of few hundred μm in the impact point provided by the BM is needed to discriminate the right vertex in pile-up events, together with a good alignment between BM and VTX.

The BM efficiency was measured to be $\sim 96.8\%$ and was stable during the run as shown in Fig. 3.8 (black triangles) with the largest variation of $\sim 3\%$. The mean track spatial resolution was measured to be $\sigma_x \sim 140 \mu\text{m}$. Such precision in the impact point allows to discriminate the right vertex in pile-up events.

The BM and the VTX detectors have been aligned one with respect to the other using calibration events taken without any target, with tracks traversing both detectors without any fragmentation or scattering. The alignment constants were tuned by minimizing the distance between the two predicted track intersections with a virtual plane in the target position and the difference between the track parameters (like the angle with respect to the beam axis). After the alignment a bias in the VTX - BM residual distribution smaller than 200 μm and a resolution of the order of 300 μm for the x coordinate is obtained, with similar results for the y coordinate.

3.1.3 The Vertex Detector

The Vertex detector (VTX) is a silicon pixel detector placed immediately after the target along the beam direction and used to measure the trajectory of charged

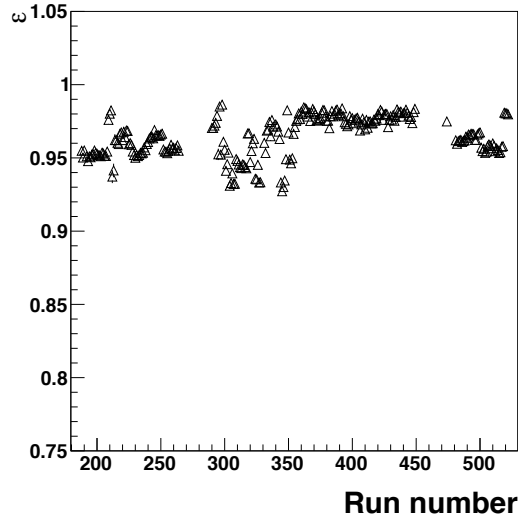


Figure 3.8: BM tracking efficiency (black triangles) as a function of the run number. The small fluctuations ($\leq 3\%$) that can be observed against the mean value of 96.8% are due to the changes in the beam position, as well as to changes in the temperature and pressure of the gas mixture.

particles coming out from the target, with an angular coverage of $\pm 40^\circ$ and an angular resolution better than $\sim 0.3^\circ$ for the two tracks separation. These features enable a good fragmentation vertex reconstruction.

The VTX is composed of four layers each consisting of two MIMOSA-26 (M26) silicon pixel sensors [114, 115] glued on the two sides of a printed circuit board (PCB), as shown in Fig. 3.9. The sensitive area of each sensor is $10.6 \text{ mm} \times 21.2 \text{ mm}$ covered by 576 rows and 1152 columns of pixels with $18.4 \text{ }\mu\text{m}$ pitch. The thickness of about $50 \text{ }\mu\text{m}$ per sensor allows to minimize the lateral straggling of the impinging particles and to reduce the secondary fragmentation inside the sensor at a level of a few per cent, with respect to the on-target one. This choice ensures a good compromise between the need of having redundancy in the track reconstruction and of minimizing the sensor total thickness.

The energy deposited by a ionizing particle impinging a M26 sensor produces charge carriers that are collected by a number of adjacent pixels. The read-out

3.1. THE EXPERIMENTAL SETUP

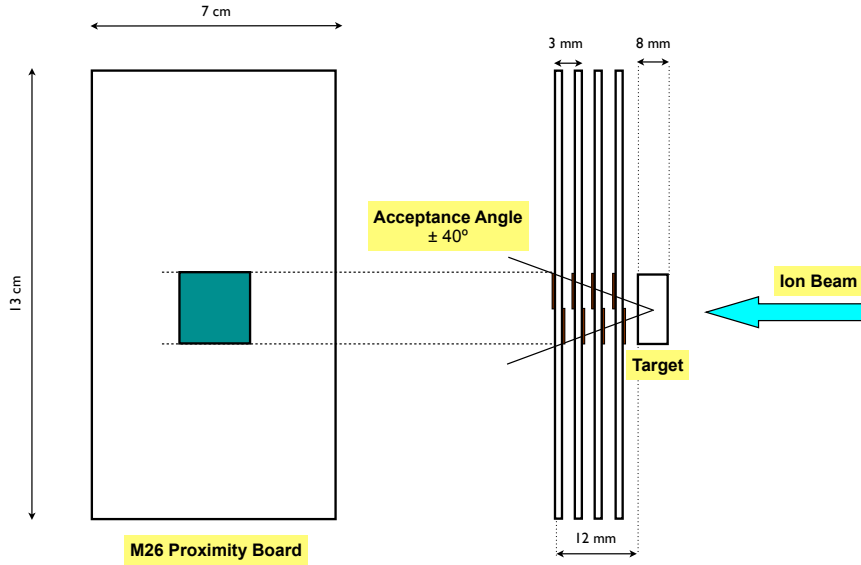


Figure 3.9: Sketch of the VTX detector arrangement: following the target the four PCB planes, each housing the two M26 sensors, one on each side are visible. The M26 sensors are placed over a square hole in the PCB itself obtaining an active volume of $2 \times 2 \text{ cm}^2$.

gives a binary response: the pixel fires when the charge deposited is higher than a given threshold. All the pixels are read-out per column with a row read-out time of 200 ns for a total read-out time of 115.2 μs per sensor. At the end of each column a discriminator is used to produce the input to the following zero suppression logic, that removes the empty pixel information and stores the data in two buffer memories.

The off-line VTX detector data processing starts from the raw data file reading, from which a list of fired pixel is extracted. The VTX reconstruction software [107], consisting of three different algorithms, gathers the fired pixels to identify cluster in each plane (*clustering*), builds tracks with aligned clusters on different planes (*tracking*) and estimates the vertex position from reconstructed tracks (*vertexing*). For each reconstruction step at least two algorithms, providing consistent results, have been implemented [107]. Only the faster algorithm and with a lower fakes number

has been chosen as default for each step and will be briefly described in the following. The alternative algorithms have been used to assign systematic uncertainties.

The clustering algorithm allows to identify and group fired pixels originated by a single ionizing particle and so to reconstruct the crossing point of the particles through the M26 sensor. The algorithm is based on a recursive method looking for the next neighboring fired pixel and is able to reconstruct correctly the clusters with an efficiency higher than 99.9% [107].

The tracking algorithm requires at least three aligned clusters to build a track. Starting from the last plane and proceeding backwards with respect to the beam direction, a path to the position given by the intersection of the BM track with the target is defined. Then all the available clusters on each plane close to the projected path within a given tolerance are selected to build a track. The tracking reconstruction efficiency, evaluated on Monte Carlo simulation events (see § 3.3) is $98.7\pm 0.1\%$, with a measured proportion of fake tracks of $1.99\pm 0.01\%$ [107].

The residuals are defined as the distance between the cluster centroid positions and the fitted track line: their distribution was used to evaluate the tracking resolution of the VTX detector given by the sigma of a Gaussian fit. Fig. 3.10 shows the residuals obtained using ^{12}C ions straight tracks at 400 MeV/nucleon for the x and y coordinates: the resolution in x and y directions is better than $\sigma_{x,y} = 6 \mu\text{m}$ and the fraction of tails outside a 4σ window is smaller than 13%. The distributions for fragmented particle tracks shown more important tails and a resolution better than $10 \mu\text{m}$.

At the end of the tracking procedure a list of reconstructed tracks projected to the target is produced. The vertex is defined as the common position from where two or more tracks are generated. The vertexing algorithm combines the reconstructed tracks in one or more vertices maximizing the probability to find two or more tracks in the same point (Probability Distribution Approach [116, 107]). Using the MC simulation a vertex reconstruction efficiency of $98.6\pm 0.2\%$, with a $2.30\pm 0.01\%$ proportion of fake vertices, has been estimated. The resolution of the vertex reconstruction, evaluated using Monte Carlo events, is better than $10 \mu\text{m}$ in

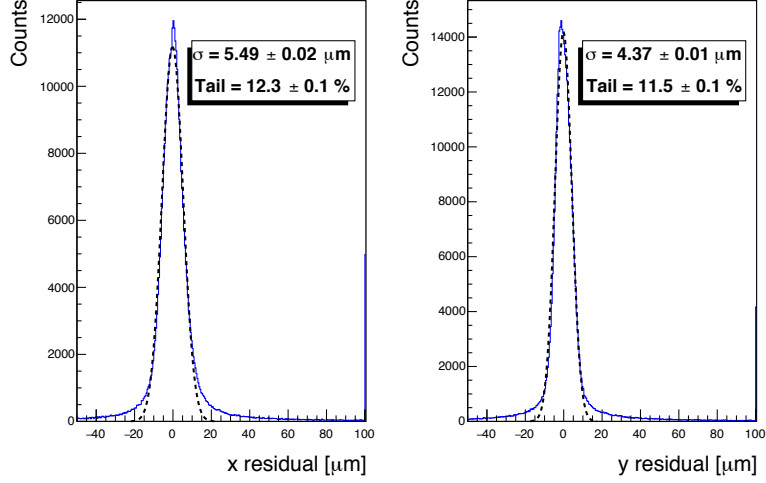


Figure 3.10: Residual distance between the cluster centroid position and the reconstructed track position in the x (left plot) and y (right plot) directions for straight ^{12}C at 400 MeV/nucleon. The data distribution is shown in blue, while the result of a Gaussian fit to the histogram is superimposed in black dashed line.

the x and y directions and better than 50 μm in the z direction [107].

During the M26 sensor read-out time, more than one ^{12}C ion can impinge on the VTX detector, with the result that more than one vertex is reconstructed (pile-up effect). For this reason the BM is used to discriminate the right vertex and address the pile-up ambiguities (see § 3.1.2). With the typical beam rate provided by the SIS of the order of 1 kHz, the total number of pile-up occurrences is relatively large (about 34%). The number of events piled-up in each occurrence can be estimated with the SC detector ($\sigma_t \sim 150$ ps): such number follows a Poisson distribution with $\lambda = 0.74$. The number of piled-up events has been simulated accordingly to such Poisson distribution: it was found that only in $(2.4 \pm 0.1)\%$ of the events the vertex reconstruction algorithm could not disentangle the different vertices.

3.1.4 The ALADIN magnet

The ALADIN (A Large Acceptance DIpole magNet) dipole magnet [109] is a crucial part of the FIRST apparatus, as it provides the measurement of the rigidity (pc/Z) of charged fragments emitted at low angle through the horizontal deflection (x-z plane) of their trajectory in the magnetic field, matching the position information from the TW detector. A vertical magnetic field (parallele to y direction) acts on the particles traveling through the vacuum inside the magnet gap of approximate dimensions $155(H) \times 50(V) \times 230(L)$ cm³. The magnet angular acceptance is limited to 5.7° by a circular collimator of 15 cm diameter positioned at 75 cm from the target. The value of the magnet current has been chosen so that a non interacting beam particle crosses the central region of the TW, and it has been kept constant during the data taking within $\pm 0.5\%$. The corresponding deflection for a 400 MeV/nucleon ¹²C ion is 5.3° .

The values of the magnetic field used in the reconstruction and simulation comes from interpolation of maps measured at GSI along the three coordinate axes on about 10^4 grid points for different current values. The field map consists of a 3D grid of points with step of 5 cm. The actual current value used for the data analysis (~ 680 A) is determined with the MC by requiring that a beam particle crosses the TW in the same positions as measured in special runs with and without the magnetic field. The uncertainty on the magnet current and field scale is limited by the TW position resolution along the x coordinate ($\sigma_x \sim 0.7$ cm) and estimated to be 2.5%.

3.1.5 The ToF-Wall detector

The ToF-Wall (TW) detector is a large area hodoscope (1.10 m long and 2.40 m wide) made of two scintillators layers [110] placed $\simeq 6$ m far from the target, along the trajectory of the ¹²C beam, beyond the TPC (Fig. 3.3). Each layer consists of BC-408 plastic scintillator slats (vertical bars 110 cm long, 1 cm thick, 2.5 cm wide), divided in 12 modules of 8 slats each, for a total number of 192 independent

3.1. THE EXPERIMENTAL SETUP

scintillators. The two scintillators walls are separated by 8 cm from each other: the plane closest to the magnet is called “front wall” (slat numbers: 1-96), while the other one “rear wall” (slat numbers: 101-196). The entire detector is placed inside a nitrogen filled chamber separated by a thin mylar window from the TPC. A picture of the TW detector layout is shown in Fig. 3.11. A brass foil of 0.5 mm thick is placed between the two planes to shield the rear plane from delta electrons produced in the interactions of fragments with the material of the first plane. The two layers are horizontally shifted one respect to the other by 1.25 cm, corresponding to half a slat, in order to maximize the probability that incoming fragments hit at least one slat. The three central slats of the front plane (slat numbers 52, 53 and 54) have a hole in the position of the impinging point of the ^{12}C beam.



Figure 3.11: Picture of the TW detector: the 12 modules of the front wall are clearly visible

The light produced by a charged track impinging on a TW slat is collected at the top and at the bottom of the slat by two R3478 Hamamatsu PMT. Fig. 3.12 shows a layout of the read-out electronics associated to each PMT output. The analog signal from each PMT is split into two branch of the acquisition chain. The first branch consists of a FastBus ADC (model Lecroy 1885F) that provides the energy information exploiting the measurement of the ionization released by the impinging particle. The second branch of the electronic chain consist of a CFD (Constant

Fraction Discriminator), a digital delay module and a TDC (model Lecroy 1875) that provides the time information. Delays lines are used to synchronize the TDC and ADC reading, with the gate and stop signals provided by the general trigger of the experiment. In summary, for each slat crossed by a charged track (a TW hit), four signals (ADC top, ADC bottom, TDC top and TDC bottom) can be obtained. Combining such $ADC_{t,b}$ and $TDC_{t,b}$ informations the energy loss (E_{loss}), the arrival time and the vertical impact position y of the track can be reconstructed. Moreover, the slat number gives the information about the horizontal position (x coordinate) of the TW hit, with a resolution limited by the slat width to $\sigma_X \lesssim 2.5 \text{ cm}/\sqrt{12}$, and also about the fired wall (i.e. z coordinate). The fragment charge is reconstructed by combining the E_{loss} measurements with the start time from SC and the arrival time of the TW, that provide together the ToF of the particle (see § 3.1.5). The ToF measurement is also used to measure the fragment mass in the track reconstruction (see § 4.1).

TW calibration

The ADCs and TDCs have been calibrated to provide the measurements of E_{loss} , ToF and y of each impinging particle. The calibration of such quantities has been performed exploiting dedicated runs called “sweep-runs”, in which data have been collected without any target. In these runs the ^{12}C ion beam has been deflected on the horizontal plane (the y coordinate of the beam is assumed to be 0) over all the slats, varying the magnetic field. In such conditions the beam energy and the beam impinging position (x, y, z) are well known, on average, for each slat. In the next paragraphs a short description of the calibration of the quantities of interest is given. In the following description the scheme shown in Fig. 3.12 on the right can be taken as a reference: when a charged particle impinges on a TW slat, with length L , with vertical impact position y , releasing an energy E_{loss} , the light produced, propagates towards the top and the bottom edges of the slat where is collected and amplified by the PMTs and can be read by $ADC_{t,b}$ and $TDC_{t,b}$.

3.1. THE EXPERIMENTAL SETUP

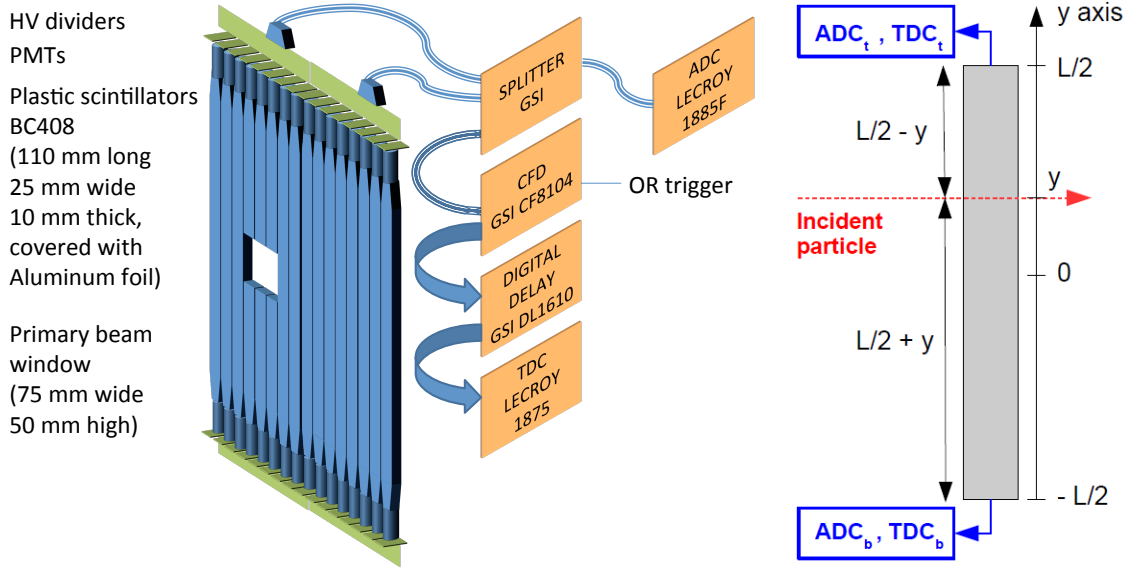


Figure 3.12: On the left: sketch of two TW scintillator modules and of the read-out electronics chain with splitters, CFDs, digital delays, TDCs and ADCs boards. On the right: schematic view of a TW slat, with length L , hit in the vertical impact position y ($-L/2 < y < L/2$), by an impinging particle releasing an energy E_{loss} . The produced light propagates towards the top and bottom edges of the slat where the signal is read by $\text{ADC}_{t,b}$ and $\text{TDC}_{t,b}$.

Energy calibration The charge measured by each ADC, after that ADC pedestals have been subtracted, is proportional to the scintillation light S_{light} released by the incident particle, attenuated exponentially according to the distance from the edge of the slats and to the attenuation coefficient α , that is different for each slat:

$$\text{ADC}_t = K_t \cdot S_{\text{light}} \cdot e^{-\alpha(\frac{L}{2}-y)} \quad (3.1)$$

$$\text{ADC}_b = K_b \cdot S_{\text{light}} \cdot e^{-\alpha(\frac{L}{2}+y)} \quad (3.2)$$

The calibration factors $K_{t,b}$ are constants that take into account several effects as the quantum efficiency and the gain of the PMTs. The ADC pedestals have been determined for each ADC channel with a gaussian fit of the ADC distributions

obtained in dedicated runs with random triggers. The released scintillation light S_{light} can be obtained from the combination of (3.1) and (3.2):

$$S_{\text{light}} = C \cdot \sqrt{ADC_t \cdot ADC_b} \quad (3.3)$$

where $C = e^{\alpha \cdot \frac{L}{2}} / \sqrt{K_t \cdot K_b}$ is a calibration constant. The energy calibration has been obtained applying the semi-empirical Birks' formula [119] that takes into account the non-linear response of plastic scintillators to the ionization density:

$$S_{\text{light}} = \frac{A \cdot E_{\text{loss}}}{1 + B \cdot E_{\text{loss}}} \quad (3.4)$$

The parameters A and B are the calibration factors that finally link the ADC counts with the E_{loss} . They are determined experimentally from the data using the following procedure. For each slat the light distribution presents from one to six peaks corresponding to the carbon peak and its fragments: H, He, Li, Be and B. Fitting these distributions with a number of Gaussian functions equal to the number of peaks, the light mean values can be extracted for each slat (see Fig. 3.13). For each slat a scatter plot of the light mean values vs the corresponding values of E_{loss} , computed using the Bethe-Bloch formula, has been obtained: the energy calibration has been achieved fitting with (3.4) and extracting the calibration factors A and B for each slat (Fig. 3.14). For the external slats, that are not hit by the carbon beam in standard runs, the carbon peak from sweep-runs can be used. Once A and B are known a rescaling of the energy axis can be applied, inverting the Birks' formula (3.4).

ToF calibration The ToF is related to the time measured by the two TDCs according to the following expressions:

$$\text{TDC}_t = \text{ToF} + \frac{(L/2 - y)}{v_{\text{light}}} + \Delta_t \quad (3.5)$$

$$\text{TDC}_b = \text{ToF} + \frac{(L/2 + y)}{v_{\text{light}}} + \Delta_b \quad (3.6)$$

3.1. THE EXPERIMENTAL SETUP

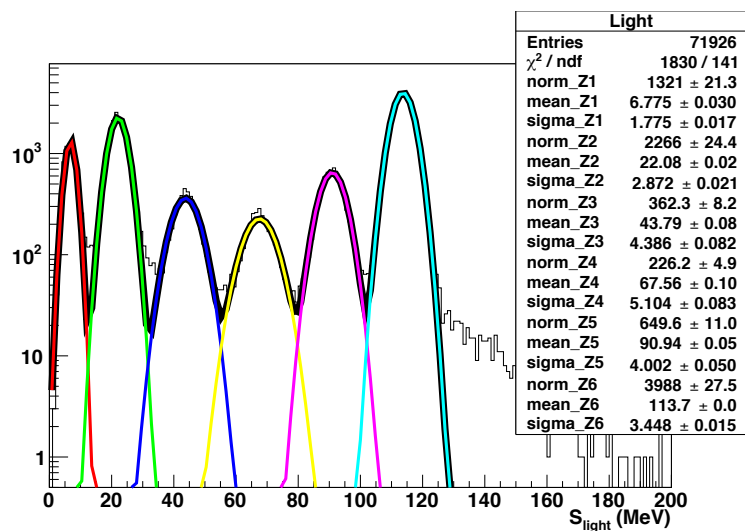


Figure 3.13: Light distribution for slat 48 for all the data production runs. The six peaks corresponding to the carbon and fragments peaks are clearly seen.

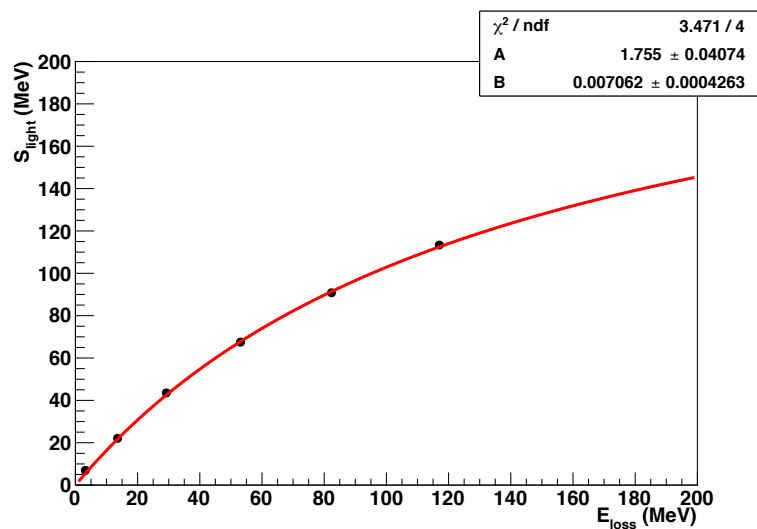


Figure 3.14: Fit with the Birks' law for slat 48 from which the energy calibration factors A and B are extracted.

where v_{light} is the propagation speed of the light in the slat (the measured mean value is 15.6 ± 0.8 cm/ns) and $\Delta_{t,b}$ are the channel delays along the lines and electronic circuits, that have to be determined. The ToF can be obtained taking the sum of (3.5) and (3.6), that is independent of the hit-position in the slat:

$$\text{TDC}_t + \text{TDC}_b = 2 \cdot \text{ToF} + \frac{L}{v_{\text{light}}} + (\Delta_t + \Delta_b) \quad (3.7)$$

The calibration can be achieved fixing the sum $\Delta_t + \Delta_b$. This can be done in “sweep-runs” where $y = 0$ and the ToF can be computed by the known beam energy (i.e. velocity) and the path length to the individual slats. The mean value of $\text{TDC}_t + \text{TDC}_b$ can be extracted from fit for each slat in such a way to obtain the desired sum $\Delta_t + \Delta_b$. Inverting the equation (3.7) the measurement of ToF of charged tracks is achieved.

In addition to the ToF calibration, a data sample has been collected with dedicated runs (“wedge-runs”) in order to take into account the dependence of the arrival time measurement on the energy released by the fragments in each slat. A scan of the TW with the beam impinging an alluminium bar (5 cm thick) placed in front of the scintillator front plane was performed. The time dependence on the released energy (time-walk effect) has been found to be <0.5 ns and thus it has been neglected in the TW hit reconstruction.

y calibration The vertical impact position of the fragments can be obtained using the ADC or TDC information, respectively. The first possibility is to calculate y through the ADCs (y_{ADC}) taking the logarithm of ratio between (3.1) and (3.2):

$$\ln \left(\frac{\text{ADC}_t}{\text{ADC}_b} \right) = \ln \left(\frac{K_t}{K_b} \right) + 2y\alpha \quad (3.8)$$

where the attenuation (α) and the PMT gain ratio (K_t/K_b) are the calibration constants to extract. The calibration parameters have been measured using the positions (y coordinates) of the intercept between the VTX track extrapolation and the TW reference planes. α and $\ln(K_t/K_b)$ can be seen in (3.8), respectively, as the slope

3.1. THE EXPERIMENTAL SETUP

and the intercept of a line and are extracted from a linear fit of $\ln(ADC_t/ADC_b)$ respect to y_{VTX} , performed for each slat.

A second method exploits the TDC values to compute the y coordinate (y_{TDC}), taking the difference of (3.5) and (3.6):

$$(TDC_t - TDC_b) = (\Delta_t - \Delta_b) - \frac{2y}{v_{\text{light}}} \quad (3.9)$$

In “sweep-runs” the vertical coordinate is known ($y = 0$) and the difference ($\Delta_t - \Delta_b$) can be extracted fitting the TDCs difference (3.9). However, it results that the y coordinate measured with the ADCs has better resolution than the coordinate measured using the TDCs information. For this reason, y_{TDC} will be only used for slats in which one of the two ADCs was not working properly and the y_{ADC} can't be computed.

In the case that one TDC is missing, the y is reconstructed using the ADCs, and the remaining TDC can be used to measure the ToF, taking into account the y_{ADC} (single channel calibration; see (3.1) or (3.2)). Slats for which one ADC or both TDCs didn't work properly, do not provide enough informations to reconstruct the TW quantities. Such slats are masked for both data and MC and are not considered in global reconstruction (see § 4.1).

Charge identification algorithm

The charge identification algorithm (Z_{ID}) of the FIRST experiment is based on the TW reconstructed quantities E_{loss} and ToF. The particle charge is fundamental for the reconstruction of the momentum and of the mass of the track (see § 4.1). For each hit, for which both E_{loss} and ToF can be reconstructed, the Z_{ID} assigns a charge to the corresponding track. The TW performances allow the discrimination of six spots in the E_{loss} -ToF plane, related to different fragment charges, as shown in Fig. 3.15: for each spot the Bethe-Bloch curve with the corresponding Z superimposed. The TW Z_{ID} algorithm assigns to a given fragment (a TW hit) the charge that minimizes its normalized distance, in the E_{loss} -ToF plane, with respect to the different Bethe-Bloch curves relative to the different Z hypothesis. A bisection algorithm computes

the distance of each point of the plane from each Bethe-Bloch curve. The distance is normalized, for each Z hypothesis, to the σ_{dist} of the distribution obtained from a Gaussian fit to the distance of each hit to each Bethe-Bloch curve measured in the full data sample. Furthermore, the μ_{dist} from the fit is used to calibrate the normalized distance distribution (see Fig. 3.16). The same Z_{ID} algorithm is implemented for data and MC samples.

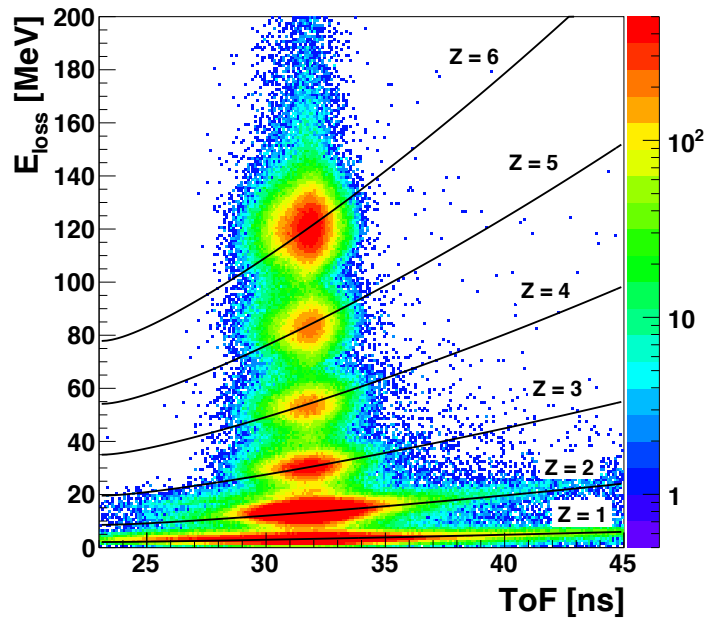


Figure 3.15: Measured E_{loss} vs ToF distribution, for all the TW hits reconstructed in the full data sample. The corresponding Bethe-Bloch curves, fitted on the data sample, are superimposed in black.

TW efficiency

When a particle impinges on a TW slat the produced signal, collected by PMTs and read-out by ADCs and TDC, depends on the E_{loss} and on the vertical impact position of the particle (because of the attenuation of the light propagating in the

3.1. THE EXPERIMENTAL SETUP

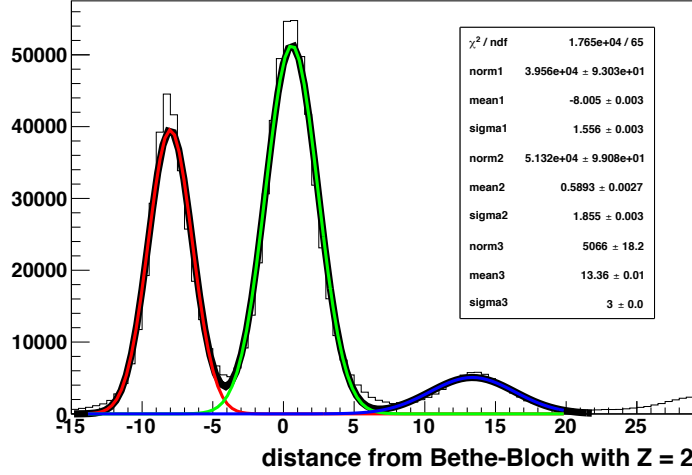


Figure 3.16: Distance distribution from the Bethe-Bloch curve with $Z=2$. The σ_{dist} and the μ_{dist} are extracted from a Gaussian fit to the distribution centered in zero to compute the normalized distance from the $Z=2$ curve.

slat). For a given signal, working ADCs always allow the E_{loss} reconstruction. The same signal can be able or not to trigger the CFDs. For signals below threshold of the CFDs the time information can't be retrieved. Tracks for which is not possible to get any time information have to be considered inefficiencies: the global reconstruction algorithm is not able to assign a mass to these tracks (see § 4.1). Without the ToF is not possible to reconstruct the particle charge. This means that TW detection inefficiencies are mainly due to light fragments (especially protons) releasing a low energy in the slats.

In order to simulate accurately this effect, for each TW channel (top and bottom) the fraction of events with a detected TDC hit has been studied as a function of the ADC counts after pedestal subtraction, as shown in Fig. 3.17 (for slat 33, top). The sharp transition from 0 to 1 (parameterized with a sigmoid fit) corresponds to the minimum ADC counts needed to trigger a TDC hit. The minimum released energy needed to trigger the TDC in each channel is estimated using the calibration parameters and Birks' factors, and is used in the Monte Carlo simulation to discard

hits with an energy below threshold.

The energy threshold is generally below the energy released by a minimum ionizing particle, with a few exceptions. These include specifically the region close to the impact point of the carbon beam, where higher thresholds are set and an efficiency loss for protons of high kinetic energies is observed.

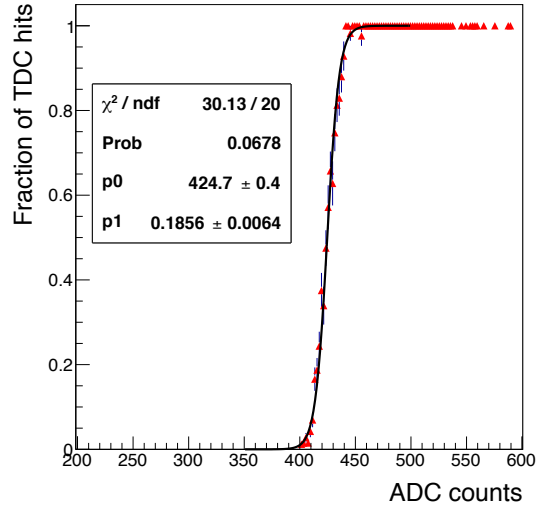


Figure 3.17: Fraction of events with a TDC hit as a function of ADC counts for slat 33 of the TW.

TW resolution

The resolutions of the physical quantities (E_{loss} , y , ToF), reconstructed by the TW, are estimated using tracks for which both hits in the front and in the rear wall are recorded. Both hits have to be compatible with the same track according to their position (slat number and y , within a certain tolerance) and their charge. The distribution of the difference between the values measured for hits in the two planes is built for each charge. The resolutions are estimated from a Gaussian fit to such distributions and then used for the tuning of the Monte Carlo signal processing (see § 3.3).

The y_{ADC} coordinate resolution depends, as expected, on the value of the vertical coordinate itself and it is shown as a function of the energy released in the scintillator by the particle in Fig. 3.18 (top, left). The energy resolutions, obtained on data and MC, are shown in Fig. 3.18 (top, right), as a function of the released energy. The ToF resolution, shown in Fig. 3.18 (bottom, left), is about 800 ps while the y_{TDC} resolution (bottom, right) is 8 cm and is nearly independent of the energy. A fine tuning of MC resolutions is still necessary to improve the data-MC comparisons in Fig. 3.18. However such discrepancies produce an error in the cross section measurement much lower than the systematic uncertainties (see § 4.4) and so are not relevant for the final result.

3.2 The DAQ and the trigger

The read-out of the detector electronics is performed on an event-by-event basis using the Multi Branch System (MBS) [117, 21], a general DAQ framework developed at GSI. In MBS several intelligent bus controllers (CES RIO), running under the real-time operating system LynxOS, perform the read-out of the digitization modules of the individual crates when triggered by dedicated trigger modules. All the trigger modules, one in each read-out crate, are connected via a trigger bus to distribute the trigger and dead-time signals and to provide event synchronisation. Data collected by single controllers are transmitted during the beam inter-spill period via Ethernet to a host PC where they are merged and saved in the standard GSI format by an event-builder. A set of client-server applications allows to control the data acquisition, to configure the detector settings remotely and to perform on-line monitoring of the data quality. MBS can handle easily the different Front-End Electronics standards used by the different subdetectors: FASTBUS, CAMAC and VME. The signals from single detectors are locally processed with NIM electronics to generate trigger primitives. The final trigger logic is implemented in a FPGA programmable VME module, where the local trigger primitives are combined in logic matrices. The accepted triggers for different logical conditions are propagated to the read-out electronics via the trigger bus. Different trigger outputs are generated

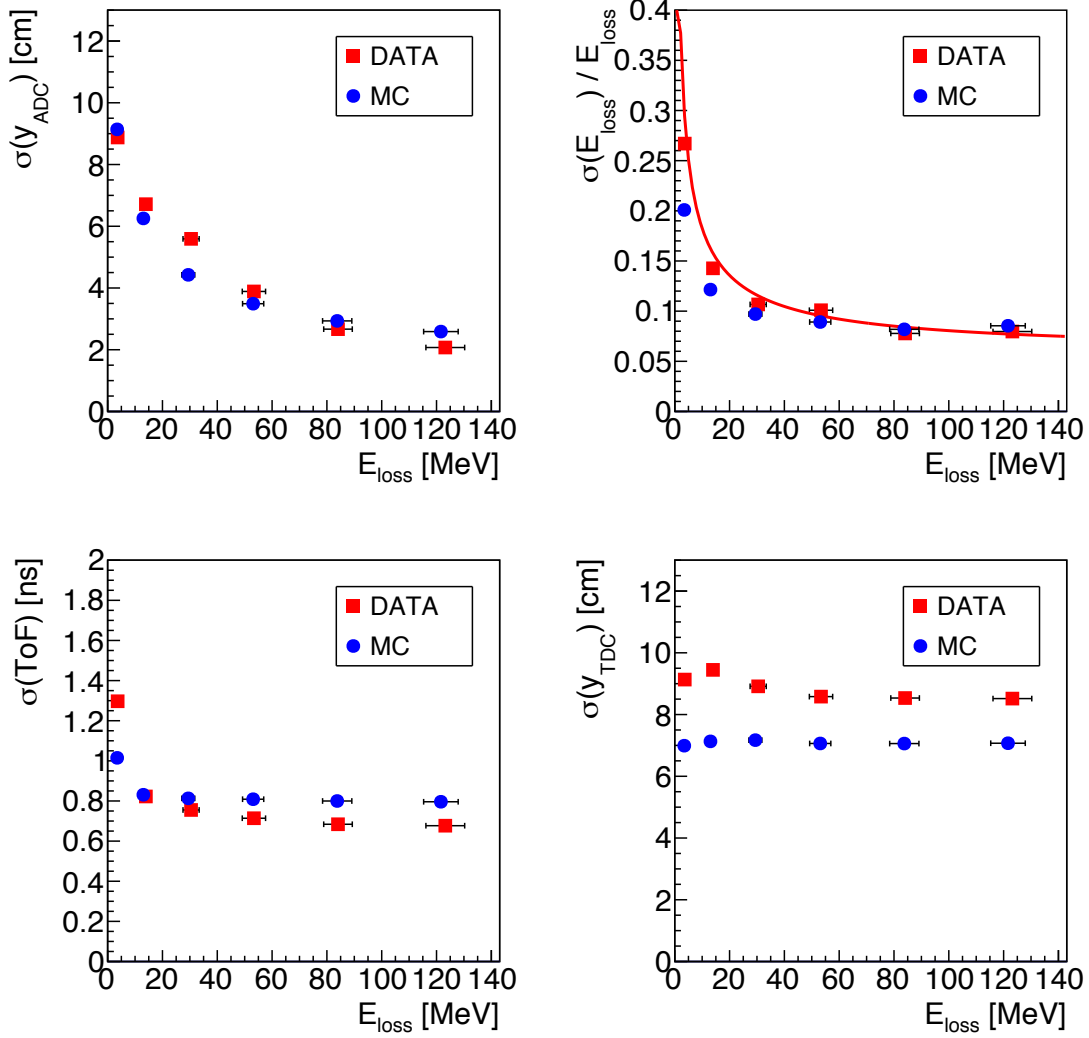


Figure 3.18: Top left: y_{ADC} resolution. Top right: energy resolution. Bottom left: ToF resolution. Bottom right: y_{TDC} resolution. All the distributions are shown for data (red squares) and MC (blue circles) event samples as a function of the released energy. A red line, showing a $\propto 1/\sqrt{E_{\text{loss}}}$ distribution is superimposed to the energy resolution distribution.

with downscale factors or at random times for calibration purposes, while the main physical trigger is based only on the signal from the SC detector, thus providing an unbiased selection of primary beam particles for the data analysis. The typical beam rate during the data taking was around 1 kHz, with instantaneous fluctuations related to the spill structures provided by the SIS.

3.3 The Monte Carlo simulation

The full simulation of the FIRST experiment has been implemented using the general purpose Monte Carlo code FLUKA [45], used with the “HadronTherapy” default setting, which includes accurate modelization of hadronic interactions in the energy range for particle therapy application, with de-excitation and radioactive decays of heavy fragments (see chapter 2). The implementation of the simulation is divided in four different steps:

- detailed description of the experimental setup, detector geometry and materials, to properly evaluate the interaction in all the active detectors and the production of secondary fragmentation outside the target;
- particle transport with the MC code FLUKA, and scoring of basic physical quantities of the tracks (i.e., primary and secondary particles propagated through the experimental volume) and of the hits (i.e., energy depositions of tracks in sensitive detector elements);
- modelling of the subdetector responses and digitization of the hits;
- storing of simulated tracks, hits and digitized signals.

The data flow of the simulation is illustrated in Fig. 3.19. In order to facilitate a flexible and object-oriented coding of the geometry and processing of the MC simulation data, the FORTRAN77 based FLUKA code was interfaced with C++. The simulation of the detector response is written in FORTRAN but the output of the simulation is stored in ROOT files [118] with the same format of the output files

produced during the data taking of FIRST, and processed by a local reconstruction code using the same algorithm used for the data (see § 3.4).

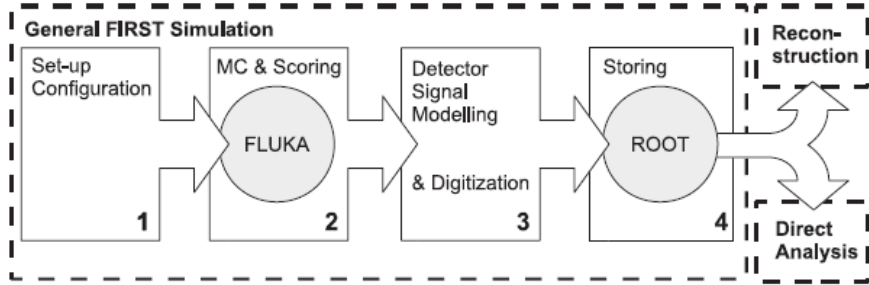


Figure 3.19: Data flow of the simulation.

A sample of 50 million MC events of ^{12}C ions interacting with a composite target (see Table 3.1) and a sample of 50 million of ^{12}C ions interacting with a gold target are used for the analyses described in the following chapter 4. In particular MC simulation is needed for the optimization of the reconstruction algorithm and the evaluation of the efficiencies, angular end kinetic energy resolutions and for the background subtraction. For this purpose each reconstructed track is associated with a MC generated track and the reconstructed variables (kinetic energy, mass, charge, emission angle, momentum) are compared with the corresponding true value at generator level (see § 4.1).

The comparison of E_{loss} , ToF and y coordinate measured from the TW detector for DATA and MC events in which a fragmentation occurred are shown in Fig. 3.20, where the distributions have been normalized to the maximum peak. The fragmentation events are defined as those in which at least one vertex has been reconstructed in the VTX detector and more than one track is associated to it. While the agreement between data and MC for y and ToF is good, the same is not valid for the E_{loss} . This is because in the E_{loss} distribution the different fragments populations depend on the fragmentation cross sections, that are different in data and MC. Instead the y and ToF measurements does not depend on the cross sections but only on the TW detector performances.

3.3. THE MONTE CARLO SIMULATION

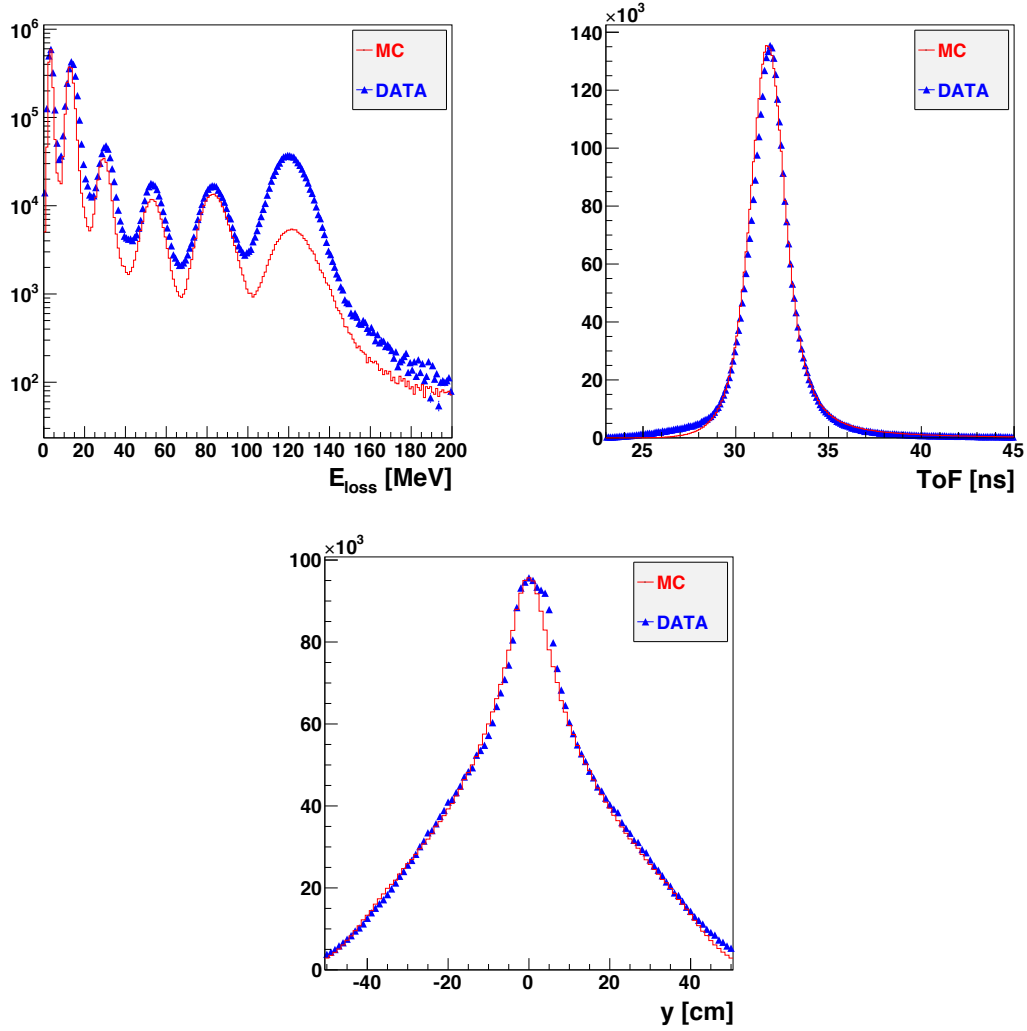


Figure 3.20: Comparison of data and Monte Carlo distributions for TW reconstructed variables in fragmentation events. The data and MC spectra have been normalized to the maximum peak. Top left: E_{loss} . Top right: ToF. Bottom: y coordinate.

3.4 The data/MC reconstruction

The FIRST reconstruction software is divided into two chains that process the raw data recorded during the data acquisition and the output of the simulation, respectively. The raw data acquired during the data taking are stored in a MBS custom format and contain the digitized output from the read-out modules of all the detectors. Similar informations are produced by the FIRST simulation code and are saved in ROOT files. These files are the input to a “local reconstruction” stage (implemented in software codes called “L0 reco” and “L0 mreco” respectively for data and MC). In the local reconstruction level the elementary information from each detector (ADC and TDC measurements, hit position in the VTX, etc...) are processed by applying proper calibration factors to extract physical quantities like the energy released in a scintillator, a time or a spatial information in the detector local reference frame. The reconstruction of each detector is performed at this stage, for example to extract the positions and the directions of the VTX tracks, the charge of a TW hit, the parameters of the BM track. No correlation between different detectors is considered at this level zero of the reconstruction. The results of the local reconstruction are stored in output files in the ROOT format, with the same structure for data and MC. The last stage consists in “global reconstruction” algorithms. In this stage the reconstructed quantities from each detector are combined for the final selection of the fragment tracks, to perform the tracking in the magnetic field of ALADIN and to determine the values of the kinematic variables for each selected fragment. More details on the reconstruction of the final tracks will be provided in next chapter 4.

3.4. *THE DATA/MC RECONSTRUCTION*

Chapter 4

FIRST Analysis

As previously stated in chapter 3, the analysis described in this thesis is limited to fragments produced at polar angles $\theta \lesssim 6^\circ$ with respect to the beam direction and crossing the ALADIN magnetic field. For larger angle production, the fragments cannot enter the magnet region and are detected by the KENTROS calorimeter. Only the informations from the VTX and the TW detectors are used to identify the isotopic composition of the fragments after the interaction with the target, measuring the tracks bending in the x-z plane due to the ALADIN magnetic field. Fragments are reconstructed, in this case, using an iterative procedure providing the value of the rigidity and the trajectory path for each combination of VTX tracks and TW hits detected in the event. From these informations the kinematic variables such as the production angle, the momentum, the kinetic energy and the mass can be computed for each tracks.

The following sections describe the details of how a possible track candidate and its parameters are reconstructed, from each pair of VTX track and TW hit and how the final selection of tracks is performed starting from all the combinations of VTX and TW hits.

An example of a fully reconstructed fragmentation event, in which four fragments produced at small angle enter in ALADIN collimator acceptance, is shown in Fig. 4.1. The little gray box in the bottom left corner of the picture represents the BM, while

the target and VTX detector are not visible in this scale. The KENTROS blue barrel and endcap modules, surrounding the target/VTX region are shown as well. The passage of a ^{12}C ion is detected by BM wires/cells, highlighted in blue. The charged tracks, represented as “dots” in space, produced in the interaction with the target and reconstructed by the VTX detector, are bended in the grey box representing the ALADIN magnet region: before and after that region the magnetic field intensity is negligible and the track trajectory is assumed to be a straight line. Four pairs of magenta bands on the TW, two for each fragment as it traverses both the front and the rear wall, represent the TW slats that have been hit. The TW hits used to build the track are highlighted as green tiny spots.

4.1 The reconstruction algorithm

The global tracking algorithm implements three main steps.

1. The events are pre-selected applying several filters: at least one hit on the TW and one track in the VTX detector have to be reconstructed;
2. For all the preselected events an iterative scan of the matching between VTX tracks and TW hits is performed, producing a list of global track candidates: for each candidate the value of pc/Z is measured.
3. The track candidates are combined and ranked accordingly to the VTX-TW matching quality. The resulting track list, in which each VTX track is used to build only one global track, is then used as input for the cross section measurements.

4.1.1 Global tracking

The global tracks are built by pairing the tracks reconstructed with the VTX and the hits detected by the TW. For this purpose at least a valid VTX track and a valid TW hit are needed. Valid VTX tracks are reconstructed tracks that are produced

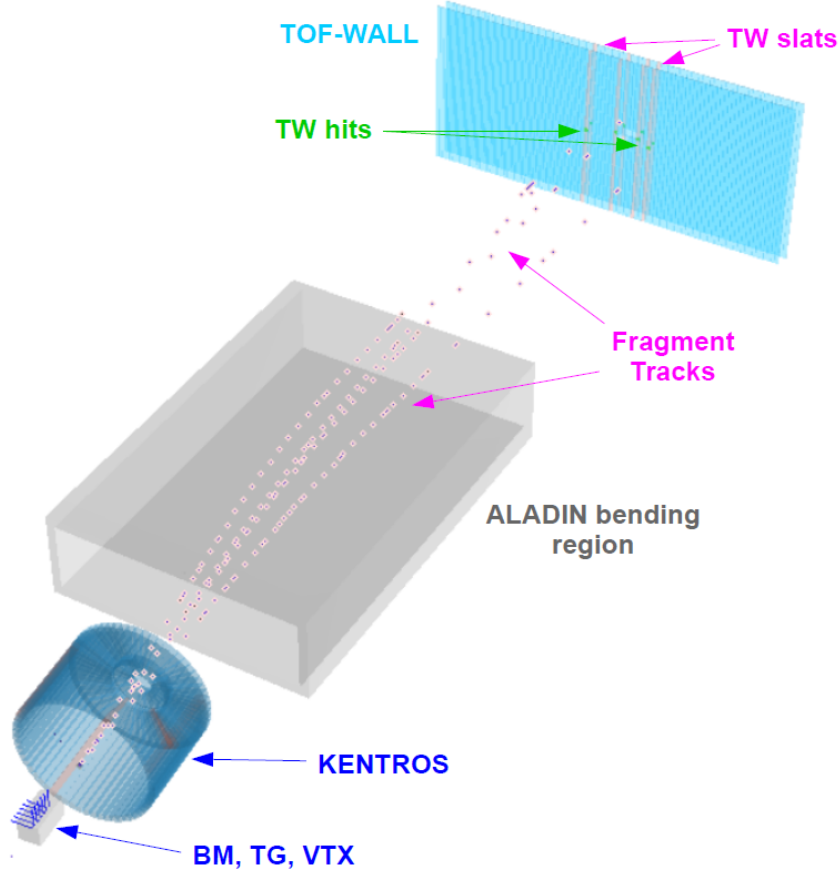


Figure 4.1: 3D view of a fully reconstructed fragmentation event, with four fragments produced in the small angle region. Fragment tracks are built by pairing tracks reconstructed in the VTX detector (not visible in this figure) with the hits detected by the TW (in green in the top right light blue region that represents the TW). The tracks are represented as dots connecting the target/VTX region with the green dots on the TW. The magnet region is represented as a grey box between the KENTROS detector and the TW.

within the acceptance window of the ALADIN magnet ($\theta \lesssim 6^\circ$). In case of pile-up events, for which more than one vertex is reconstructed by the VTX detector, only the VTX tracks produced from the vertex closer to the BM track are selected (see

4.1. THE RECONSTRUCTION ALGORITHM

§ 3.1.3). Events where the BM track is not available for the identification of the right vertex are discarded as well. Only TW hits for which all the TW quantities E_{loss} , ToF and y coordinate can be reconstructed and a charge can be assigned are considered: this is possible only for slat with both ADCs and at least a TDC are properly working (see § 3.1.5).

For all the preselected events, all the possible combinations of VTX tracks and TW hits are considered in such a way to produce a list of global tracks candidates: each VTX track matched with each TW hit can constitute a potential global track.

For each selected global track candidate the charge and the ToF are measured by the TW, while the track origin position (x, y, z) and direction (θ and ϕ) before the magnet are provided by the VTX detector. Each candidate track is propagated from the target as a straight line towards the magnet, where the track is bended according to the Lorentz force differential equation in momentum p. A minimization algorithm, based on an initial momentum guess and on the Runge Kutta method for solving the Lorentz differential equation and providing the final momentum outside the magnet, determines the optimal value of pc/Z and the corresponding trajectory that matches the VTX track before the magnet and the TW x-position after the magnet. The particle path L can be determined from the trajectory. The particle momentum is determined multiplying the value of pc/Z from the tracking algorithm by the measured charge: obviously a bad charge identification produces a wrong momentum assignment. The particle velocity measurement is given by ToF and track path:

$$\beta = \frac{L}{\text{ToF} \cdot c} \quad (4.1)$$

The ToF is measured with respect to the reference time provided by the SC. The expected time needed by the carbon beam to travel from the SC to the target has been subtracted from the ToF value to determine the particle velocity.

The mass measured in the spectrometer is given by the ToF and momentum measurements:

$$Mc^2 = \frac{pc}{\beta \cdot \gamma} \quad (4.2)$$

where γ is the Lorentz factor. The relative error on M is hence related to the time and momentum resolutions by the relation:

$$\frac{\Delta M}{M} = \sqrt{\left(\frac{\Delta p}{p}\right)^2 + \left(\gamma^2 \frac{\Delta t}{t}\right)^2} \quad (4.3)$$

where (4.1) and (4.2) have been used in the propagation of uncertainties formula. The differential cross sections are measured in FIRST as a function of the fragment production angle (θ) with respect to the beam axis, measured using the tracks reconstructed by the VTX detector, and of the particle kinetic energy normalized to the atomic mass A , defined as:

$$E_{\text{kin}} = \frac{1}{A} \left(\sqrt{p^2 c^2 + M^2 c^4} - M c^2 \right) \quad (4.4)$$

with mass number $A = M/m_N$, where m_N is the atomic mass unit. The advantage to express the cross sections in terms of this normalized kinetic energy, instead of total kinetic energy, is to cancel out the dependence on the mass of the different isotopes. In the following, “kinetic energy”, E_{kin} , will always stands for the normalized kinetic energy. All the reconstructed kinematic variables are corrected for the expected energy loss of the primary ^{12}C particle in the target. Since the depth of fragmentation point inside the target is not known, the correction is done assuming the mean energy loss in half of the target thickness.

4.1.2 Improving the Z_{ID} algorithm with VTX cluster size

From the previous paragraph follows that a wrong charge assignment due to the Z_{ID} algorithm from TW corresponds to a wrong momentum and mass assignment. An help to the charge identification can be provided by the VTX detector. The energy deposited by a ionizing particle impinging a M26 sensor produces charge carriers that are collected by a number of adjacent pixels: each particle produces then a cluster of fired adjacent pixels, with cluster size correlated to the energy and charge of the impinging particle. This property is used in FIRST to complement the charge measurement provided by the TW detector, described in § 3.1.5.

4.1. THE RECONSTRUCTION ALGORITHM

The mean cluster size distributions (on the different M26 sensors) for a selected sample of global tracks has been studied as a function of the Z_{ID} measured with the TW detector (see Fig. 4.2). In order to obtain a such pure sample global tracks coming from events with just one vertex, with more than one track and with only one track in the geometrical acceptance of ALADIN magnet, have been selected. The response of the VTX detector to the passage of an energetic particle and the corresponding cluster size distribution has been also simulated in the MC (see § 3.3). A fine tuning of the MC simulation of the cluster size is still necessary in order to improve the matching with the data distributions in Fig. 4.2. However such discrepancies produce an error in the cross section measurement much lower than the systematic uncertainties (see § 4.4) and so are not relevant for the final result.

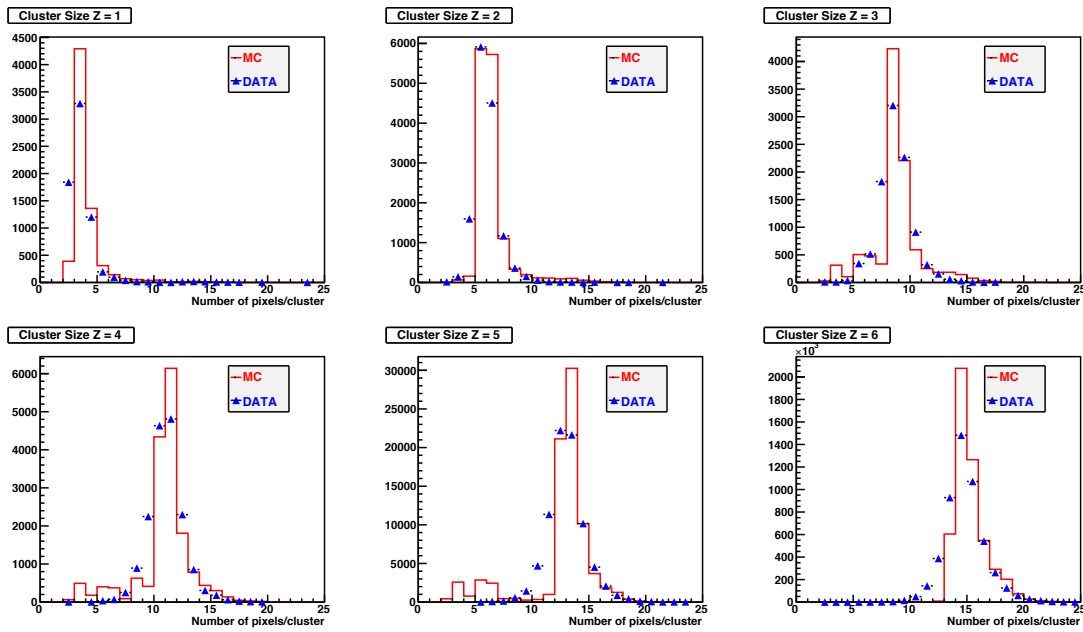


Figure 4.2: Data/MC cluster size distributions for the different fragment charge assigned from the TW Z_{ID} algorithm in a clean sample of global reconstructed tracks.

A VTX Z_{ID} algorithm has been calibrated on data, using the measured mean cluster size for each Z TW charge: the correlation between these two quantities is shown in Fig. 4.3. The mean values shown in Fig. 4.3 are the Most Probable values

(MPV) of Landau fits of the cluster size distributions for particle of different TW charges shown in Fig. 4.2. For each reconstructed track, the VTX Z_{ID} algorithm compares the mean cluster size with the calibrated distributions in order to assign a probability for each Z hypothesis. The hypothesis with the largest probability is then used to assign the Z_{ID} to the fragment.

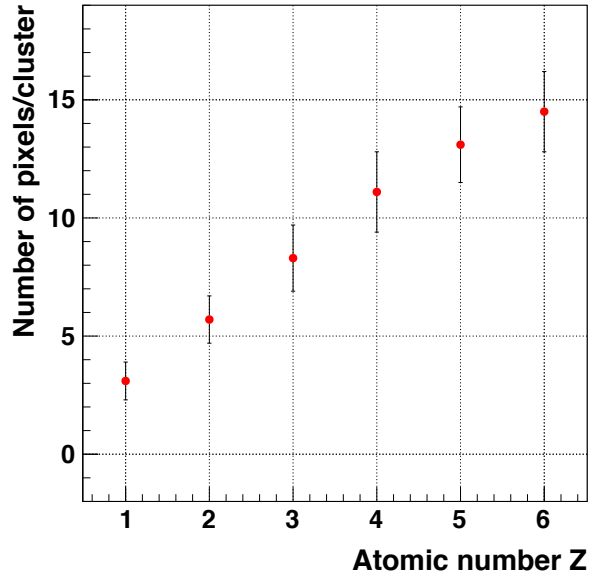


Figure 4.3: VTX tracks mean cluster size (number of pixels per cluster) as a function of the fragment atomic number Z obtained by the TW.

The charge from the VTX detector provides an additional information that can be useful in particular to distinguish hydrogen from helium. As shown in Fig. 4.3, a saturation effect of the cluster size produces a worse separation of ions with $Z > 3$.

4.1.3 Rating of the candidate tracks

The reconstruction algorithm produces the kinematic variables, for all the combinations of VTX tracks and TW hits, using only the information of the direction and production point of the VTX track and of the horizontal position of the TW hits,

4.1. THE RECONSTRUCTION ALGORITHM

together with the charge Z from the TW Z_{ID} algorithm. The measurements of the y coordinate in the TW and of the particle charge with the VTX are used to reduce the number of possible combinations and to perform a rating of the candidate tracks.

The selection of the final tracks from the list of global tracks candidates is based on a scoring function that uses the quality of the match between VTX tracks and TW hits to select the best candidates. The scoring function is based on the difference Δ_y between the y coordinate measured by the TW and the y coordinate of the VTX track (y_{VTX}) extrapolated to the TW plane, and on the difference Δ_Z between the charges measured with the TW Z_{ID} and the VTX Z_{ID} algorithms. The adopted scoring function $S(y, Z)$, used for the track rating, is:

$$S(y, Z) = \sqrt{\Delta_Z^2 \cdot W_Z^2 + \Delta_y^2 \cdot W_y^2} \quad (4.5)$$

where W_y and W_Z are two weighting factors. The weighting factors of (4.5) have been optimized using the full MC simulation and minimizing the fraction of wrong TW-VTX combinations.

The pairing procedure can produce wrong VTX/TW hits matches, forming a random combination that is selected by the scoring algorithm. Such fragments are defined as “combinatorial background”, since they represent the result of a reconstruction that artificially combines tracks and hits not belonging to a true fragment.

An example is shown in Fig. 4.4 for H and He fragments: the fraction of tracks in which the VTX track and the TW hits are not correctly paired with respect to the total number of reconstructed tracks (fraction of combinatorial background) is shown as a function of the charge weight W_Z , with W_y fixed at 1. The final W_Z value chosen for the fragments reconstruction is the one that minimize the fraction of combinatorial background (from Fig. 4.4 $W_Z = 8$ has been selected). A reduction of the fraction of wrong matches is visible for increasing values of W_Z , while at high values of W_Z the fraction of wrong matches for fragments of higher charges increases with W_Z . The values of the weights used in the scoring function ($W_Z = 8$ and $W_y = 1$) are a compromise between these two opposite trends.

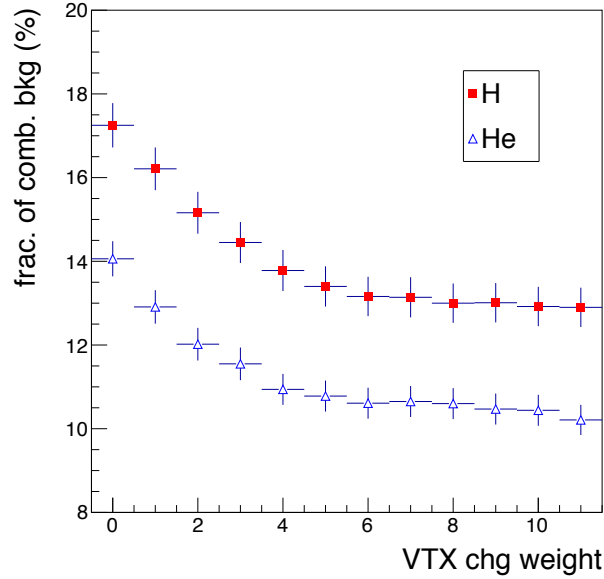


Figure 4.4: The fraction of tracks in which the VTX track and the TW hits are not correctly paired with respect to the total number of reconstructed tracks is shown as a function of W_Z . The chosen value of W_Z weight that minimize the wrong matches is 8.

4.1.4 TW hits clustering

Two neighboring TW hits in different planes are usually produced by the same particle. However, the reconstruction algorithm uses the combination of the VTX tracks with all the TW hits: two hits in different TW planes can thus be associated to two different tracks even if the two TW hits are compatible with the same particle. Duplicated tracks in which the same fragment has produced a hit in both front and rear TW wall have to be properly combined, according to geometrical and energetic criteria.

An algorithm has been developed to associate pairs of hits in the two TW planes into a single cluster. The TW clustering algorithm looks for pairs of TW hits in the two planes for which two global track candidate, paired with the same VTX track, have been reconstructed. If the parameters of the two global tracks are compatible

with only one fragment and if the distance between the two hits is smaller than a threshold ($\Delta_{\text{slat}} < 5$), the two hits are merged into a single one, with new values of the x, y coordinates and of the ToF. The charge assigned to the track is the larger of the two hits charges. The values of the geometrical cuts required for the matching have been optimized using the MC simulation, minimizing the probability of wrong VTX-TW matching.

4.2 Tracking algorithm performances

The tracking algorithm performances have been validated using the MC simulation. The output of the MC provides a list of particles, with all the information needed to reconstruct the history from the primary beam to the set of particles producing hits in the active parts of the detector. This list can be used to correlate each TW hit to a VTX track and to check if they are compatible to the trajectory of a single particle or if they are not correlated. A track reconstructed from a pair of uncorrelated VTX track and TW hit is considered a wrong match contributing to the combinatorial background. These mismatched tracks are the consequence of the large distance between VTX and TW detector (~ 6 m, without any other detector in the middle), of the poor spatial resolution along TW x coordinate and also of the limited resolutions of the variables used for the selection of valid tracks (y TW and particle charge Z). This situation is worsened in data respect to MC due to additional pile-up VTX tracks (mainly not interacting carbons).

Strong biases can be found when comparing reconstructed and generated kinematic variables (such momentum, mass and kinetic energy) for tracks with wrong combination of VTX tracks and TW hits. Let's consider the case of the kinetic energy. The difference between the generated ($E_{\text{kin,true}}$) and the reconstructed ($E_{\text{kin,rec}}$) values as a function of $E_{\text{kin,true}}$ is shown in Fig. 4.5 for hydrogen fragments, taking into account either wrong or right VTX-TW combinations. Selecting only tracks with right VTX-TW combinations the bias is negligible.

In the following, the reconstruction resolutions and efficiencies will be estimated

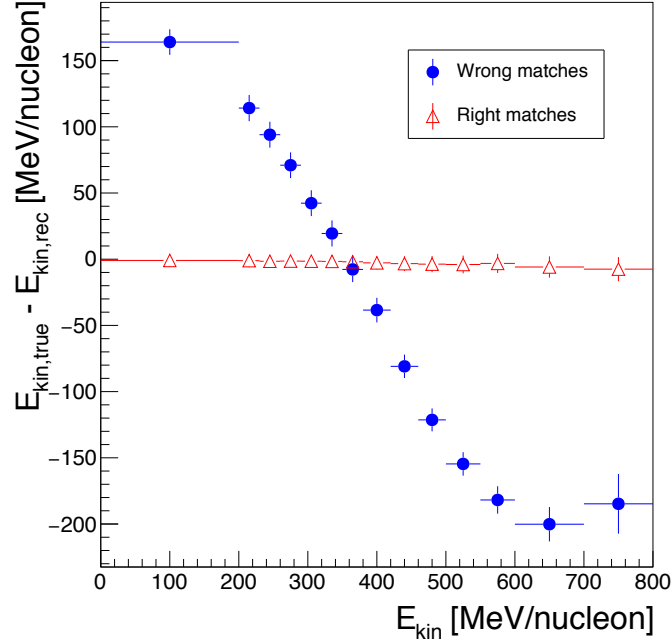


Figure 4.5: Reconstruction biases (mean difference between generated and reconstructed values) in E_{kin} for hydrogen fragments in the case of right and wrong VTX-TW matches.

using the correctly paired tracks, while the wrongly paired combinations are used to model the combinatorial background as discussed in § 4.3.1.

4.2.1 The angular and kinetic energy resolutions

The angular and kinetic energy resolutions have been measured in order to evaluate possible bias introduced by the reconstruction algorithm and to optimize the binning adopted for the cross section measurement. The widths of the bins in θ and E_{kin} used for the cross section measurement are chosen so as to minimize the migrations between different bins on the basis of the following resolution studies, trying to keep the bin width smaller or comparable with the measured resolutions.

The angular resolution σ_{θ} has been evaluated using global tracks from the full

4.2. TRACKING ALGORITHM PERFORMANCES

MC sample comparing the true fragment direction (θ_{true}) at the target exit point with the one reconstructed by the FIRST tracking algorithm (θ_{rec}). The distribution of $\theta_{\text{true}} - \theta_{\text{rec}}$ has been fitted with a Gaussian function in bins of θ_{true} and for each charge: the mean value has been used to estimate eventual bias, while the sigma value provides the resolution.

The angular resolution with respect to the track emission angle, for fragments and carbon ions is shown in Fig. 4.6. For all particles we obtain $\sigma_{\theta} \sim 0.054^{\circ}$, except for protons ($\sigma_{\theta} \sim 0.076^{\circ}$). Such numbers are entirely dominated by the intrinsic resolution of the VTX detector.

These figures refer to the tracking resolution only. Aiming to the estimation of the accuracy on the determination of the track production direction, the multiple scattering induced by the path of the fragment inside the target must be taken into account.

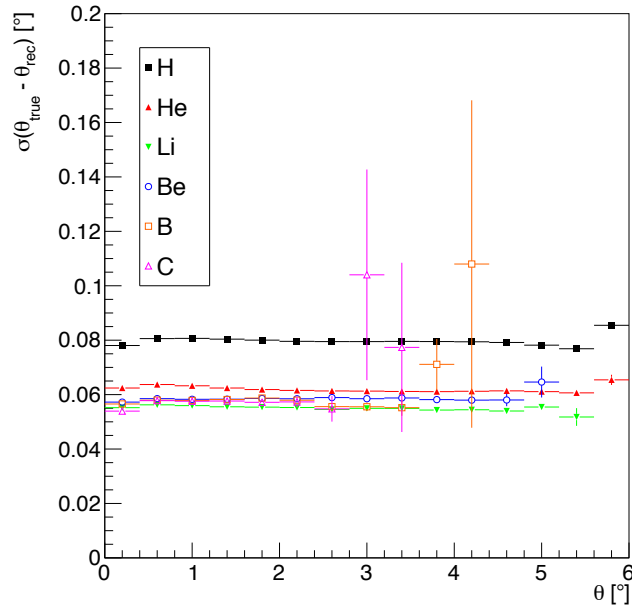


Figure 4.6: Angular resolution as a function of the fragment polar angle.

Thus comparing the reconstructed fragment direction with the production value,

inside the target, the resolution is instead in the 0.1° - 0.15° range, completely dominated by the multiple scattering and with a dependence on the fragment charge and energy. Must be remarked that angular resolution is dominated by VTX information, so it doesn't depend on the tracking algorithm.

The kinetic energy resolution ($\sigma_{E_{\text{kin}}}$) has been evaluated within the full MC simulation comparing the reconstructed energies with the corresponding true values at generator level, as for the angular resolution. Fig. 4.7 shows the E_{kin} resolution as a function of the measured kinetic energy. A rise of $\sigma_{E_{\text{kin}}}$ with respect to E_{kin} is observed for all fragments, as expected for a particle propagating in a magnetic field ($\sigma_p/p \propto p$).

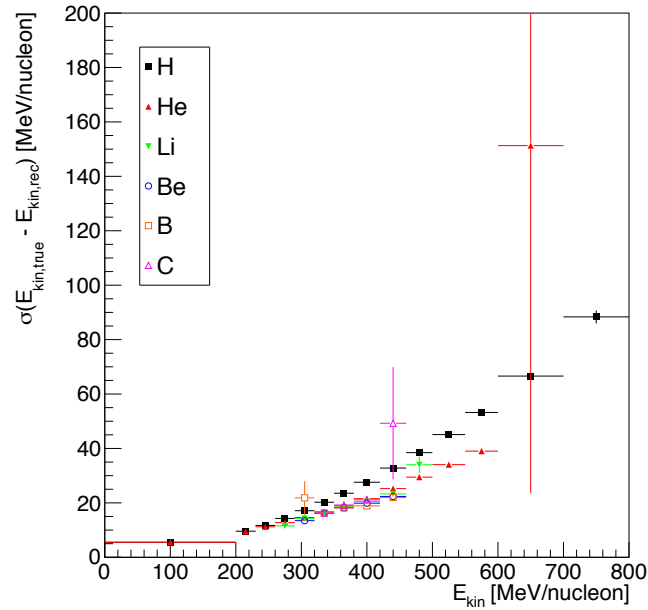


Figure 4.7: E_{kin} resolution for fragments with different Z_{ID} , from a global track MC sample selected requiring only correctly paired VTX tracks and TW hits.

4.2.2 The tracking efficiencies

The tracking efficiencies measured as a function of θ and E_{kin} are main ingredients to extract the differential cross sections as defined in next paragraph § 4.3 in equations (4.7) and (4.8). In order to evaluate the tracking efficiency for each isotope coming from ^{12}C fragmentation, a dedicated MC simulation has been developed. A sample of 10 million events for each isotope has been generated with FLUKA, producing fragments from the center of the target, with a flat E_{kin} spectrum in the range 0–800 MeV/nucleon, within the angular acceptance of the magnet. In this way a full θ , E_{kin} phase space coverage is obtained. The tracking efficiencies have been evaluated using such MC simulation sample, selecting only correct VTX-TW matches. For each fragment charge, the efficiency is defined as the ratio between the number of reconstructed tracks (n_{REC}) and the number of MC generated tracks (n_{PROD}) emerging from the target in the magnet angular acceptance:

$$\varepsilon_{\text{trk}} = \frac{n_{\text{REC}}}{n_{\text{PROD}}} \quad (4.6)$$

The tracking algorithm is then efficient when a reconstructed global track is build using the correct TW hit and VTX hit, i.e. belonging to the MC track under study. The efficiency as a function of the measured angle θ and kinetic energy E_{kin} , is shown in Fig. 4.8 for each isotope. The uncertainties shown are statistical only. The drop observed in the angular efficiency (Fig. 4.8, left) around 5° is due to the geometrical acceptance of the ALADIN magnet entrance window, while the rise observed in the first kinetic energy bin (Fig. 4.8, right) is given by a threshold effect.

4.2.3 Kinetic energy distribution unfolding

The E_{kin} resolution studies discussed in § 4.2.1 and presented in Fig. 4.7, showed that the relative kinetic energy resolution worsen, as expected, with the fragment kinetic energy. In order to correct the measured energy for this resolution effect, that broaden the kinetic energy distribution, and to obtain the true production kinetic energy of the fragment, we're developing an unfolding procedure using the TUnfold package of ROOT [120].

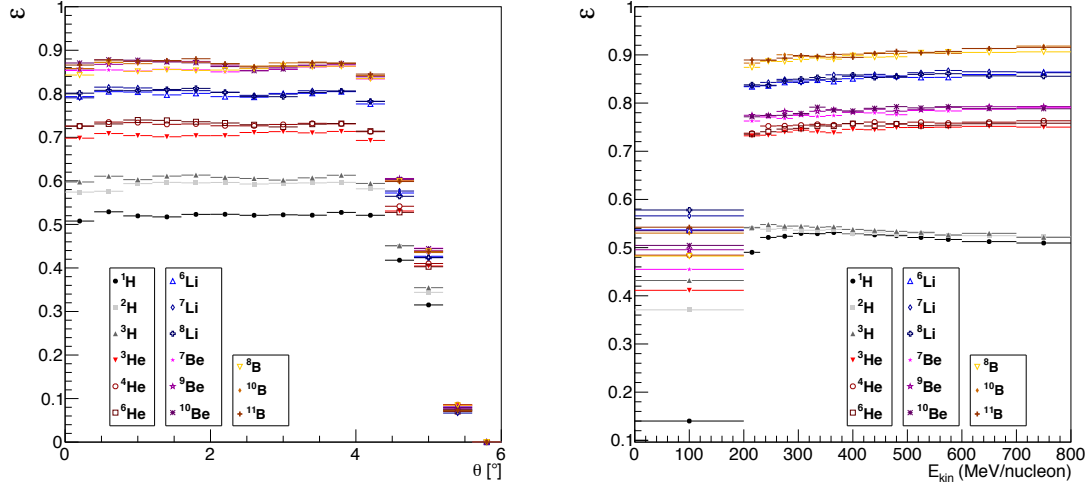


Figure 4.8: Tracking efficiency (ε_{trk}) for the identified isotopes as a function of fragment measured angle θ (left) and of the kinetic energy E_{kin} (right).

In particular, it is important to apply the tracking efficiency correction to the measured fragment yields with respect to the true E_{kin} of the fragment (see next paragraph § 4.3, equations 4.7 and 4.8), since these corrections are determined as a function of the true production energy. The dedicated MC simulation has been used for this purpose. Using this MC simulation it is possible to build the 2-dimensional unfolding matrix that contains the information needed to correlate the reconstructed kinetic energy with the true E_{kin} . The details on the unfolding algorithm are given elsewhere [120].

For what concerns this thesis, the cross sections measured as a function of the fragment E_{kin} , shown in § 4.3.4, have not yet been unfolded to take into account the detector resolutions.

4.3 Cross section measurements

The differential fragmentation cross sections, with respect to the normalized kinetic energy E_{kin} and to the angle with respect to the beam axis (θ), for the production of the i -th isotope A_ZX , with atomic number Z and mass number A , are defined as:

$$\frac{d\sigma_i}{d\Omega}(\theta) = \frac{Y_i(\theta)}{N_C \times N_{TG} \times \Delta\Omega \times \epsilon_{trk}^i(\theta)} \quad (4.7)$$

$$\frac{d\sigma_i}{dE_{kin}}(E_{kin}) = \frac{Y_i(E_{kin})}{N_C \times N_{TG} \times \Delta E_{kin} \times \epsilon_{trk}^i(E_{kin})} \quad (4.8)$$

where Y_i is the number of reconstructed fragments for the i -th isotope in an angular or energy bin $\Delta\Omega$ or ΔE_{kin} respectively. N_{TG} is the number of particles in the target per unit surface, N_C is the number of ${}^{12}\text{C}$ ions impinging on the target and ϵ_{trk}^i is the tracking reconstruction efficiency for the i -th isotope (defined in § 4.2.2).

The number of target particles per unit surface is given by $N_{TG} = (\rho \times d \times N_a)/A$ where ρ and d are the target density and thickness respectively (see table 4.2, where $X_{TG} = \rho \times d$), while N_a and A are the Avogadro number and the target atomic mass respectively.

The bin widths used for the cross section measurements have been chosen in order to limit the migrations between the different bins.

The number of ${}^{12}\text{C}$ ions impinging on the target (N_C) is measured by the SC detector (see § 3.1.1). The occurrence of multiple ${}^{12}\text{C}$ ions in a single event has been measured and found negligible in the data sample: for each trigger a single ${}^{12}\text{C}$ ion crossing is counted with negligible exceptions, due to the low trigger rate.

The production abundance of each fragment (Y_i), as well as the identification of different isotopes for each charge hypothesis is measured using the reconstructed mass spectra. In order to compute properly the fragment yields Y_i the background has to be taken into account and subtracted. Two different components can be identified in the background mass spectra:

1. Combinatorial background coming from the matching of wrong VTX tracks

and TW hits combinations or from the matching between background hits and/or fake tracks, as described in § 4.1.3;

2. A component coming from right VTX track and TW hits combination, for which the Z_{ID} algorithm assigns a wrong charge Z (see § 3.1.5). In the following we will refer to this source of background as “cross feed background”.

In order to extract the fragment yield for each isotope A_ZX , the reconstructed mass spectra are fitted, for each charge Z and for each angular and energy bin, taking into account a contribution from the signal and a contribution from the background. The fragment yields are then called raw yields (Y_i^{raw}) because they have to be corrected yet for cross feed corrections, so as to obtain the final Y_i .

4.3.1 Combinatorial background evaluation

The combinatorial background has to be taken into account and subtracted from the reconstructed track sample. In order to model the background the mass spectra coming from combinatorial background have been evaluated using the full MC simulation, for each charge and for each angular and kinetic energy bin. Fig. 4.9 shows, for the full MC sample, the mass spectra in two different kinetic energy bins (200-230 MeV/nucleon and 350-380 MeV/nucleon) for lithium candidates selected requiring that the VTX tracks and the TW hits used to build the track belong to two different particles (i.e. built using wrong hits assignment).

In Fig. 4.9, the probability density function (PDF) used to model the combinatorial background is shown, as a blue curve, superimposed to the reconstructed mass spectra (black dots). The PDF is built from the MC spectra using the one dimensional kernel estimation method [121] provided by the RooFit package [122]. In our analysis we take the shape of the combinatorial background directly from the full MC simulation and then we’ll fit its normalization directly on data, using the mass distributions (see § 4.3.2).

The systematic uncertainty correlated to the uncertainties on the combinatorial background, that affects the cross section measurement, is discussed in § 4.4.

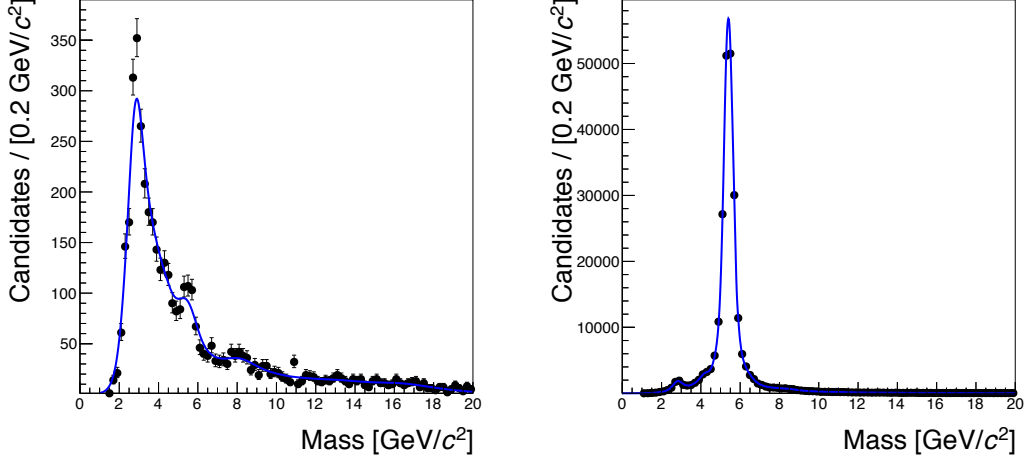


Figure 4.9: Mass distribution for two different kinetic energy bins, 200-230 MeV/nucleon (left) and 350-380 MeV/nucleon (right), for reconstructed Li fragment candidates in the full MC sample.

4.3.2 Fragment yield measurement

The fragment yields Y_i^{raw} are measured fitting the reconstructed mass spectra for each charge and angular (energy) bin, using an unbinned extended maximum likelihood approach (performed using the RooFit toolkit [122]), in which the signal and background yields are fitted together: the signal is modeled with a Gaussian PDF for each isotope and the background PDFs, accounting for the combinatorial background, are extracted from the MC simulation (see § 4.3.1).

An example of mass fits, for fragments of different charges and for reconstructed mass spectra in different E_{kin} and θ bins, is shown in Fig. 4.10. Superimposed to the data distribution (black dots), the total PDF is shown (in red) while the signal PDF, modeling the various isotopes, is shown in blue. A magenta dotted line shows the contribution from the combinatorial background. The top row shows the invariant mass fits to the H fragment spectra in a given bin of angle (left) and energy (right): protons, deuterons and tritons isotopes are clearly visible. The bottom row shows the same information for Li fragments in different angle (left) and energy (right)

bins: the two visible peaks correspond to ${}^6\text{Li}$ and ${}^7\text{Li}$ isotopes; less visible is the ${}^8\text{Li}$ isotope.

The obtained Y_i^{raw} yields from the fit have to be corrected yet for the cross feed contamination (see next paragraph § 4.3.3).

4.3.3 Cross feed evaluation

In spite of the Z_{ID} algorithm, described in § 3.1.5, some fragments, properly matched, are identified with a wrong charge, biasing the final cross section measurement. In order to correct for the cross feed between reconstructed fragments, a method based on the full MC information has been developed. The effect due to the wrong Z_{ID} assignment is shown in Fig. 4.11, where the reconstructed mass spectrum is shown for fragments in which the reconstructed charge Z is equal to three, in the angular bin with $1.2^\circ < \theta < 1.6^\circ$. The total spectrum is shown in black (solid line). The contribution from the combinatorial background (see § 4.3.1) is shown in red full squares, while the main signal contributions to the spectrum, respectively from ${}^6\text{Li}$, ${}^7\text{Li}$ and ${}^8\text{Li}$ are shown as open marks (circle, square and triangle respectively). A clear contamination from ${}^4\text{He}$ appears (in blue full triangles), under the ${}^6\text{Li}$ peak: such contamination cannot be distinguished by the mass fit and hence has to be subtracted from the obtained yields of fragments (Y_i^{raw} in § 4.3.2). In the following we'll refer to isotopes like ${}^6\text{Li}$ in the example of Fig. 4.11 as “contaminated” isotopes, while to isotopes like ${}^4\text{He}$ as “contaminant” isotopes.

The cross feed background has to be subtracted from the signal yield Y_i^{raw} to take into account contamination by isotopes with a wrong charge identification. The yields Y_i^{raw} are computed only in a given range of mass distribution, so the cross feed contamination has to be considered only if there are contaminants peaks in that range. In the example of Fig. 4.11, the ${}^3\text{He}$ contamination has not to be considered because is outside the mass fit range. Few isotopes contribute to the cross feed background, usually a maximum of two contaminants isotopes in a given fit range have to be considered, and usually just one contaminant isotope is under a given mass peak.

4.3. CROSS SECTION MEASUREMENTS

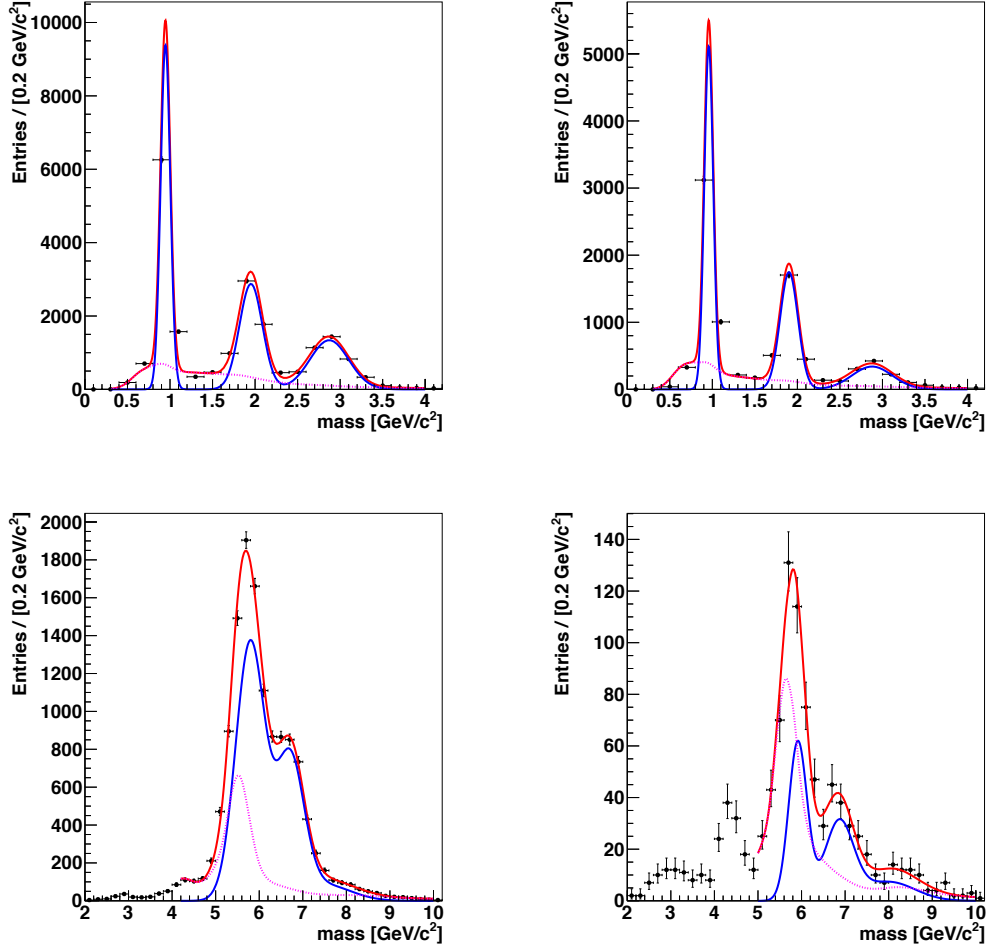


Figure 4.10: Mass fit results for H and Li fragments mass spectra in different E_{kin} , θ bins. The top panel shows the invariant mass fits for H fragments with polar angles between 0.4° and 0.8° (left), and with E_{kin} in the range between 200 MeV/nucleon and 230 MeV/nucleon (right). The bottom panel shows the invariant mass fits for Li fragments with polar angles between 1.2° and 1.6° (left) and with E_{kin} in the range between 260 MeV/nucleon and 290 MeV/nucleon (right).

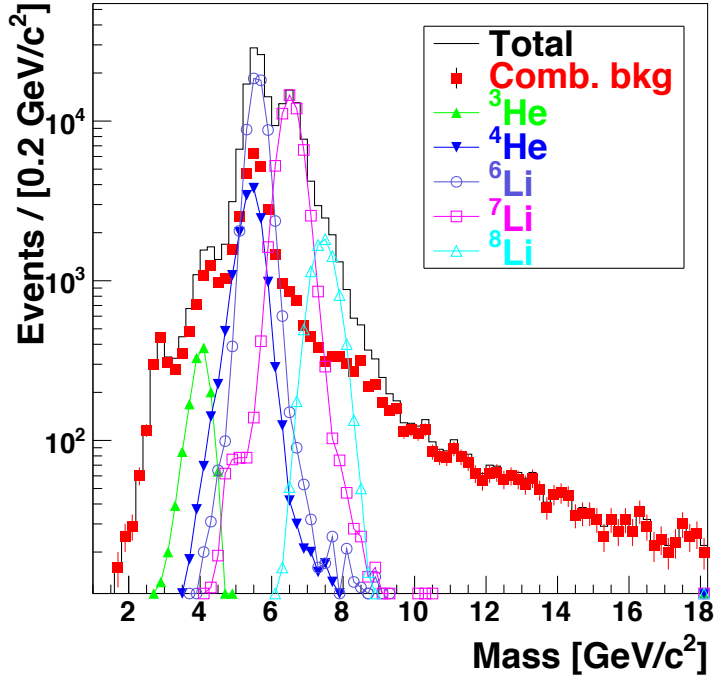


Figure 4.11: Reconstructed mass spectrum for Li fragments using the full MC simulation sample. The black spectra is the total reconstructed spectrum. The red full squares are showing the combinatorial background contamination. The main signal contributions to the spectrum, respectively from ${}^6\text{Li}$, ${}^7\text{Li}$ and ${}^8\text{Li}$ are shown as open marks (circle, square and triangle respectively). The cross feed background from ${}^3\text{He}$ and ${}^4\text{He}$ is shown in full triangles (green and blue, respectively).

In order to compute the correction factors ε_i^{xf} , that have to be applied to the Y_i^{raw} yields for each isotope, the full MC sample has been analyzed, in bins of reconstructed angle and kinetic energy and the contaminations relative to the analyzed isotopes have been computed. If A is a contaminated isotope and B is its contaminant, being Y_A and Y_B their corresponding yields, the cross feed correction to be applied to the Y_i^{raw} yields, obtained from mass fit, is:

$$Y_i = \frac{Y_A}{Y_A + Y_B} \times Y_i^{raw} = \varepsilon_i^{xf} \times Y_i^{raw} \quad (4.9)$$

4.3. CROSS SECTION MEASUREMENTS

While the absolute amount of a given contamination under a certain reconstructed peak depends clearly on the absolute fragmentation cross section implemented in the MC, the cross feed contamination is a relative correction that depends on the capability of the MC simulation to reproduce the ratio between the contaminant and contaminated isotopes cross sections. The obtained ε_i^{xf} factors have been corrected in order to take into account the different cross sections ratio between data and MC: the change in each isotope total cross section measured without any correction has been used to assign a systematic uncertainty (see § 4.4).

The maximum cross feed correction ($\sim 15\%$) are applied to the ${}^6\text{Li}$ and ${}^8\text{B}$ isotopes that are contaminated by the ${}^4\text{He}$ and ${}^7\text{Be}$ isotopes respectively.

4.3.4 Cross sections results

The isotopic differential cross sections have been obtained for each fragment produced in the interaction of the beam with both targets, measured with the FIRST apparatus. The isotopes identified with mass fits are reported in the table 4.1.

charge	isotope ${}^A\text{X}$
$Z = 1$	${}^1\text{H}, {}^2\text{H}, {}^3\text{H}$
$Z = 2$	${}^3\text{He}, {}^4\text{He}, {}^6\text{He}$
$Z = 3$	${}^6\text{Li}, {}^7\text{Li}, {}^8\text{Li}$
$Z = 4$	${}^7\text{Be}, {}^9\text{Be}, {}^{10}\text{Be}$
$Z = 5$	${}^8\text{B}, {}^{10}\text{B}, {}^{11}\text{B}$

Table 4.1: Isotopes identified with mass fits.

As an example, in Fig. 4.12 the production cross sections of the isotopes ${}^1\text{H}$, ${}^2\text{H}$ and ${}^3\text{H}$ in the interaction of the ${}^{12}\text{C}$ beam with the gold target are shown as a function of θ and E_{kin} . The results for the three isotopes ${}^1\text{H}$, ${}^2\text{H}$ and ${}^3\text{H}$ are shown respectively in red, green and blue, together with their sum, in black squares, corresponding to the overall contribution of hydrogen fragments. The uncertainty shown in the

plots account for statistic and systematic contributions, evaluated as described in § 4.4. The $d\sigma/dE_{\text{kin}}$ results are shown for fragments in the ALADIN acceptance ($\lesssim 6^\circ$): such cross sections shown the expected peak at about 400 MeV/nucleon, that corresponds to the energy of the primary beam. The isotopic cross sections for all the produced isotopes as a function of θ and E_{kin} , for both the gold and the composite targets are shown in the Appendix A. Also a full set of tables for all the measured isotopic cross sections is provided in the Appendix A.

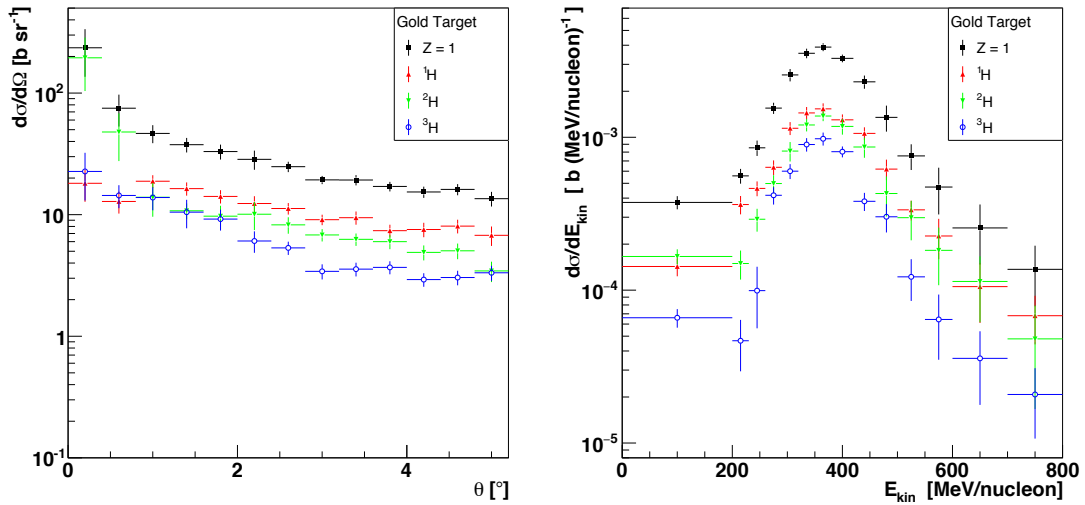


Figure 4.12: Differential cross sections for the production of the isotopes ^1H , ^2H and ^3H in the interaction of the ^{12}C beam with the gold target, as a function of the production angle of the fragment respect to the beam axis (left) and of the production normalized kinetic energy of the fragment (right). The cross sections have been computed using Eq. 4.7 and Eq. 4.8 for fragments within the ALADIN angular acceptance ($\lesssim 6^\circ$). The results for each isotope are shown separately, together with their sum (in black squares). The total uncertainty (statistic and systematic added in quadrature) is shown.

The measured elemental differential cross sections for the gold target, as a function of θ and E_{kin} , are shown respectively in Figs. 4.13 and 4.14, while the ones for the composite target, as a function of θ and E_{kin} , are shown respectively in Figs. 4.15

4.3. CROSS SECTION MEASUREMENTS

and 4.16. As in the isotopic cross section, the reported uncertainties account also for the systematic contribution, and the $d\sigma/E_{\text{kin}}$ results are referred to the ALADIN geometrical acceptance.

The histograms for each atomic number have been obtained by summing up all the non negligible contributions from different isotopes that have the same Z_{ID} .

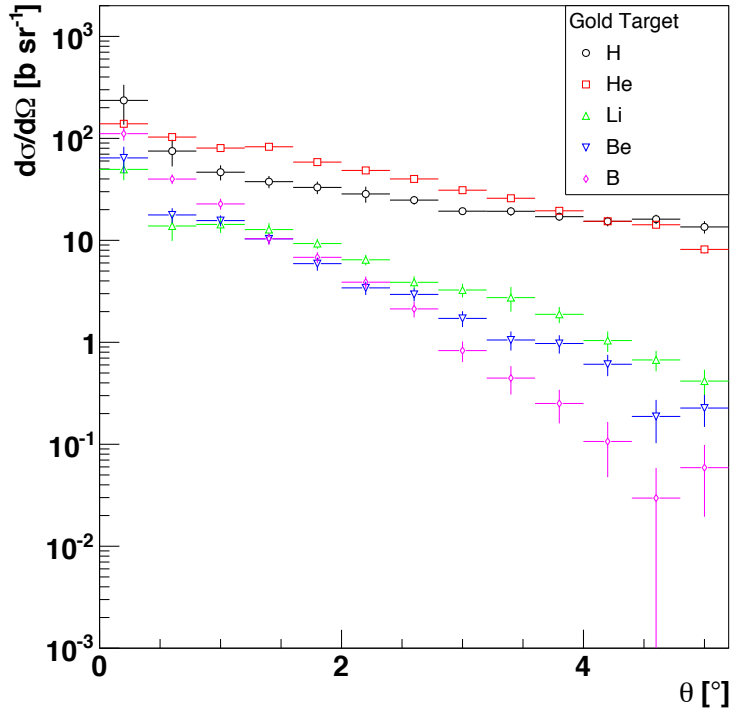


Figure 4.13: Elemental differential cross sections for the gold target, as a function of the fragment angle with respect to the beam axis, measured using Eq. 4.7. The total uncertainty (statistic and systematic) is shown: for most of the points is well below the marker size.

The total charge-changing cross section σ_{tcc} can be calculated measuring the number of final carbons N_f impinging on the TW and the number of initial carbons N_0 impinging on the Start Counter. In order to take into account the secondary fragmentation in the detector and in the air [82] the number of final carbons has to be corrected using the data from the run without target.

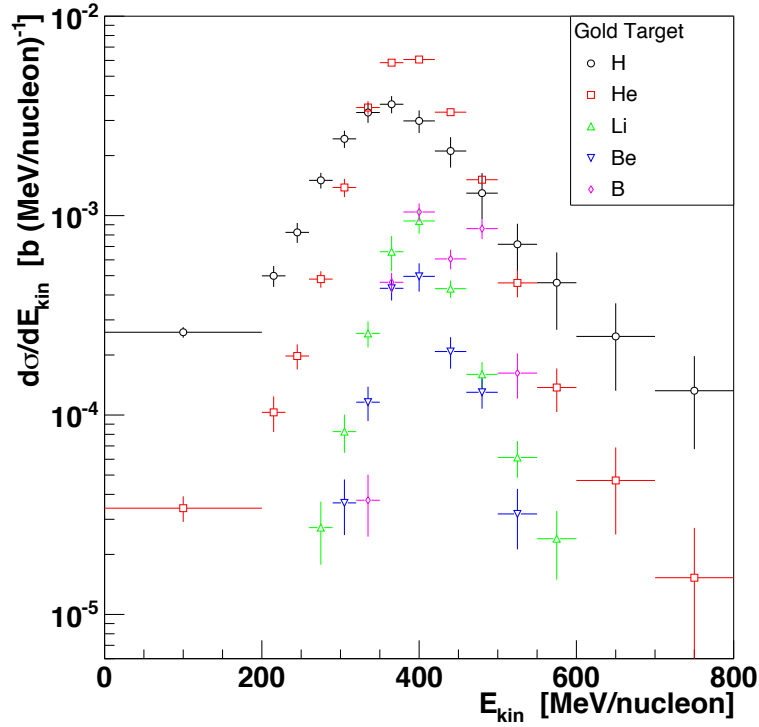


Figure 4.14: Elemental differential cross sections for the gold target, as a function of the fragment normalized kinetic energy, measured using Eq. 4.8 for fragments within the ALADIN angular acceptance ($\lesssim 6^\circ$). The total uncertainty (statistic and systematic) is shown.

For the target runs (TG):

$$N_f^{TG} = N_0^{TG} \exp(-X_{TG}/\lambda_{TG}) \exp(-X_{det}/\lambda_{det}) \quad (4.10)$$

where $X_{TG} = \rho \times d$ is the target thickness and λ_{TG} is the interaction mean free path (MFP) in the target, while X_{det} and λ_{det} are the same quantities for detector + air.

For the no-target runs (NT):

$$N_f^{NT} = N_0^{NT} \exp(-X_{det}/\lambda_{det}) \quad (4.11)$$

From the ratio of (4.10) and (4.11) is possible to obtain the MFP:

$$\lambda_{TG} = X_{TG} / \ln \left[\frac{N_f^{NT}/N_0^{NT}}{N_f^{TG}/N_0^{TG}} \right] \quad (4.12)$$

4.3. CROSS SECTION MEASUREMENTS

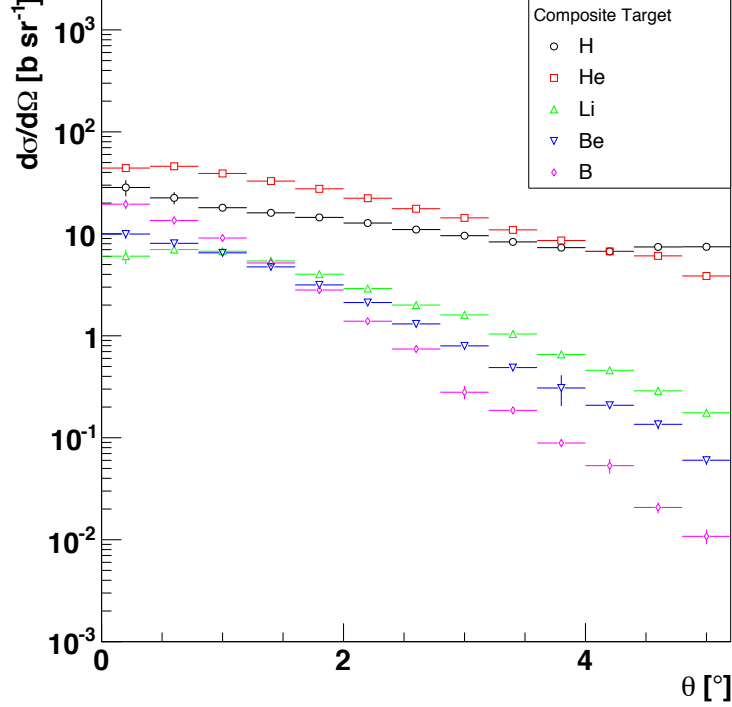


Figure 4.15: Elemental differential cross sections for the composite target, as a function of the fragment angle with respect to the beam axis, measured using Eq. 4.7. The total uncertainty (statistic and systematic) is shown: for most of the points is well below the marker size.

From (4.12) is possible to obtain the σ_{tcc} cross section (in cm^2) as:

$$\sigma_{tcc} = \frac{A}{N_A \times \lambda_{TG}} \quad (4.13)$$

where A is the average mass number of the target and N_A is the Avogadro's number.

In order to count the number of final carbons in the runs with and without target N_f^{TG} and N_f^{NT} , the number of reconstructed carbons requiring 1 vertex and 1 track in the VTX detector have been selected. The reconstruction efficiency corresponding to this selection of carbon events has been considered the same, for no target and TG runs and then cancel out from the σ_{tcc} measurement. The measured σ_{tcc} cross section for both FIRST targets are reported in table 4.2 with the corresponding

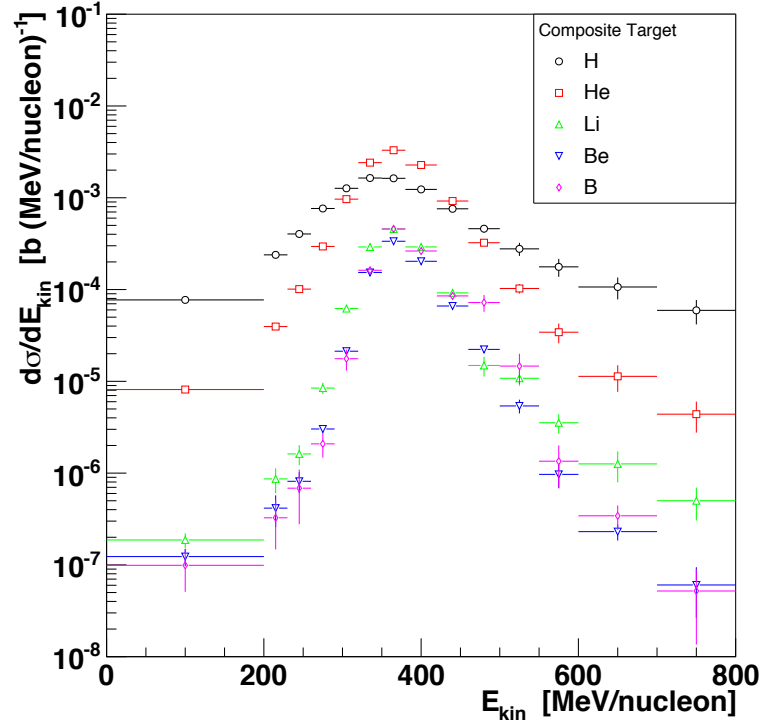


Figure 4.16: Elemental differential cross sections for the composite target, as a function of the fragment normalized kinetic energy, measured using Eq. 4.8 for fragments within the ALADIN angular acceptance ($\lesssim 6^\circ$). The total uncertainty (statistic and systematic) is shown.

statistical errors:

target	X_{TG} (g/cm ²)	λ_{TG} (g/cm ²)	A (g/mol)	σ_{tcc} (barn)
gold	0.965	6.469	196.97	50.55 ± 0.17
composite	3.43	25.57	27.068	1.758 ± 0.006

Table 4.2: Total charge changing cross sections.

4.4 Systematic uncertainties

The method used to evaluate the systematic uncertainties in the cross section measurement was to repeat several times the analysis procedure, changing the reconstruction algorithms (local and global), the calibration and geometrical parameters, the corrections and the background subtraction procedure. The cross sections values obtained in this way have been compared with the one obtained following the prescriptions and the strategies outlined in the previous sections, to which we will refer as the *default* result. The systematic uncertainty relative to each measurement has been assigned computing the spread of the different results (RMS) with respect to the default one, for each angular/energy bin. In the plots showing the isotopic cross sections in Fig. 4.12 and in Appendix and in the ones showing the elemental cross sections in Fig. 4.13, 4.14, 4.15 and 4.16, the systematic uncertainty has been added in quadrature to the statistical uncertainty.

Several checks of our analysis have been performed to evaluate such a systematic. We studied the stability of the measurement with respect to changes of global or local algorithms, such as the track selection criteria, the scoring function and the TW hit clustering, or such as the VTX detector tracking algorithm and TW hit efficiency. These checks evaluate the influence on the cross sections results of possible discrepancies between the actual detector response and what has been implemented in the MC simulation. For each systematic study the full reconstruction and analysis procedure has been repeated applying the same changes to both data and MC. Also for the estimation of combinatorial background and reconstruction efficiencies has been repeated applying in the MC the same changes applied in the data reconstruction. A MC sample of 50 million events has been produced for each of these checks.

Other systematic checks concerned the detector description and alignment: global positioning of detectors has been varied within the precision achieved by the survey. The reconstruction has been repeated by changing the corresponding parameters only in the data, and using the nominal sample of MC events to evaluate backgrounds, acceptances and efficiencies. The last set of systematic checks were

focused on the background subtraction, both on PDF modelization of the combinatorial background and on cross feed correction.

An important source of uncertainties come from the modeling of the TW detector efficiency for particles releasing little energy, namely hydrogen isotopes of high kinetic energy. In the TW detector, designed to have a wide dynamic range to detect heavy Z fragments, the hydrogen isotopes signals are close to the minimum threshold needed to have a signal in the CFDs. As reported in § 3.1.5 in order to improve the tracking efficiency for low charge fragments, also the events in which only one TDC gives a signal have been used. The limited knowledge of the TW energy thresholds has been evaluated repeating the analysis by using only events where both TDCs and ADCs measurements were available. The change with respect to the *default* gives an evaluation of the robustness of the MC simulation of energy thresholds and relative hit reconstruction efficiency. The difference observed is, as expected, significant only for hydrogen isotopes and is shown in Fig. 4.17 as red full topside down triangles (*SCC*).

The impact of the global reconstruction algorithm procedure (namely matching of TW and VTX candidates and rating of the tracks) is evaluated in the *Cls/Sco*, *ClusOnly* and *ScorInv* study, shown in Fig. 4.17. The analysis has been redone changing both the scoring function, using different W_Z and W_y weights, and disabling the TW hits clustering algorithm, in order to account for sub-optimal optimization of the weights and of the clustering algorithm. This study is sensitive to tracking algorithm sub-optimal tuning and to different combinatorial background conditions.

A set of systematic studies concerning the vertex reconstruction has also been performed: the matching with the BM has been tested in the *BM mat* study, that analyzed the effect of a more stringent cut on the BM tracking, while the effect of the use of BM predicting the carbon impinging point on the target, within the VTX tracking (BM point is used as seed for VTX track reconstruction) is tested in the *VTX trk* study. In this analysis the L0 tracks reconstruction in the VTX has been redone using a fully standalone procedure [107], that is not relying on the BM.

The systematic uncertainty due to the limited precision of the TW position, with

4.4. SYSTEMATIC UNCERTAINTIES

respect to the general FIRST reference frame, was studied by changing the absolute horizontal position of the TW of ± 1 cm, corresponding to the resolution of the survey performed after the data taking. The changes in the vertical and Z position are expected to give small effects on the results with respect to the uncertainties in the horizontal position, so their effect has not been evaluated in this study. The results of this study is shown in Fig. 4.17, labeled as *TW pos+(-)*.

The systematic affecting the fit of the reconstructed mass distributions has been evaluated repeating the fit after changing the combinatorial mass model PDF. The observed result is, for most bins, well within the statistical uncertainty, as shown in Fig. 4.17 (spectrum labeled *Bkg model*). It has also to be noted that the different analyses strategies used for the evaluation of the systematic uncertainty explored several combinatorial background conditions (modified shapes and different background contamination): the final systematic uncertainty therefore covers also the background contamination subtraction in different background conditions.

Finally the systematic checks included also the evaluation of the effect of the estimation of the cross feed correction that is used to correct the Y^{raw} yields described in § 4.3.3. The data/MC rescaling used for the evaluation of the correction factors has been switched off in order to evaluate the maximum impact of this rescaling. This last systematic check is shown in Fig. 4.17 and is labeled *Xfeed sys*.

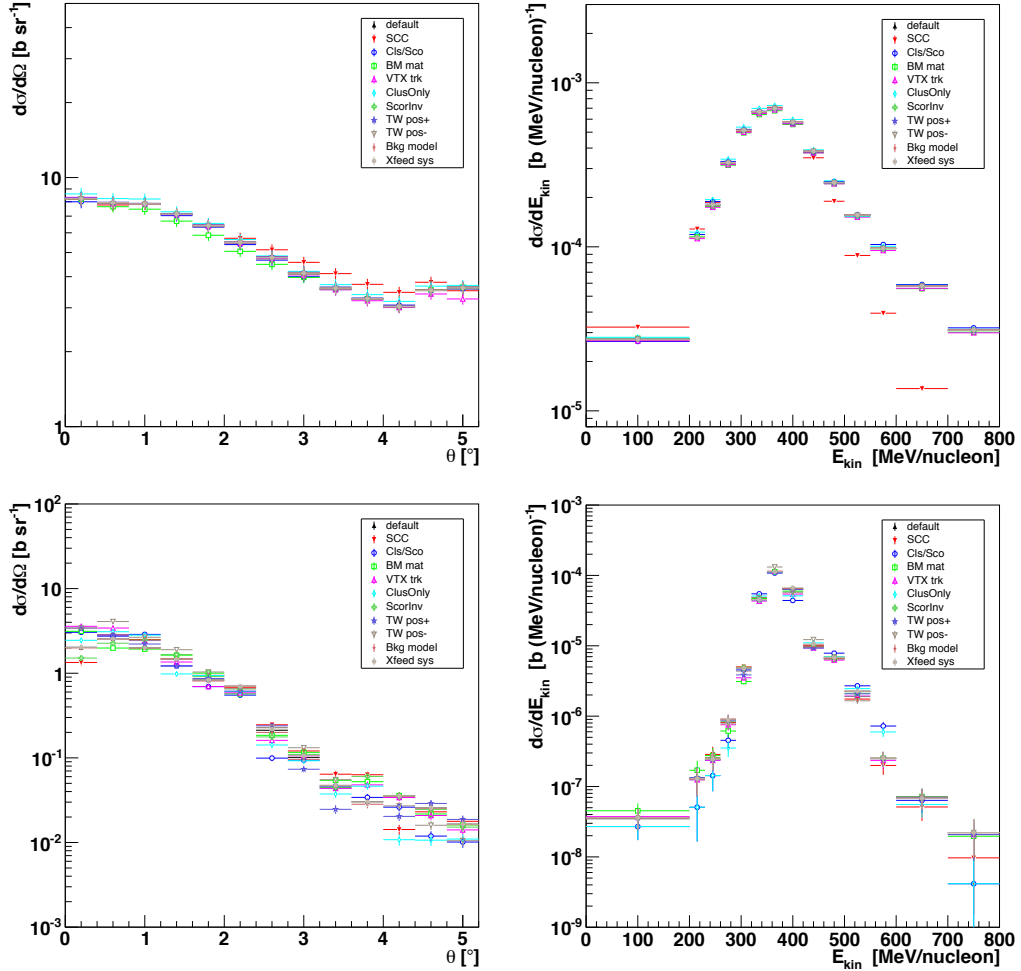


Figure 4.17: Effect of systematic checks on the production angular and energy cross sections of ${}^1\text{H}$ (top) and ${}^9\text{Be}$ (bottom) fragments, for the composite target. The production cross sections obtained changing the analysis strategy, algorithm and cuts are shown. The details on the different spectra labels are described in the text.

4.4. SYSTEMATIC UNCERTAINTIES

Chapter 5

A possible upgrade for the FIRST detector

A simple and straightforward improvement of the FIRST experiment would be the introduction of an independent tracking detector between the ALADIN magnet and the TW detector. The large volume time projection chamber (TPC-MUSIC IV [111]), should have provided the measures of track directions and energy releases in this region, but could not be operated during the data taking. This failure made the TW the most critical detector for the analysis. The alignment and calibration procedure has become then critical and most of the studies described in the previous chapters (such as TW quantities resolutions and the Z_{ID} algorithm) were based only on the comparison of the relative response of the two planes of the TW (see § 3.1.5). For these reasons the uncertainties in the calibration and alignment parameters produced not negligible systematic errors for the measurement (see § 4.4).

In this experimental setup the momentum and mass resolutions are dominated by the accuracy on the horizontal position (x coordinate) measurement in the TW, limited by the slat width of 2.5 cm (being the spatial resolution of the VTX detector $\sigma_x < 10 \mu\text{m}$). Actually the momentum resolution σ_p for particles detected after the bending in a magnetic field is proportional to the spatial resolution along the x

coordinate σ_x of the tracking detectors (VTX and TW):

$$\frac{\sigma_p}{p} \propto \frac{\sigma_x \cdot p}{h \cdot L \cdot B} \quad (5.1)$$

where p is the particle momentum, h is the distance between the magnet and the hodoscope, L is the length of the magnetic region crossed by the particle and B is the magnetic field intensity. So, fixed h , L and B , the momentum resolution worsens with poor spatial resolution along the x coordinate and with high particle momenta. This stands in particular for fragments with high charge produced with a velocity close to the velocity of the impinging particle, with a limited range of kinetic energies and production angles, and with low bending in the magnetic field (see FIRST kinetic energy resolution in § 4.2.1, Fig. 4.7). A direct consequence of these considerations is that uncertainties in the track positions determination are the main source of uncertainties on the measured cross sections (see § 4.4). Multiple Coulomb Scattering in air, in the target and in the detectors crossed by the particles also affects the total momentum resolution, but the contribution is small and has been neglected in equation (5.1)

Following equation (4.3), also mass resolution worsens with poor spatial resolution of the tracking detectors downstream the magnet and with high particle momenta. As a consequence a poor mass resolution produces a worse isotope separation and larger uncertainties in isotopic cross sections. The worsening of the mass resolution with respect to the particle momentum, and then with particle mass, is clearly shown in Fig.4.10 in § 4.3.2, where the better mass separation in hydrogen isotopes (top) is evident respect to lithium isotopes (bottom).

The MUSIC detector would have also provided a better charge identification, that would have resulted in a lower cross feed contamination and in a more accurate measurement of the fragment yield in mass fits.

Another eventual advantage (maybe the main one) to have a tracking detector after the magnet would have been the reduction of the combinatorial background: the global track reconstruction would have been much easier. This background is the main limit to the FIRST measurement, producing a not negligible uncertainty on the fragment yield measured from the mass distributions. In summary such a

tracking device could give the following advantages: reduction of the combinatorial background, better mass resolution, better isotope separation and a more accurate measurement of the fragmentation cross sections.

5.1 A possible upgrade of the FIRST setup: the FINUDA drift chambers

In order to solve the problems above mentioned, the idea to use the drift chambers of the FINUDA experiment [123], has been proposed for a possible upgrade of the FIRST detector in the next future.

FINUDA drift chambers (FDCs) could be operated as tracking system after the magnet without introducing high fragmentation, due to the very thin mylar window (36 μm in total for each chamber). On top of that their design follows the FIRST tracking system requirements of large acceptance, transparency and high spatial resolution.

In the FINUDA experiment were present 20 drift chambers, of two different geometries and dimensions ($123 \times 39 \times 6 \text{ cm}^3$ the small ones and $187 \times 68 \times 6 \text{ cm}^3$ the big ones), and those chambers are available at LNF laboratories. FDCs are rectangular wires chambers with resistive anodes ($\sim 2 \text{ k}\Omega/\text{m}$), where the coordinate along the sense wire can be obtained by the charge division method.

Each drift chamber is built up of five glass fiber frames supporting mylar, cathode and anode wires and two external aluminum frames, necessary to strenghten the structure and to give the exact positioning for the anode and cathode frames, as shown in Fig. 5.1. Each mylar frame support two layers of mylar foils for a total thickness of 18 μm per frame, with a thin aluminium coating (30 nm) of the mylar sheet, in order to get a better uniformity of the electric field inside the drift cell. The wires are parallel to each other and to the long side of the drift chamber.

The drift cell scheme is shown in Fig.5.2. Each chamber is composed of contiguous drift cells, 5 cm wide: 6 for the small and 11 for the big chambers. The drift cell

5.1. A POSSIBLE UPGRADE OF THE FIRST SETUP: THE FINUDA DRIFT CHAMBERS

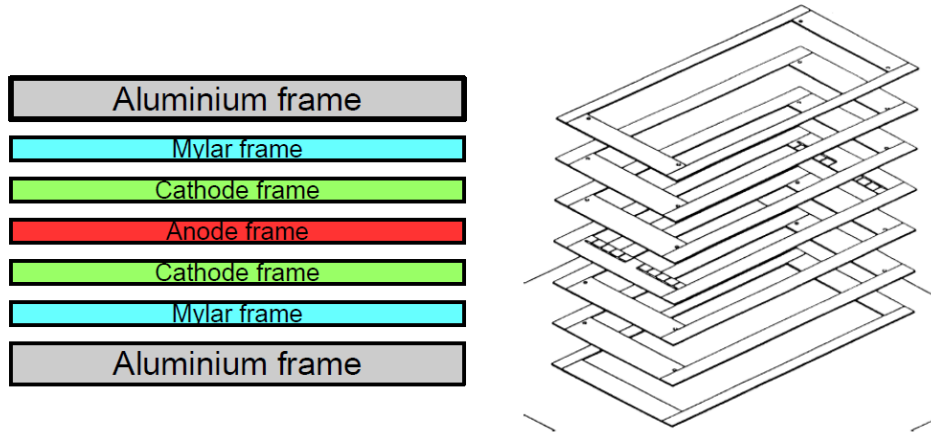


Figure 5.1: Schematic view of the order and of the composition of the FINUDA drift chambers frames

is closed on the top and on the bottom by two parallel layers of copper-beryllium cathode wires, 50 μm diameter, at a relative distance of 6 mm: the cathode wires pitch is 1 mm. In the center of the drift cell a couple of 25 μm diameter stainless steel anode wires, placed at a relative distance of 200 μm , are needed in order to eliminate the left-right ambiguity in tracks reconstruction. The drift cell is enclosed on the border by a couple of field wires, of same type of the cathode wires, that lies on the anode plane at a relative distance of 50 mm.

If the z axis follows the beam direction that cross the chamber orthogonally, each chamber allows to measure two spatial coordinates: y by the measurement of the drift time of the ionization produced in the drift cell, and x with the charge division method. The greatly improved spatial resolution along y , with respect than the one of the TW $\sigma_y \sim 2\text{-}5$ cm, can improve the capability of rating the global tracks through the scoring function $S(y, Z)$ (see equation 4.5), as discussed in § 4.1.3.

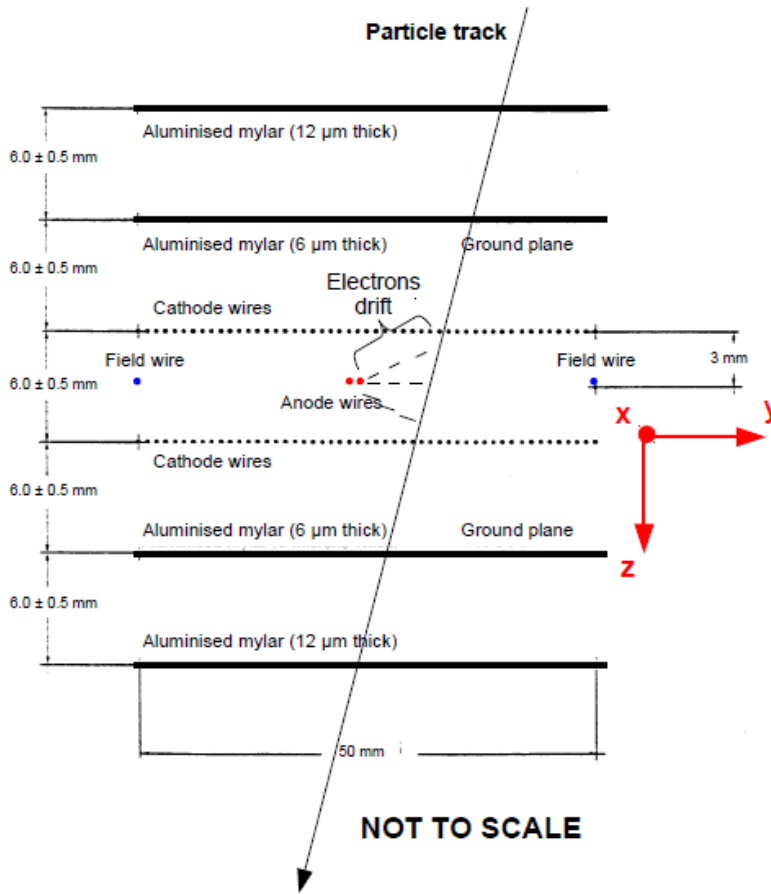


Figure 5.2: Schematic view of the drift cell, obtained by sectioning the drift chamber with a plane orthogonal to the wires [123].

5.1.1 Monte Carlo Simulation

The FDCs have been simulated in detail with FLUKA and included in the full MC of the FIRST experiment, as shown in Fig.5.3, in order to estimate the secondary fragmentation produced inside them. The cathode and anode wires planes, of the four simulated big FDCs, have been arranged parallel to the TW detector planes: as previously stated, in this geometry the y coordinate is obtained by the measured drift time, while the x coordinate is provided by the charge division method. The

5.1. A POSSIBLE UPGRADE OF THE FIRST SETUP: THE FINUDA DRIFT CHAMBERS

MUSIC detector has been removed from the MC and air was put in the magnet and in the region previously occupied by the TPC. Both small and large FDCs have been simulated: a maximum of 6 chambers, 2 small before the magnet and 4 big between ALADIN and the TW, can be inserted in the FIRST setup. In order to easily study the differences between different configurations, it has been implemented a system able to select the desired chamber and insert it into the MC. An algorithm that computes the minimum distance approach of tracks from anode wires has been implemented. The simulation follows the scheme of the other FIRST sub-detectors and the results from the FDCs are stored in the same ROOT file of the full MC.

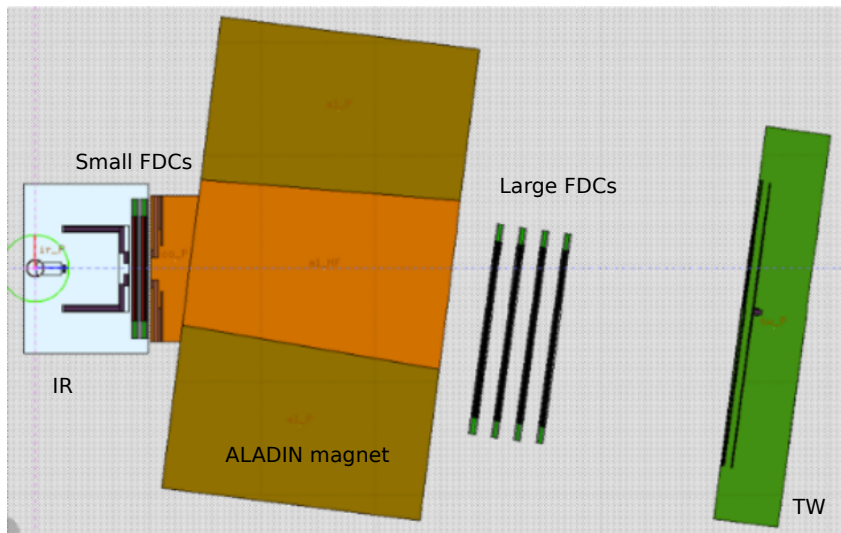


Figure 5.3: Detailed simulation of the FDCs included in the full MC of the FIRST experiment. In the figure two small FDCs have been introduced between the KENTROS detector and the ALADIN magnet, while 4 big FDCs have been inserted between the magnet and the TW,

We evaluated the fragments yield produced in the FDCs and in the air, in the magnet and in the MUSIC region, from the simulation of a ^{12}C ions beam at 400 MeV/nucleon, going through the FIRST apparatus, without any target. Light particles, such as neutrons, hydrogen and helium ions, are the main contribution to the secondary fragmentation inside the chambers. Different combinations of small

and big FDCs have been compared, providing, in all the cases, an overall secondary fragmentation of a few percent respect to the on-target one, as for others FIRST sub-detectors. It must be remarked that final quantitative evaluation of the improvement of the FIRST tracking system, should be evaluated embedding the FDCs in the overall tracks reconstruction. This additional evaluation will be done outside this thesis. In this work we will focus on the possibility of the operation of the FDCs inside the FIRST setup from the hardware point of view.

5.1.2 FINUDA drift chambers test with cosmic rays

A preliminary cosmic rays test of FINUDA small drift chambers has been performed at LNF laboratories (Laboratori Nazionali di Frascati) of the INFN (picture in Fig. 5.4).

The main goal of the test was to study the spatial resolution of the drift chambers for a possible improvement of the fragments tracking system after the magnet in the FIRST apparatus. A small drift chamber has been tested with a Ar/CO₂ (80/20%) gas mixture. This gas mixture is different from the mixture used in the FINUDA experiment where drift chambers were operated with a He-iC₄H₁₀ (70/30%) gas mixture. Unfortunately this hydrocarbons-based mixture cannot be used at FIRST, mainly for safety reasons, and the performance of the Ar-CO₂ gas mixture must be measured. The experimental setup, shown in Fig. 5.5, consists of a trigger system composed of two scintillators with surfaces (20×4) cm² and (20×9) cm² respectively, a small FINUDA test chamber and the read-out system.

The read-out system

The electronic read-out chain consists of a “digital” part and an “analog” part, for the measure of the drift times and of the released charges, respectively, as shown in Fig. 5.6. The digital part of the electronic chain consists of a discriminator followed by a TDC, aimed to provide the spatial resolution of the coordinate along the drift direction (*y* coordinate). The analog part consists of a QDC and an electronic

5.1. A POSSIBLE UPGRADE OF THE FIRST SETUP: THE FINUDA DRIFT CHAMBERS



Figure 5.4: Photo of the setup for the cosmic rays test performed with a small FDC at the LNF laboratories of INFN. The drift chamber is clearly visible in the center of the photo, with mylar windows covered by iron sheet, in order to avoid mylar breaking. On the top and on the bottom of the chamber the two scintillators used as trigger system are arranged orthogonally with respect to the chamber wires. On the right the electronic chain is visible, with discriminators, TDC, QDC, receiver and Linear Gate modules placed in 6U and 9U VME racks. High and low voltage power supplies are also visible on the top and on the bottom of the crate.

system, called Linear Gate, which allows to perform a precise charge division measurement of the longitudinal coordinate. The discriminator accepts 32 analog input and provides 32 analog output, transmitted in the analog part of the electronic chain without any modification, and other 32 output, transmitted to the digital part, that have to trigger the discriminator to be digitized by the TDC.

The most delicate part of the electronic chain is the one dedicated to the measurement of the coordinate along the wire with the charge division method [124, 125, 126]. The charge division method has intrinsic limitations to the accuracy due to the signal to noise ratio. The drifting charges, producing the pulses on the doublet

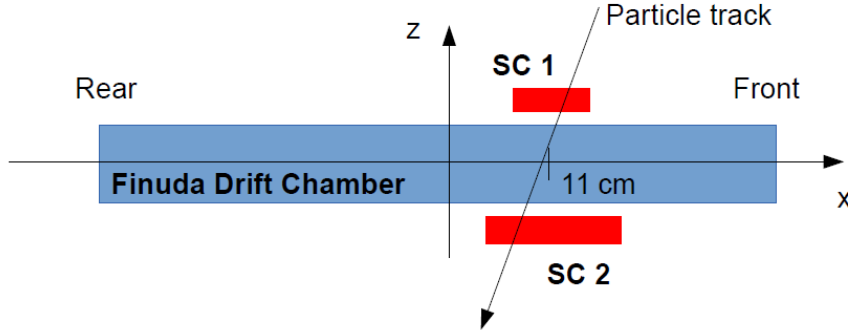


Figure 5.5: Scheme of the cosmic rays test. The small FDC is represented in blue, while the two trigger scintillators (SC 1 and SC 2) are shown in red.

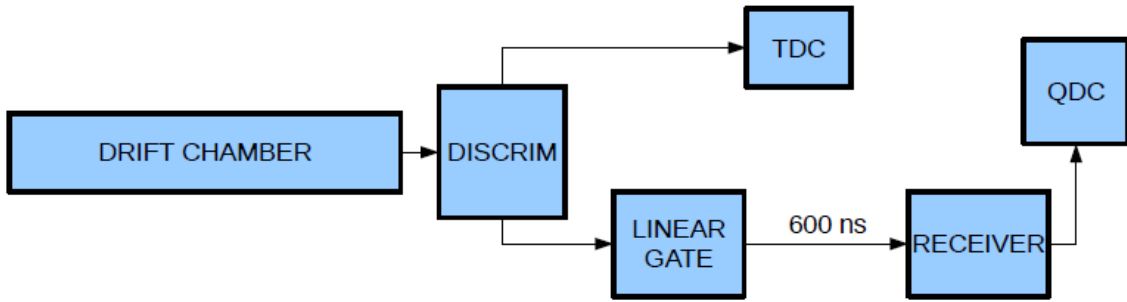


Figure 5.6: Block diagram of the FDC readout.

of wires, give a negative signal on the closest wire and a positive induced one on the other. In order to optimize the signal to noise ratio, a dedicated twin amplifier working on both signals of the doublet has been developed. A block diagram of the circuit is shown in Fig. 5.7. The amplifier couples the signals from the two doublet wires, adding to each one the other with inverse polarity. The signal to noise ratio, with the twin amplifier, is about 30% better than with the normal coupling, in case of completely uncorrelated noise [124]. Moreover, and even more important, this system will automatically cancel the common noise, giving signals of the same polarity on both wires: as a consequence, an improvement greater than 30% can be

5.1. A POSSIBLE UPGRADE OF THE FIRST SETUP: THE FINUDA DRIFT CHAMBERS

obtained, depending on the significance of the common noise contribution.

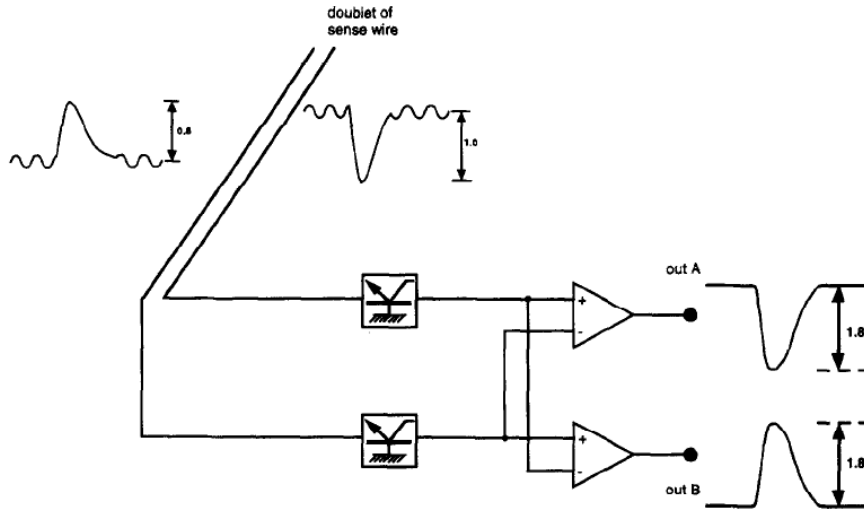


Figure 5.7: Block diagram of the twin amplifier circuit [124].

The sense wires of the FDCs are kept at high voltage, so decoupling capacitors are required to read the signal at the ends of the wires: the capacitance value is chosen in such a way that the energy stored in the capacitor is small enough to avoid a wire breaking. When the current signal, due to the passage of an ionizing particle, vanishes, there is a voltage difference between the two capacitors. These are connected in series through the sense wire, so a current from one capacitor to the other is developed, in a time dependent on the time constant of the circuit, introduced by the decoupling capacitors (Fig. 5.8). This means that, if the QDC gate is open for all the drift time, a charge is added on one side and taken away from the other, giving a systematic longitudinal coordinate compression.

In order to measure the charge and to perform a more precise x-coordinate measurement, it is necessary to select only a limited part of the anode pulse. The Linear Gate [126], shown in Fig. 5.8, has been designed to fulfill this purpose: it opens a temporal gate (120 ns) at the arrival of the signal and then delivers, at its output, a pulse of amplitude linearly dependent from the input value. The Linear Gate sums the front and the rear of each wire, after the front-end amplification,

and if the sum is greater than the threshold of 30 mV it opens, and allows the two signals to pass through and to be transmitted to the QDC. The system works as on-off analog switch: in the on position it allows the signal to pass through, while in the off position it prevents further signal propagation to the QDCs. The left and the right signals of the sense wire coming from the wire amplifiers are applied to the circuit and added together to trigger a one-shot circuit. The output squared pulse (120 ns) is used to open the gate. Meanwhile, the analog signals are delayed and applied to the analog input gate (see Fig.5.8). The output circuit converts the unipolar signal to a differential one in order to drive long (90 m) twisted pair cables, that introduce a delay of ~ 600 ns. The integration and attenuation effects of the twisted cables require a frequency and voltage compensation. For this reason, at the end of the delay line, a receiver overcompensates the signal to obtain a good rise time, before entering in the QDC.

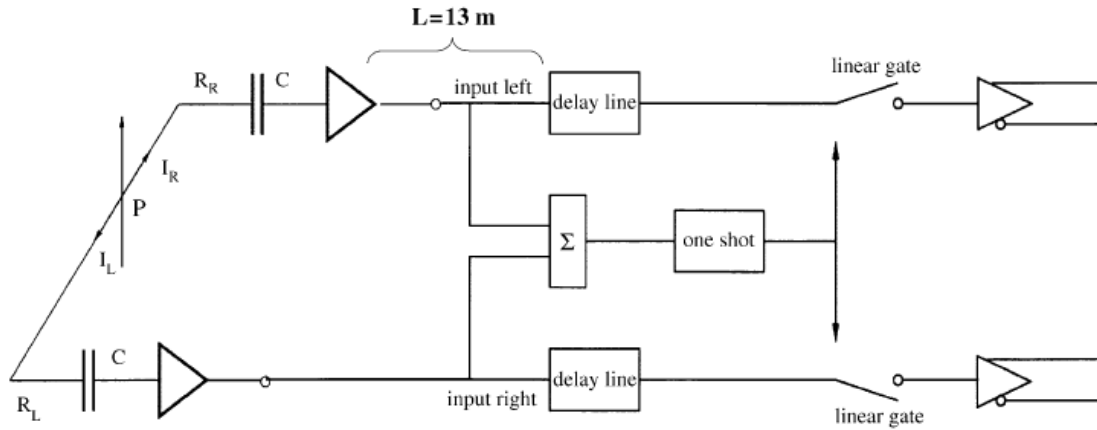


Figure 5.8: Electrical scheme of the sense wire with its front-end electronics and block diagram of the Linear Gate [126].

A small chamber is composed of 6 cells and 12 sense wires, therefore its read-out needs 24 analog and 24 digital electronic channels, being read both the ends of the sense wires. For such purpose the following CAEN modules have been used:

- Double Threshold Discriminator: 32 digital and 32 analog channels (model

5.1. A POSSIBLE UPGRADE OF THE FIRST SETUP: THE FINUDA DRIFT CHAMBERS

VN663)

- TDC: 64 channels, resolution ~ 1 ns (model v673A)
- Linear Gate and receiver: 32 channels. Between them a delay line of twisted cables of 600 ns
- QDC: 64 channels, resolution ~ 400 fC/counts (model VN1465)

The DAQ has been performed using a VME bridge model v1718 (CAEN), interfaced with a host PC through a USB port, together with two dual timer modules (CAEN model N93B).

Spatial resolution measurements

The small drift chamber has been tested at the operating voltage of +1620 V applied to anodes and -3340 V applied to cathodes, for which the chamber efficiency is $\sim 96.0\%$, with a discriminator threshold of 40 mV. At this working voltage signal rise time is less than 40 ns and its amplitude is in the range $\sim 50 - 350$ mV. In Fig.5.9, on the left, is shown the signal (in magenta) as it exits from the discriminator and enter in the TDC and in the Linear Gate. The TDC operates in common stop mode and acquires only signals in a temporal gate of 1 μ s before the common stop signal (in green). On the right of Fig. 5.9 is shown the signal (in cyan) after exiting from the Linear Gate and receiver, delayed of 600 ns, and the QDC gate, 1 μ s long, in yellow.

The time distributions obtained with the TDC of two sense wires named 4A and 3B are shown in Fig.5.10, for both the ends of the wires (“front” and “rear”). Some qualitative considerations about the time distributions can be made:

- TDC works in common stop mode, so the events at 760 ns are the ones near the anode
- The time jitter of the signal is ~ 500 ns

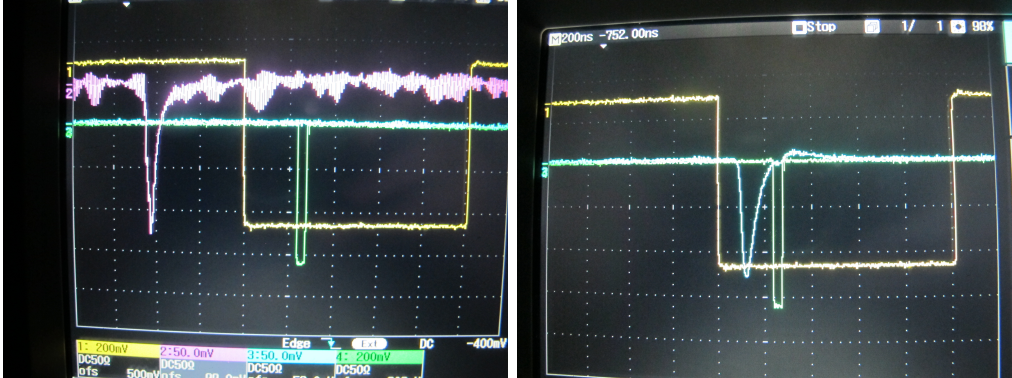


Figure 5.9: Signals at the oscilloscope: vertical scale: 50 mV/division, horizontal scale: 200 ns/division. On the left in magenta the signal after the discriminator is shown. In green and in yellow the common stop signal for TDC acquisition and the QDC gate of 1 μ s are respectively shown. On the right in cyan the signal, delayed of 600 ns after the Linear Gate and the receiver.

- In a naive constant velocity model the drift velocity can be estimated from the maximum drift time and the cell dimension read from one wire of the doublet (2.5 cm): $v_{drift} \sim 50 \mu\text{m/ns}$
- The distributions are “almost” flats as expected with cosmic rays (randomly distributed), so the drift velocity can be expected “almost” saturated
- The excess of counts near the anode (at ~ 760 ns) can be due to the small number of events that cross the cell in the region between the two anode wires and maybe also to a non complete saturation of the drift velocity
- The spatial resolution, along the drift direction (y direction), can be roughly estimated from product of the rise of the time distribution near the anode (~ 20 ns) and the drift velocity (50 $\mu\text{m/ns}$). This results in a spatial resolution of ~ 1 mm along the drift direction (x coordinate).

However, the spatial accuracy of a drift chamber largely depends on the precise knowledge of the drift space-time relations, which in turn depends on the gas mixture

5.1. A POSSIBLE UPGRADE OF THE FIRST SETUP: THE FINUDA DRIFT CHAMBERS

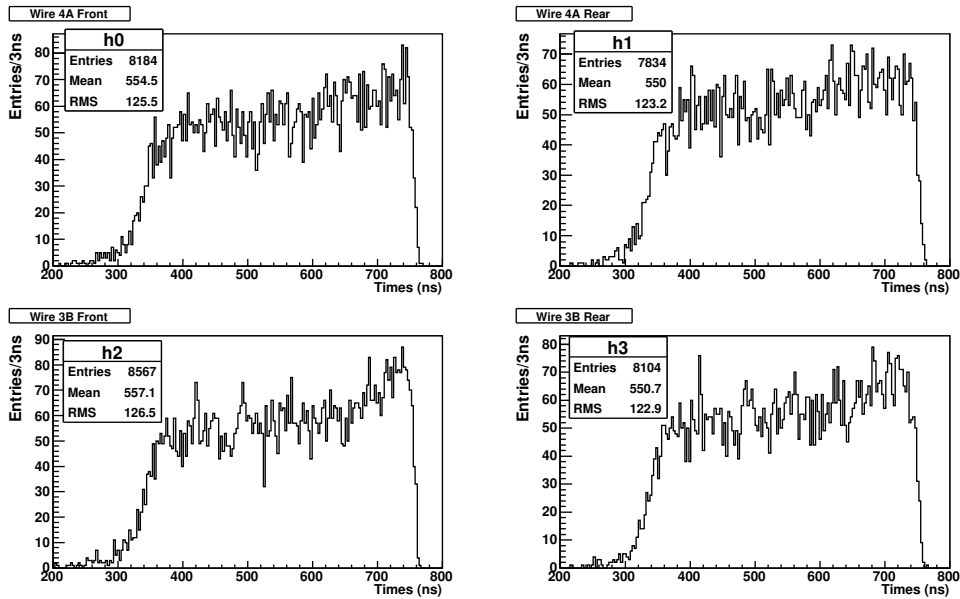


Figure 5.10: Time distributions for sense wires 4A and 3B read on both wire ends, front and rear.

employed and the electric field in the cell. An accurate model of the drift cell is therefore essential for high precision track reconstruction.

The charge distributions obtained with the QDC for the sense wire 3B are shown in Fig.5.11, for both the ends of the wire (“front” is channel 12 and “rear” is channel 13). For this working voltage the signal is well separated from the noise, that has to be subtracted from charge distributions. The acquisition of pedestals has been possible sending a NIM signal to a special input of the Linear Gate that so opens the gates for signals of each amplitude.

The coordinate along the wire with the charge division method is given by the formula:

$$x = k \times (Q_f - Q_r)/(Q_f + Q_r) \quad (5.2)$$

where k is a proportionality factor depending on the wire resistivity and length and $Q_{f,r}$ is the front and rear charge measured by QDC. Taking the mean value and the

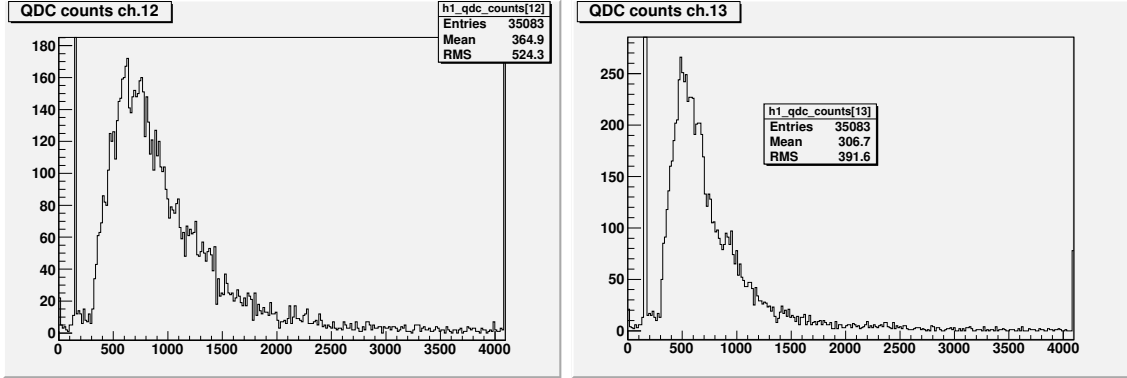


Figure 5.11: Charge distributions for sense wire 3B read on both wire ends, front (channel 12) and rear (channel 13).

rms of the distribution of the quantity $(Q_f - Q_r)/(Q_f + Q_r)$, shown in Fig.5.12 and exploiting the knowledge of the position of the trigger respect to the center of the sense wire (11 cm towards the front of the wire as shown in Fig. 5.5), it has been possible to estimate a resolution along x coordinate of ~ 3 cm. This first estimation is an upper limit to the x resolution and is limited both from the oversimplified calculation and from the poor knowledge of the trigger position due to the large size of the trigger scintillators (9 cm and 4 cm wide).

5.1.3 Final considerations

By the measured time and charge distributions it has been possible to give a first estimation of the spatial resolution of the chamber: 1 mm along the drift direction and 3 cm along the sense wire. These values are preliminary results and have to be considered as upper limits for the reasons discussed above. A test beam with ions beams is mandatory to properly measure the spatial resolution of the FDCs and their dynamic range with respect to the different energy released by ions with charges $Z = 1 - 6$.

As far as the changes of the FIRST setup according to the MC simulation the best configuration for the FIRST experiment is made of four big FDCs after the

5.1. A POSSIBLE UPGRADE OF THE FIRST SETUP: THE FINUDA DRIFT CHAMBERS

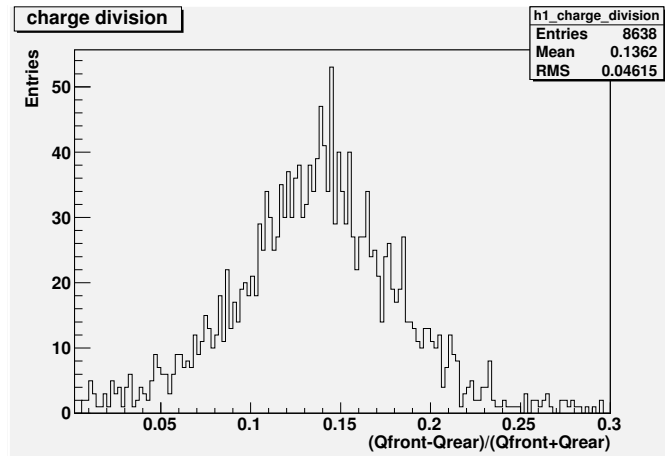


Figure 5.12: Distributions of the normalized front/rear charge difference for sense wire 3B. From the mean and the rms of such distribution and the charge division method formula 5.2 has been possible to estimate an upper limit to the x coordinate resolution.

ALADIN magnet. The two couples of FDCs could be operated to different voltage in order to achieve the required wide dynamic range with this tracking system. This could be an easy solution respect to modify the front-end electronics of the chambers.

These studies have shown that FDCs can provide the desired tracking performances for a possible upgrade of the FIRST apparatus. In particular the spatial resolution along the drift direction $\sigma_y < 1$ mm (to be compared to that provided by the TW detector: $\sigma_y \sim 2 - 5$ cm) could significantly improve the capability of the tracking algorithm in the matching of TW-VTX hits. This could translate in a reduction of the combinatorial background, that is an important source of uncertainty in the FIRST measurement. The resolution along the x coordinate could as well provide little improvement to the momentum and mass resolutions useful for a better isotope peaks separation (according to FINUDA measurements a resolution of the order of the 1% of the wire length, equivalent to ~ 1 cm, can be achieved).

Conclusions

This thesis described the analysis of the data collected with the FIRST apparatus for the measurement of the fragmentation cross sections in the interaction of a 400 MeV/nucleon ^{12}C beam on thin targets. The data collected at the SIS accelerator of the GSI laboratory have been analyzed to measure the fragmentation differential cross sections as a function of the emission angle θ and the kinetic energy E_{kin} . The present analysis was focused on the fragments emitted at angles $\theta \lesssim 6^\circ$, in the angular acceptance of the ALADIN magnet.

A gold and a composite targets were used for the FIRST data taking for the fragmentation study of the ^{12}C beam. In particular the composite target has a composition shown in Table 3.1 of chapter 3. In this target, namely C, O, P and Ca, that constitute the 85% of the elemental composition of the target, are elements constituting the human body, and so are of interest for particle therapy applications. The data obtained from this target can be evaluable benchmarking for MC model of fragmentation of carbon on C, O, P and Ca.

A second main item of this thesis is related with a possible improvement of the FIRST tracking system. In particular the lack of a tracking device between the magnet and the TW detector made the calibration of the single devices and the matching between the tracks before the magnet and the hits in the TW after the magnet a very delicate procedure. In this framework I have been commissioned to a design study, both from a hardware and from a MC point of view, that would produce a first evaluation of the use of the FINUDA drift chambers in the FIRST setup. The FDCs have been included in the full MC simulation of the FIRST experiment and

have been tested with cosmic rays at the LNF laboratories of INFN. Such studies have shown the possibility to improve the FIRST apparatus with these detectors (chapter 5).

Main part of my PhD work has been devoted to understand and improve the calibration and alignment procedure and to refine the reconstruction algorithms. In particular, a big effort has been dedicated to the E_{loss} calibration of the TW detector and to the development of the charge identification algorithms performed with the TW and the VTX detectors, as shown in chapter 3.

The chapter 4 contains the great part of my original contribution to data analysis. The reconstruction algorithm has been optimized in some parts and validated with Monte Carlo studies. The global reconstruction algorithms have been validated and benchmarked against the full MC simulation. The angular and kinetic energy resolutions have been measured in order to evaluate any possible bias introduced by the reconstruction algorithm and to optimize the binning adopted for the cross section measurement. The background characterization has been studied using the full MC simulation as well, by looking at the tracks at generator level. The observed discrepancies between the collected data and the MC simulation have been taken into account when assessing the systematic uncertainties of the result.

The algorithms and the analysis strategies described in chapter 4 and used for the measurement of the cross sections have been developed within this thesis, included the procedure to correct for all the efficiencies and for the contamination from combinatorial background. The tracking efficiencies have been measured using a dedicated MC in which fragments of each detected isotope have been generated inside the target and their tracks have been reconstructed using the FIRST tracking algorithms.

A huge work has been done in order to estimate the contribution from different isotopes to the cross section. The fragment yields have been measured fitting the mass distributions for each energy and angular bin. The obtained yields have been corrected bin by bin for the cross feed correction, that takes into account for the misidentified tracks by the Z_{ID} algorithm. Mass fits and cross feed evaluation

CONCLUSIONS

required a careful and an accurate study performed on a large number of bins.

The differential cross sections have been measured for all the elements and isotopes produced in the fragmentation of the primary carbons interacting with the target. Also the total charge changing cross sections have been measured. The analysis has been redone several times, changing the reconstruction algorithms, MC samples, measurement strategies in order to assign a systematic uncertainty to the measured cross sections.

The FIRST collaboration is going to publish these results, and a paper is in preparation to provide data that will reduce the gap of the existing measurements and will help to improve the nuclear models used for particle therapy and space radiation protection applications.

Appendix A

Isotopic cross sections

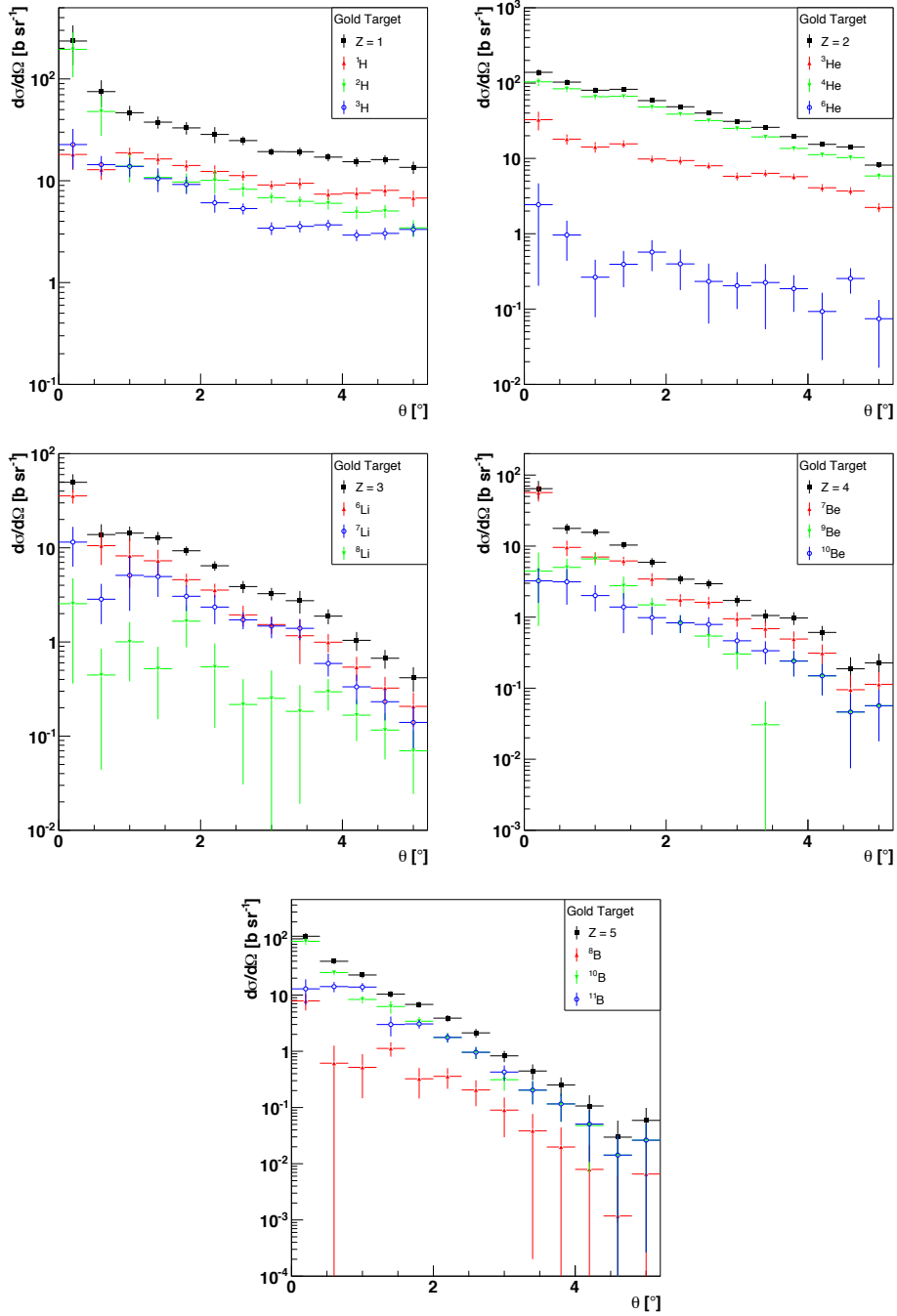


Figure A.1: Isotopic differential cross sections for the gold target, as a function of the fragment angle with respect to the beam axis, computed using Eq. 4.7. The results for each isotope are shown separately, together with their sum (in black squares). The total uncertainty (statistic and systematic added in quadrature) is shown.

APPENDIX A. ISOTOPIC CROSS SECTIONS

Table A.1: Cross sections as a function of the angle θ for the gold target. The values in parentheses represent the uncertainties [8.2 (0.5) is equivalent to 8.2 ± 0.5].

θ (deg)	1H $d\sigma/d\Omega$ [b-sr $^{-1}$]	2H $d\sigma/d\Omega$ [b-sr $^{-1}$]	3H $d\sigma/d\Omega$ [b-sr $^{-1}$]	3He $d\sigma/d\Omega$ [b-sr $^{-1}$]	4He $d\sigma/d\Omega$ [b-sr $^{-1}$]	6He $d\sigma/d\Omega$ [b-sr $^{-1}$]
0.2 (0.2)	22 (5.6)	2.6e+02 (95)	31 (11)	33 (9.1)	1.1e+02 (17)	3.3 (2.3)
0.6 (0.2)	15 (3.6)	59 (20)	18 (3.3)	18 (2.6)	89 (12)	0.8 (0.59)
1 (0.2)	22 (2.8)	15 (4.5)	18 (3.2)	15 (2.7)	70 (8.4)	0.15 (0.19)
1.4 (0.2)	19 (2.7)	12 (1.7)	13 (2.9)	18 (2.3)	73 (7.7)	0.37 (0.22)
1.8 (0.2)	17 (1.9)	12 (2.5)	12 (1.6)	11 (1.5)	55 (5.7)	0.72 (0.3)
2.2 (0.2)	14 (2.2)	11 (3.1)	7.1 (1.2)	10 (1.7)	44 (4.2)	0.43 (0.27)
2.6 (0.2)	13 (1.3)	10 (1.3)	6.1 (0.84)	9.2 (0.98)	36 (3.1)	0.24 (0.2)
3 (0.2)	10 (1.1)	7.9 (0.9)	3.5 (0.74)	6.5 (0.79)	27 (2.8)	0.19 (0.12)
3.4 (0.2)	11 (1.1)	7.3 (0.98)	4 (0.59)	6.9 (0.83)	21 (1.8)	0.23 (0.19)
3.8 (0.2)	8.4 (0.81)	6.8 (0.68)	4 (0.85)	6.5 (0.64)	15 (1.2)	0.21 (0.11)
4.2 (0.2)	8.3 (0.92)	5.5 (0.68)	3.1 (0.68)	4.4 (0.63)	13 (1.1)	0.13 (0.082)
4.6 (0.2)	9 (0.97)	5.9 (0.64)	3.2 (0.61)	4 (0.47)	10 (1.1)	0.23 (0.098)
5 (0.2)	7.8 (1)	3.8 (0.59)	3.8 (0.62)	2.3 (0.33)	6.3 (0.65)	0.079 (0.06)
θ (deg)	6Li $d\sigma/d\Omega$ [b-sr $^{-1}$]	7Li $d\sigma/d\Omega$ [b-sr $^{-1}$]	8Li $d\sigma/d\Omega$ [b-sr $^{-1}$]	7Be $d\sigma/d\Omega$ [b-sr $^{-1}$]	9Be $d\sigma/d\Omega$ [b-sr $^{-1}$]	^{10}Be $d\sigma/d\Omega$ [b-sr $^{-1}$]
0.2 (0.2)	43 (8)	12 (6.5)	2.4 (2.7)	63 (20)	2.6 (4.9)	2.9 (2.2)
0.6 (0.2)	15 (4.6)	1.8 (1.6)	0.51 (0.52)	14 (3.1)	5.7 (2.1)	5 (2.1)
1 (0.2)	14 (5.1)	3 (3.9)	1.2 (0.73)	8.9 (1.5)	9 (1.7)	2.5 (0.99)
1.4 (0.2)	5.3 (2.7)	8.2 (2.4)	0.31 (0.44)	7.2 (1.1)	3 (1.2)	1.9 (0.95)
1.8 (0.2)	4.9 (0.81)	3.5 (1.4)	2.2 (0.93)	4.1 (0.78)	1.6 (0.59)	0.7 (0.4)
2.2 (0.2)	3.3 (0.63)	3 (0.84)	0.42 (0.53)	2.4 (0.54)	0.98 (0.43)	0.36 (0.23)
2.6 (0.2)	1.7 (0.54)	1.5 (0.36)	0.35 (0.21)	3 (0.51)	1.3 (0.34)	0.13 (0.15)
3 (0.2)	1.3 (0.34)	1.6 (0.43)	0.15 (0.29)	1.7 (0.34)	0.81 (0.26)	0.13 (0.094)
3.4 (0.2)	1.4 (0.28)	0.61 (0.38)	0.47 (0.23)	1.1 (0.31)	0.12 (0.18)	0.29 (0.15)
3.8 (0.2)	1.2 (0.27)	0.69 (0.22)	0.023 (0.093)	1.2 (0.3)	0.11 (0.11)	0.093 (0.078)
4.2 (0.2)	0.23 (0.14)	0.54 (0.18)	0.095 (0.064)	0.51 (0.16)	0.086 (0.067)	0.093 (0.063)
4.6 (0.2)	0.35 (0.18)	0.13 (0.18)	0.063 (0.048)	0.17 (0.082)	2.2e-07 (9.2e-05)	0.035 (0.039)
5 (0.2)	0.26 (0.11)	0.083 (0.069)	0.03 (0.032)	0.17 (0.081)	0.026 (0.034)	6.3e-07 (0.013)
θ (deg)	8B $d\sigma/d\Omega$ [b-sr $^{-1}$]		^{10}B $d\sigma/d\Omega$ [b-sr $^{-1}$]		^{11}B $d\sigma/d\Omega$ [b-sr $^{-1}$]	
0.2 (0.2)	11 (3)		1e+02 (13)		20 (7)	
0.6 (0.2)	0.38 (0.78)		27 (2.9)		17 (3.3)	
1 (0.2)	0.64 (0.36)		8.4 (1.3)		15 (2.4)	
1.4 (0.2)	0.44 (0.24)		7.3 (2.1)		0.49 (1.7)	
1.8 (0.2)	0.052 (2.5)		2.7 (0.69)		2.3 (0.99)	
2.2 (0.2)	0.28 (0.2)		3.4 (1.1)		0.7 (1)	
2.6 (0.2)	0.2 (0.14)		0.41 (0.4)		1.7 (0.6)	
3 (0.2)	0.066 (0.052)		0.3 (0.14)		0.44 (0.17)	
3.4 (0.2)	0.06 (0.044)		0.17 (0.088)		0.15 (0.099)	
3.8 (0.2)	0.024 (0.029)		0.04 (0.043)		0.035 (0.037)	
4.2 (0.2)	1.5e-07 (0.012)		2.9e-10 (3e-06)		0.11 (0.064)	
4.6 (0.2)	3.7e-07 (0.0001)		0.028 (0.031)		6.3e-09 (1.4e-05)	
5 (0.2)	0.021 (0.022)		1.1e-08 (1.5e-05)		0.043 (0.033)	

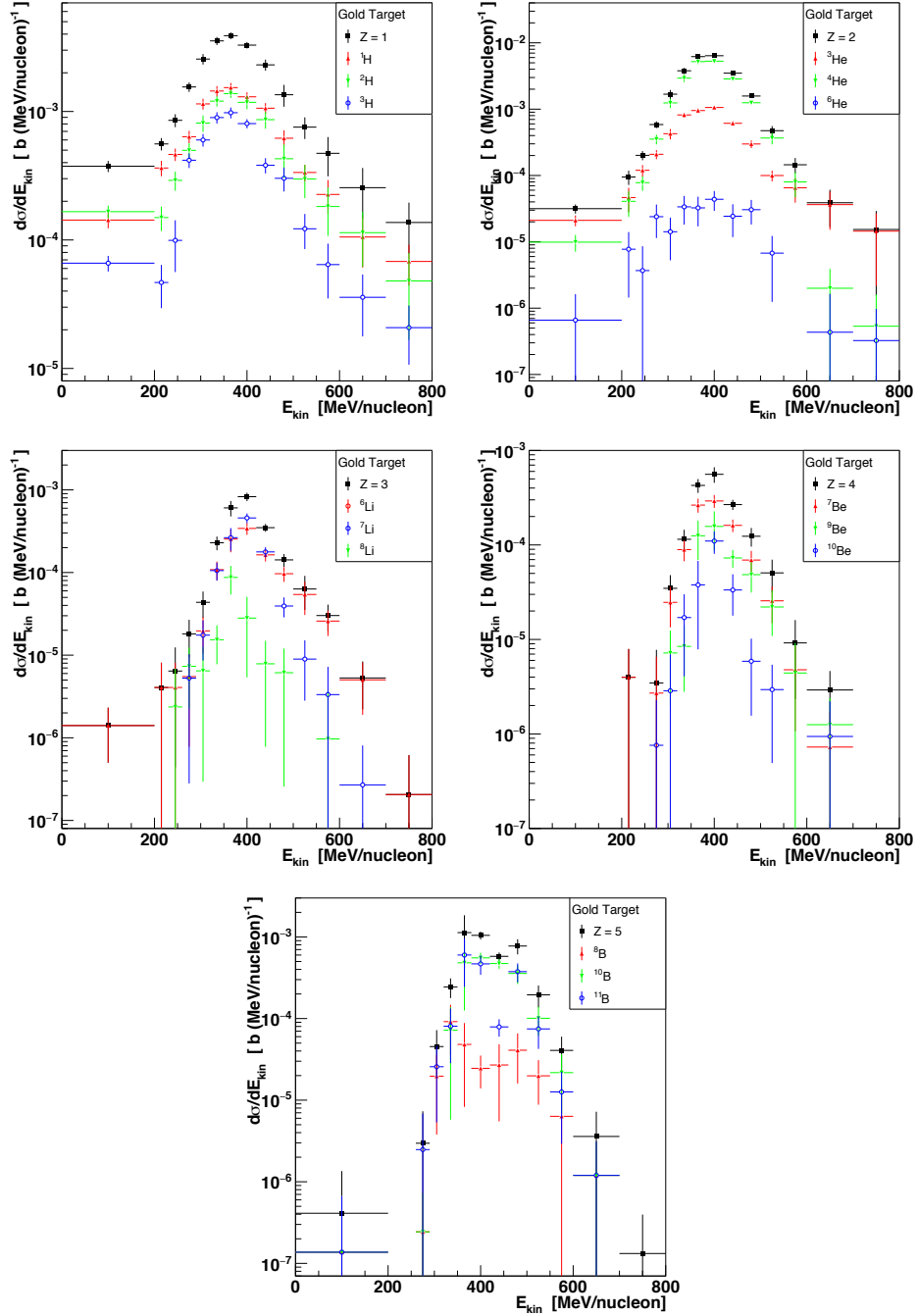


Figure A.2: Isotopic differential cross sections for the gold target, as a function of the fragment normalized kinetic energy, computed using Eq. 4.8 for fragments within the ALADIN angular acceptance ($\lesssim 6^\circ$). The results for each isotope are shown separately, together with their sum (in black squares). The total uncertainty (statistic and systematic added in quadrature) is shown.

APPENDIX A. ISOTOPIC CROSS SECTIONS

Table A.2: Cross sections as a function of the normalized kinetic energy E_{kin} [MeV/u] for the gold target. The values in parentheses represent the uncertainties.

E_{kin} (MeV/u)	1H $d\sigma/dE_{kin}$ [b·(MeV/u) ⁻¹]	2H $d\sigma/dE_{kin}$ [b·(MeV/u) ⁻¹]	3H $d\sigma/dE_{kin}$ [b·(MeV/u) ⁻¹]	3He $d\sigma/dE_{kin}$ [b·(MeV/u) ⁻¹]	4He $d\sigma/dE_{kin}$ [b·(MeV/u) ⁻¹]	6He $d\sigma/dE_{kin}$ [b·(MeV/u) ⁻¹]
100 (100)	1.38e-04 (1.96e-05)	1.61e-04 (1.89e-05)	6.17e-05 (9.17e-06)	2.00e-05 (3.92e-06)	9.78e-06 (2.78e-06)	3.34e-07 (9.64e-07)
215 (15)	3.70e-04 (4.99e-05)	1.60e-04 (3.22e-05)	4.44e-05 (1.72e-05)	5.42e-05 (1.86e-05)	3.85e-05 (1.70e-05)	8.43e-06 (6.29e-06)
245 (15)	4.71e-04 (5.15e-05)	2.71e-04 (4.96e-05)	7.65e-05 (4.30e-05)	1.16e-04 (2.38e-05)	7.07e-05 (1.94e-05)	2.42e-06 (4.88e-06)
275 (15)	6.31e-04 (6.97e-05)	4.85e-04 (6.69e-05)	4.35e-04 (5.45e-05)	2.11e-04 (3.27e-05)	3.27e-04 (5.89e-05)	2.61e-05 (1.25e-05)
305 (15)	1.15e-03 (1.12e-04)	8.33e-04 (1.18e-04)	5.90e-04 (6.72e-05)	4.09e-04 (7.55e-05)	1.14e-03 (1.99e-04)	7.90e-06 (8.92e-06)
335 (15)	1.48e-03 (1.35e-04)	1.25e-03 (1.11e-04)	9.07e-04 (9.06e-05)	8.23e-04 (6.62e-05)	2.89e-03 (3.73e-04)	2.53e-05 (1.55e-05)
365 (15)	1.55e-03 (1.33e-04)	1.38e-03 (1.03e-04)	9.80e-04 (9.54e-05)	9.76e-04 (7.72e-05)	5.12e-03 (4.31e-04)	2.46e-05 (1.54e-05)
400 (20)	1.32e-03 (1.11e-04)	1.20e-03 (1.37e-04)	8.27e-04 (6.60e-05)	1.06e-03 (6.78e-05)	5.31e-03 (2.64e-04)	5.18e-05 (1.45e-05)
440 (20)	1.09e-03 (1.02e-04)	9.31e-04 (1.29e-04)	4.06e-04 (5.17e-05)	6.31e-04 (5.03e-05)	2.88e-03 (1.40e-04)	3.32e-05 (1.25e-05)
480 (20)	6.59e-04 (4.97e-05)	4.80e-04 (1.25e-04)	3.35e-04 (6.35e-05)	3.11e-04 (3.95e-05)	1.28e-03 (8.61e-05)	3.79e-05 (1.23e-05)
525 (25)	3.45e-04 (4.97e-05)	3.25e-04 (8.61e-05)	1.32e-04 (3.72e-05)	1.08e-04 (1.82e-05)	3.53e-04 (7.20e-05)	5.26e-06 (5.51e-06)
575 (25)	2.56e-04 (6.67e-05)	2.08e-04 (7.44e-05)	7.32e-05 (2.93e-05)	8.65e-05 (2.63e-05)	6.25e-05 (3.30e-05)	4.13e-13 (9.40e-10)
650 (50)	1.15e-04 (4.45e-05)	1.39e-04 (5.23e-05)	4.35e-05 (1.80e-05)	3.76e-05 (2.12e-05)	4.46e-14 (1.92e-06)	1.08e-06 (1.21e-06)
750 (50)	7.86e-05 (2.39e-05)	4.51e-05 (3.13e-05)	2.34e-05 (1.01e-05)	1.26e-05 (1.23e-05)	8.55e-13 (1.07e-06)	2.97e-11 (6.49e-07)
E_{kin} (MeV/u)	6Li $d\sigma/dE_{kin}$ [b·(MeV/u) ⁻¹]	7Li $d\sigma/dE_{kin}$ [b·(MeV/u) ⁻¹]	8Li $d\sigma/dE_{kin}$ [b·(MeV/u) ⁻¹]	7Be $d\sigma/dE_{kin}$ [b·(MeV/u) ⁻¹]	9Be $d\sigma/dE_{kin}$ [b·(MeV/u) ⁻¹]	^{10}Be $d\sigma/dE_{kin}$ [b·(MeV/u) ⁻¹]
100 (100)	1.29e-06 (9.07e-07)	5.83e-12 (1.88e-09)	6.00e-12 (1.91e-09)	6.25e-15 (6.09e-11)	6.25e-15 (6.09e-11)	6.20e-15 (6.06e-11)
215 (15)	4.04e-06 (4.04e-06)	3.46e-12 (3.74e-09)	3.31e-12 (3.66e-09)	3.95e-06 (3.95e-06)	4.55e-13 (1.34e-09)	2.59e-14 (3.20e-10)
245 (15)	4.04e-06 (4.05e-06)	2.62e-14 (3.25e-10)	4.04e-06 (4.48e-06)	5.29e-14 (4.57e-10)	5.29e-14 (4.57e-10)	5.29e-14 (4.57e-10)
275 (15)	5.41e-06 (4.73e-06)	3.53e-06 (5.00e-06)	3.85e-06 (5.06e-06)	3.33e-06 (3.87e-06)	6.35e-11 (1.58e-08)	6.38e-11 (1.52e-06)
305 (15)	1.83e-05 (9.27e-06)	1.82e-05 (8.85e-06)	1.79e-06 (6.16e-06)	2.21e-05 (1.13e-05)	6.89e-06 (5.23e-06)	3.70e-06 (4.09e-06)
335 (15)	1.11e-04 (2.72e-05)	1.16e-04 (2.59e-05)	1.37e-05 (7.61e-06)	8.88e-05 (2.21e-05)	9.99e-06 (5.65e-06)	9.52e-06 (1.30e-05)
365 (15)	2.18e-04 (7.85e-05)	2.06e-04 (8.10e-05)	1.07e-04 (3.31e-05)	2.72e-04 (4.46e-05)	1.33e-04 (5.55e-05)	3.56e-05 (2.99e-05)
400 (20)	3.77e-04 (5.61e-05)	4.92e-04 (6.12e-05)	1.80e-05 (2.27e-05)	2.96e-04 (4.54e-05)	1.59e-04 (6.96e-05)	8.50e-05 (2.95e-05)
440 (20)	1.36e-04 (2.76e-05)	1.80e-04 (2.48e-05)	4.68e-06 (7.08e-06)	1.60e-04 (2.44e-05)	7.09e-05 (1.55e-05)	3.36e-05 (1.55e-05)
480 (20)	1.02e-04 (1.97e-05)	3.66e-05 (1.06e-05)	4.60e-06 (5.87e-06)	7.83e-05 (1.73e-05)	5.45e-05 (1.72e-05)	7.78e-06 (4.32e-06)
525 (25)	4.57e-05 (2.36e-05)	5.19e-06 (6.14e-06)	2.88e-14 (2.64e-10)	2.05e-05 (1.08e-05)	2.03e-05 (1.12e-05)	1.96e-06 (2.45e-06)
575 (25)	2.91e-05 (8.82e-06)	4.84e-06 (3.89e-06)	2.42e-06 (2.70e-06)	4.74e-06 (3.71e-06)	2.37e-06 (4.75e-06)	6.05e-15 (1.20e-10)
650 (50)	6.01e-06 (3.13e-06)	8.72e-11 (5.39e-07)	2.03e-10 (1.57e-08)	7.64e-13 (9.78e-07)	8.74e-07 (1.16e-06)	1.18e-06 (1.27e-06)
750 (50)	4.62e-13 (4.12e-07)	4.62e-13 (7.48e-10)	4.62e-13 (7.48e-10)	0.00e+00 (0.00e+00)	0.00e+00 (0.00e+00)	0.00e+00 (0.00e+00)
E_{kin} (MeV/u)	8Bo $d\sigma/dE_{kin}$ [b·(MeV/u) ⁻¹]		^{10}Bo $d\sigma/dE_{kin}$ [b·(MeV/u) ⁻¹]		^{11}Bo $d\sigma/dE_{kin}$ [b·(MeV/u) ⁻¹]	
100 (100)	1.68e-07 (5.34e-07)		1.68e-07 (5.34e-07)		1.68e-07 (5.34e-07)	
215 (15)	0.00e+00 (0.00e+00)		0.00e+00 (0.00e+00)		0.00e+00 (0.00e+00)	
245 (15)	0.00e+00 (6.90e-14)		0.00e+00 (6.90e-14)		0.00e+00 (6.90e-14)	
275 (15)	0.00e+00 (4.87e-07)		0.00e+00 (4.87e-07)		0.00e+00 (4.37e-06)	
305 (15)	2.13e-05 (1.59e-05)		3.64e-11 (2.02e-08)		3.17e-05 (2.03e-05)	
335 (15)	1.40e-04 (5.59e-05)		5.85e-05 (6.62e-05)		6.61e-05 (5.23e-05)	
365 (15)	5.72e-05 (3.99e-05)		6.11e-04 (3.57e-04)		5.96e-04 (3.56e-04)	
400 (20)	2.84e-05 (1.06e-05)		5.96e-04 (8.65e-05)		4.84e-04 (1.25e-04)	
440 (20)	4.99e-05 (2.15e-05)		5.10e-04 (6.51e-05)		6.76e-05 (1.89e-05)	
480 (20)	5.58e-05 (2.49e-05)		4.20e-04 (9.28e-05)		3.57e-04 (9.75e-05)	
525 (25)	1.78e-05 (1.11e-05)		1.12e-04 (3.90e-05)		8.74e-05 (3.21e-05)	
575 (25)	6.70e-06 (8.07e-06)		2.68e-05 (1.50e-05)		1.34e-05 (9.69e-06)	
650 (50)	1.01e-06 (1.92e-06)		1.01e-06 (1.92e-06)		1.01e-06 (1.92e-06)	
750 (50)	0.00e+00 (8.80e-08)		0.00e+00 (8.80e-08)		0.00e+00 (8.80e-08)	

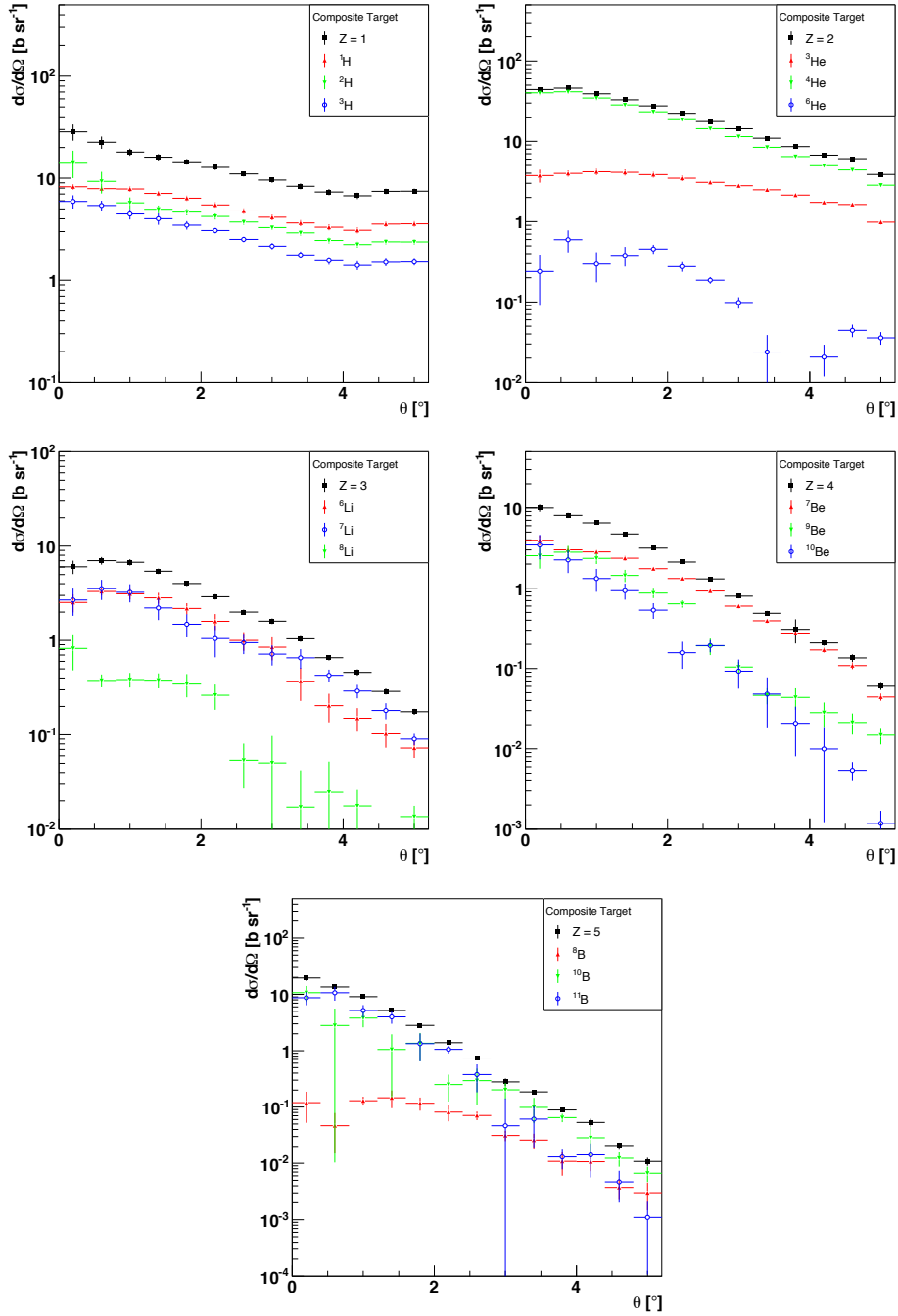


Figure A.3: Isotopic differential cross sections for the composite target, as a function of the fragment angle with respect to the beam axis, computed using Eq. 4.7. The results for each isotope are shown separately, together with their sum (in black squares). The total uncertainty (statistic and systematic added in quadrature) is shown.

APPENDIX A. ISOTOPIC CROSS SECTIONS

Table A.3: Cross sections as a function of the angle θ for the composite target. The values in parentheses represent the uncertainties [8.2 (0.5) is equivalent to 8.2 ± 0.5].

θ (deg)	1H $d\sigma/d\Omega$ [b-sr $^{-1}$]	2H $d\sigma/d\Omega$ [b-sr $^{-1}$]	3H $d\sigma/d\Omega$ [b-sr $^{-1}$]	3He $d\sigma/d\Omega$ [b-sr $^{-1}$]	4He $d\sigma/d\Omega$ [b-sr $^{-1}$]	6He $d\sigma/d\Omega$ [b-sr $^{-1}$]
0.2 (0.2)	8.2 (0.5)	16 (4.3)	6 (0.88)	3.6 (0.69)	40 (2.6)	0.11 (0.15)
0.6 (0.2)	7.9 (0.45)	9.6 (2.2)	5.5 (0.61)	3.9 (0.34)	41 (2.5)	0.61 (0.18)
1 (0.2)	7.8 (0.44)	5.7 (0.74)	4.5 (0.52)	4.1 (0.36)	34 (2.1)	0.28 (0.12)
1.4 (0.2)	7.1 (0.4)	5 (0.43)	4.1 (0.51)	4 (0.35)	28 (1.6)	0.37 (0.11)
1.8 (0.2)	6.4 (0.37)	4.7 (0.33)	3.5 (0.33)	3.8 (0.31)	23 (1.3)	0.45 (0.059)
2.2 (0.2)	5.5 (0.33)	4.2 (0.28)	3.1 (0.19)	3.4 (0.26)	19 (1)	0.26 (0.038)
2.6 (0.2)	4.8 (0.29)	3.7 (0.22)	2.5 (0.15)	3.1 (0.19)	14 (0.77)	0.19 (0.018)
3 (0.2)	4.1 (0.26)	3.3 (0.18)	2.1 (0.15)	2.8 (0.17)	11 (0.62)	0.095 (0.016)
3.4 (0.2)	3.6 (0.24)	2.9 (0.17)	1.8 (0.14)	2.5 (0.14)	8.4 (0.47)	0.019 (0.015)
3.8 (0.2)	3.3 (0.22)	2.4 (0.16)	1.5 (0.14)	2.1 (0.12)	6.4 (0.35)	7.3e-08 (0.0055)
4.2 (0.2)	3 (0.2)	2.2 (0.15)	1.4 (0.14)	1.7 (0.096)	4.9 (0.27)	0.026 (0.0088)
4.6 (0.2)	3.5 (0.21)	2.4 (0.13)	1.5 (0.13)	1.6 (0.091)	4.4 (0.25)	0.049 (0.0079)
5 (0.2)	3.6 (0.22)	2.4 (0.14)	1.5 (0.11)	0.99 (0.061)	2.8 (0.16)	0.037 (0.0064)
θ (deg)	6Li $d\sigma/d\Omega$ [b-sr $^{-1}$]	7Li $d\sigma/d\Omega$ [b-sr $^{-1}$]	8Li $d\sigma/d\Omega$ [b-sr $^{-1}$]	7Be $d\sigma/d\Omega$ [b-sr $^{-1}$]	9Be $d\sigma/d\Omega$ [b-sr $^{-1}$]	^{10}Be $d\sigma/d\Omega$ [b-sr $^{-1}$]
0.2 (0.2)	2.4 (0.55)	2.1 (0.86)	1.1 (0.34)	4.2 (0.56)	2 (0.79)	4.2 (1.2)
0.6 (0.2)	3.2 (0.31)	3.4 (0.85)	0.38 (0.059)	3 (0.26)	2.6 (0.56)	2.7 (0.71)
1 (0.2)	3.1 (0.4)	3.1 (0.71)	0.36 (0.068)	2.8 (0.18)	2 (0.35)	1.8 (0.42)
1.4 (0.2)	2.8 (0.37)	2.1 (0.57)	0.38 (0.068)	2.3 (0.16)	1.5 (0.25)	0.98 (0.21)
1.8 (0.2)	2.2 (0.3)	1.3 (0.41)	0.4 (0.095)	1.8 (0.1)	0.83 (0.12)	0.63 (0.12)
2.2 (0.2)	1.7 (0.31)	0.9 (0.38)	0.31 (0.078)	1.3 (0.078)	0.7 (0.066)	0.11 (0.058)
2.6 (0.2)	1 (0.22)	0.9 (0.23)	0.037 (0.027)	0.93 (0.054)	0.21 (0.045)	0.18 (0.034)
3 (0.2)	0.9 (0.23)	0.72 (0.17)	0.021 (0.047)	0.6 (0.036)	0.1 (0.017)	0.1 (0.037)
3.4 (0.2)	0.3 (0.14)	0.76 (0.15)	0.0037 (0.025)	0.39 (0.024)	0.044 (0.011)	0.062 (0.03)
3.8 (0.2)	0.19 (0.068)	0.47 (0.063)	0.0036 (0.027)	0.28 (0.018)	0.03 (0.013)	0.036 (0.013)
4.2 (0.2)	0.14 (0.042)	0.31 (0.047)	0.018 (0.0085)	0.17 (0.012)	0.036 (0.0095)	0.0044 (0.0087)
4.6 (0.2)	0.1 (0.029)	0.19 (0.035)	0.0029 (0.0035)	0.11 (0.01)	0.026 (0.0063)	0.0051 (0.0014)
5 (0.2)	0.077 (0.015)	0.082 (0.012)	0.015 (0.0041)	0.045 (0.0044)	0.016 (0.0034)	0.0012 (0.00051)
θ (deg)	^{10}B $d\sigma/d\Omega$ [b-sr $^{-1}$]		^{11}B $d\sigma/d\Omega$ [b-sr $^{-1}$]			
0.2 (0.2)	0.14 (0.067)		11 (3.4)			
0.6 (0.2)	0.05 (0.032)		0.75 (2.8)			
1 (0.2)	0.13 (0.023)		3.9 (1.2)			
1.4 (0.2)	0.11 (0.05)		0.42 (0.9)			
1.8 (0.2)	0.13 (0.031)		1.7 (0.71)			
2.2 (0.2)	0.071 (0.026)		0.23 (0.13)			
2.6 (0.2)	0.079 (0.012)		0.18 (0.19)			
3 (0.2)	0.034 (0.0065)		0.23 (0.063)			
3.4 (0.2)	0.03 (0.0077)		0.11 (0.047)			
3.8 (0.2)	0.0088 (0.0048)		0.074 (0.011)			
4.2 (0.2)	0.0087 (0.0034)		0.038 (0.015)			
4.6 (0.2)	0.005 (0.0015)		0.011 (0.0036)			
5 (0.2)	0.0023 (0.0015)		0.0079 (0.002)			

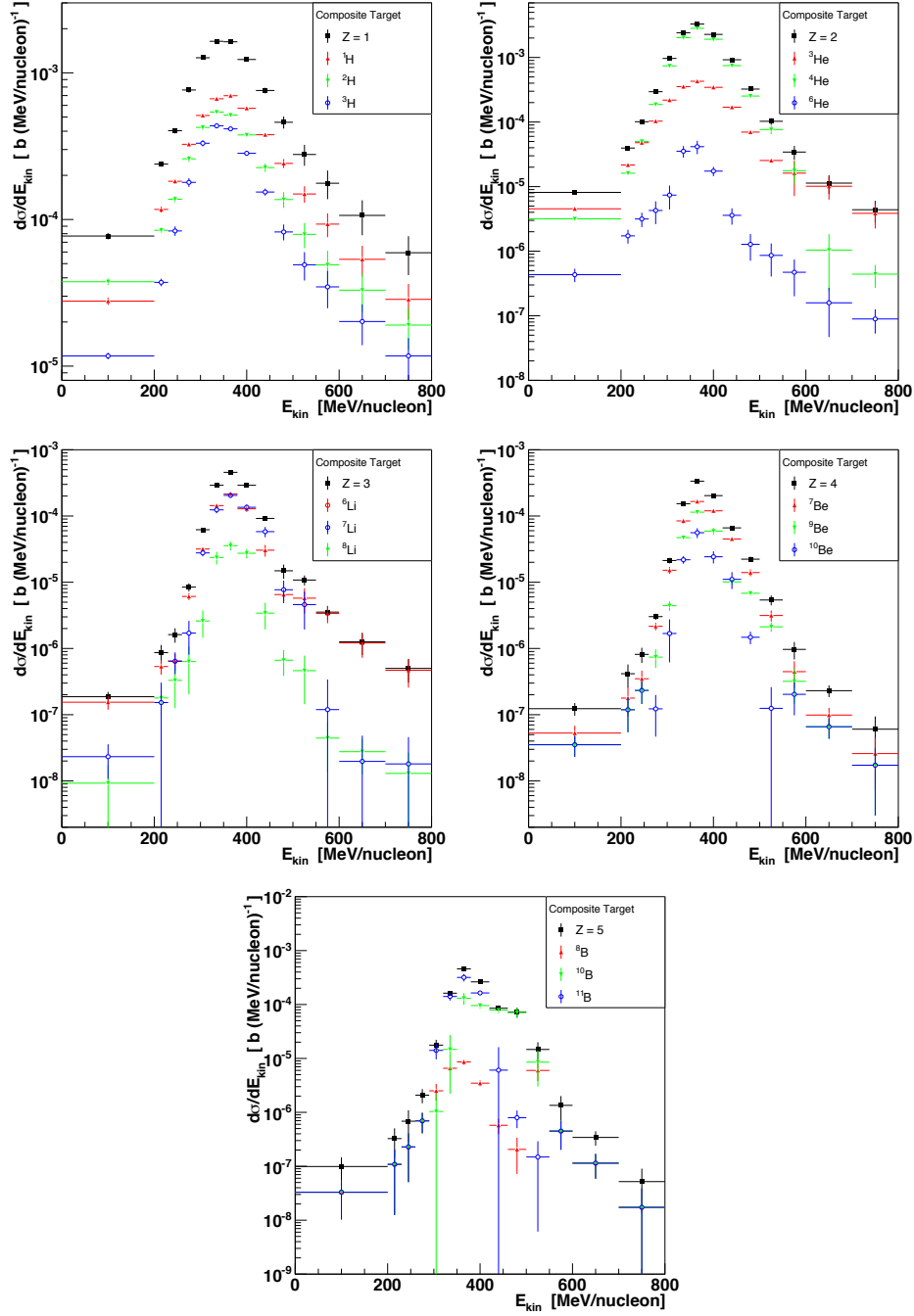


Figure A.4: Isotopic differential cross sections for the composite target, as a function of the fragment normalized kinetic energy, computed using Eq. 4.8 for fragments within the ALADIN angular acceptance ($\lesssim 6^\circ$). The results for each isotope are shown separately, together with their sum (in black squares). The total uncertainty (statistic and systematic added in quadrature) is shown.

APPENDIX A. ISOTOPIC CROSS SECTIONS

Table A.4: Cross sections as a function of the normalized kinetic energy E_{kin} [MeV/u] for the composite target. The values in parentheses represent the uncertainties.

E_{kin} (MeV/u)	1H $d\sigma/dE_{kin}$ [b·(MeV/u) ⁻¹]	2H $d\sigma/dE_{kin}$ [b·(MeV/u) ⁻¹]	3H $d\sigma/dE_{kin}$ [b·(MeV/u) ⁻¹]	3He $d\sigma/dE_{kin}$ [b·(MeV/u) ⁻¹]	4He $d\sigma/dE_{kin}$ [b·(MeV/u) ⁻¹]	6He $d\sigma/dE_{kin}$ [b·(MeV/u) ⁻¹]
100 (100)	2.73e-05 (1.59e-06)	3.71e-05 (1.87e-06)	1.16e-05 (6.03e-07)	4.49e-06 (1.84e-07)	3.18e-06 (1.22e-07)	4.15e-07 (1.01e-07)
215 (15)	1.14e-04 (5.56e-06)	8.31e-05 (3.44e-06)	3.66e-05 (2.18e-06)	2.16e-05 (8.83e-07)	1.63e-05 (8.41e-07)	1.98e-06 (4.19e-07)
245 (15)	1.81e-04 (6.32e-06)	1.36e-04 (6.66e-06)	8.30e-05 (6.20e-06)	4.74e-05 (1.84e-06)	4.98e-05 (2.21e-06)	3.58e-06 (7.91e-07)
275 (15)	3.26e-04 (8.66e-06)	2.60e-04 (1.25e-05)	1.77e-04 (1.21e-05)	1.03e-04 (3.78e-06)	1.83e-04 (9.74e-06)	5.38e-06 (1.64e-06)
305 (15)	5.14e-04 (1.26e-05)	4.24e-04 (1.76e-05)	3.29e-04 (1.58e-05)	2.17e-04 (7.80e-06)	7.21e-04 (4.50e-05)	9.28e-06 (2.96e-06)
335 (15)	6.66e-04 (1.59e-05)	5.40e-04 (1.67e-05)	4.33e-04 (1.13e-05)	3.48e-04 (1.27e-05)	1.99e-03 (8.56e-05)	3.26e-05 (7.19e-06)
365 (15)	6.99e-04 (1.50e-05)	5.17e-04 (1.46e-05)	4.17e-04 (7.33e-06)	4.27e-04 (1.21e-05)	2.81e-03 (5.95e-05)	3.81e-05 (9.70e-06)
400 (20)	5.74e-04 (1.19e-05)	3.81e-04 (1.28e-05)	2.86e-04 (6.54e-06)	3.47e-04 (8.87e-06)	1.93e-03 (3.55e-05)	1.72e-05 (2.84e-06)
440 (20)	3.83e-04 (1.15e-05)	2.30e-04 (1.45e-05)	1.57e-04 (8.31e-06)	1.72e-04 (3.88e-06)	7.53e-04 (1.41e-05)	3.45e-06 (1.02e-06)
480 (20)	2.46e-04 (1.70e-05)	1.42e-04 (1.68e-05)	8.48e-05 (1.02e-05)	7.05e-05 (2.10e-06)	2.51e-04 (1.67e-05)	1.02e-06 (5.66e-07)
525 (25)	1.56e-04 (1.94e-05)	8.23e-05 (1.54e-05)	5.26e-05 (1.08e-05)	2.54e-05 (1.48e-06)	7.52e-05 (1.12e-05)	1.25e-06 (4.55e-07)
575 (25)	9.77e-05 (1.72e-05)	5.21e-05 (1.22e-05)	3.70e-05 (9.89e-06)	2.44e-05 (9.03e-06)	9.02e-06 (6.71e-06)	7.01e-07 (2.71e-07)
650 (50)	5.76e-05 (1.27e-05)	3.57e-05 (9.69e-06)	2.18e-05 (6.26e-06)	9.74e-06 (3.85e-06)	7.61e-07 (7.98e-07)	2.45e-07 (1.12e-07)
750 (50)	3.11e-05 (7.82e-06)	2.02e-05 (6.09e-06)	1.29e-05 (3.78e-06)	3.71e-06 (1.61e-06)	5.27e-07 (1.70e-07)	9.43e-08 (3.62e-08)
E_{kin} (MeV/u)	6Li $d\sigma/dE_{kin}$ [b·(MeV/u) ⁻¹]	7Li $d\sigma/dE_{kin}$ [b·(MeV/u) ⁻¹]	8Li $d\sigma/dE_{kin}$ [b·(MeV/u) ⁻¹]	7Be $d\sigma/dE_{kin}$ [b·(MeV/u) ⁻¹]	9Be $d\sigma/dE_{kin}$ [b·(MeV/u) ⁻¹]	^{10}Be $d\sigma/dE_{kin}$ [b·(MeV/u) ⁻¹]
100 (100)	1.77e-07 (3.52e-08)	1.44e-08 (1.25e-08)	1.37e-08 (8.18e-09)	5.40e-08 (1.54e-08)	3.60e-08 (1.21e-08)	3.60e-08 (1.21e-08)
215 (15)	4.93e-07 (1.32e-07)	5.28e-08 (1.52e-07)	1.95e-07 (7.91e-08)	1.94e-07 (8.43e-08)	1.29e-07 (6.45e-08)	1.29e-07 (6.45e-08)
245 (15)	7.63e-07 (1.88e-07)	6.57e-07 (2.32e-07)	4.88e-07 (2.05e-07)	3.67e-07 (1.14e-07)	2.45e-07 (8.75e-08)	2.45e-07 (8.75e-08)
275 (15)	6.10e-06 (7.15e-07)	7.76e-07 (9.01e-07)	1.13e-06 (4.32e-07)	2.20e-06 (2.82e-07)	8.88e-07 (2.29e-07)	4.92e-08 (7.60e-08)
305 (15)	3.01e-05 (2.41e-06)	2.72e-05 (3.04e-06)	1.62e-06 (1.15e-06)	1.44e-05 (1.81e-06)	4.81e-06 (7.13e-07)	1.01e-06 (1.07e-06)
335 (15)	1.37e-04 (5.79e-06)	1.26e-04 (1.38e-05)	2.01e-05 (5.07e-06)	8.27e-05 (6.55e-06)	4.54e-05 (3.36e-06)	2.34e-05 (2.86e-06)
365 (15)	2.03e-04 (1.01e-05)	2.02e-04 (1.67e-05)	3.62e-05 (5.28e-06)	1.66e-04 (9.64e-06)	1.13e-04 (6.10e-06)	5.97e-05 (9.50e-06)
400 (20)	1.35e-04 (1.31e-05)	1.31e-04 (1.38e-05)	2.96e-05 (4.50e-06)	1.24e-04 (6.45e-06)	6.50e-05 (6.80e-06)	1.99e-05 (5.05e-06)
440 (20)	3.30e-05 (6.08e-06)	5.30e-05 (1.02e-05)	3.75e-06 (1.48e-06)	4.58e-05 (2.41e-06)	9.90e-06 (9.31e-07)	1.22e-05 (3.16e-06)
480 (20)	6.77e-06 (1.31e-06)	7.94e-06 (2.86e-06)	8.68e-07 (2.80e-07)	1.31e-05 (1.68e-06)	6.78e-06 (5.33e-07)	1.59e-06 (3.19e-07)
525 (25)	6.09e-06 (2.38e-06)	4.89e-06 (2.66e-06)	5.58e-07 (3.18e-07)	2.84e-06 (6.00e-07)	2.26e-06 (3.43e-07)	5.31e-08 (1.36e-07)
575 (25)	3.95e-06 (9.69e-07)	1.14e-04 (2.21e-07)	4.07e-08 (3.07e-08)	3.78e-07 (1.94e-07)	2.52e-07 (1.74e-07)	2.52e-07 (1.05e-07)
650 (50)	1.50e-06 (4.89e-07)	2.05e-05 (2.85e-08)	2.34e-08 (1.51e-08)	1.02e-07 (2.82e-08)	6.79e-08 (2.26e-08)	6.79e-08 (2.26e-08)
750 (50)	5.87e-07 (2.13e-07)	8.04e-06 (2.78e-08)	1.71e-08 (1.37e-08)	3.32e-08 (1.85e-08)	2.22e-08 (1.43e-08)	2.22e-08 (1.43e-08)
E_{kin} (MeV/u)	8Bo $d\sigma/dE_{kin}$ [b·(MeV/u) ⁻¹]		^{10}Bo $d\sigma/dE_{kin}$ [b·(MeV/u) ⁻¹]		^{11}Bo $d\sigma/dE_{kin}$ [b·(MeV/u) ⁻¹]	
100 (100)	3.29e-08 (2.27e-08)		3.29e-08 (2.27e-08)		3.29e-08 (2.27e-08)	
215 (15)	1.10e-07 (9.62e-08)		1.10e-07 (9.62e-08)		1.10e-07 (9.62e-08)	
245 (15)	2.50e-07 (1.78e-07)		2.50e-07 (1.78e-07)		2.50e-07 (1.78e-07)	
275 (15)	7.67e-07 (2.85e-07)		7.67e-07 (2.85e-07)		7.67e-07 (2.85e-07)	
305 (15)	2.71e-06 (8.63e-07)		5.53e-07 (1.18e-06)		1.41e-05 (4.48e-06)	
335 (15)	6.69e-06 (5.86e-07)		1.22e-05 (1.25e-05)		1.43e-04 (2.26e-05)	
365 (15)	8.92e-06 (9.56e-07)		1.49e-04 (3.22e-05)		3.02e-04 (5.02e-05)	
400 (20)	3.74e-06 (4.34e-07)		1.04e-04 (1.07e-05)		1.64e-04 (1.25e-05)	
440 (20)	6.28e-07 (1.82e-07)		8.54e-05 (9.38e-06)		7.44e-07 (1.01e-05)	
480 (20)	1.67e-07 (1.33e-07)		6.56e-05 (1.49e-05)		6.94e-07 (2.86e-07)	
525 (25)	5.75e-06 (2.18e-06)		6.96e-06 (5.52e-06)		2.39e-07 (1.42e-07)	
575 (25)	4.22e-07 (2.47e-07)		4.22e-07 (2.47e-07)		4.22e-07 (2.47e-07)	
650 (50)	1.22e-07 (5.54e-08)		1.22e-07 (5.54e-08)		1.22e-07 (5.54e-08)	
750 (50)	1.88e-08 (2.14e-08)		1.88e-08 (2.14e-08)		1.88e-08 (2.14e-08)	

Bibliography

- [1] M. Durante and J. S. Loeffler, *Charged particles in radiation oncology*, Nat. Rev. Clin. Oncol. 7, 37–43 (2010).
- [2] W. Bragg, *On the α particles of radium and their loss of range in passing through various atom and molecules*, Philos. Mag. 10, 318-340 (1905).
- [3] D. Schardt et al., *Nuclear fragmentation of high-energy heavy-ion beams in water*, Adv. Space Res. 17, 87 (1996).
- [4] D. Thwaites, *Accuracy required and achievable in radiotherapy dosimetry: have modern technology and techniques changed our views?*, Journal of Physics: Conference Series 444, 012006, (2013).
- [5] M. Durante and F. A. Cucinotta, *Physical basis of radiation protection in space travel*, Rev. Mod. Phys., vol. 83, (2011).
- [6] M. A. Clemens et al., *The effects of nuclear fragmentation models on single event effect prediction*, IEEE Trans. Nucl. Sci., vol. 56, no. 6, 3158–3164, (2009).
- [7] M. Krämer, *Swift ions in radiotherapy – Treatment planning with TRiP98*, Nuclear Instruments and Methods in Physics Research B 267, 989–992, (2009).
- [8] M. Krämer and M. Durante, *Ion beam transport calculations and treatment plans in particle therapy*, Eur. Phys. J. D 60, 195–202 (2010).
- [9] L. Sihver and D. Mancusi, *Present status and validation of HIBRAC*, Radiation Measurements 44, 38–46, (2009).

BIBLIOGRAPHY

- [10] F. Sommerer et al., *Investigating the accuracy of the FLUKA code for transport of therapeutic ion beams in matter*, Physics in Medicine and Biology 51, 4385, (2006).
- [11] J. Allison et al., *Geant4 developments and applications*, IEEE Transactions on Nuclear Science NS-53, 270, (2006).
- [12] M. Hultqvist et al., *Evaluation of nuclear reaction cross-sections and fragment yields in carbon beams using the SHIELD-HIT Monte Carlo code. Comparison with experiments*, Physics in Medicine and Biology 57, 4369, (2012).
- [13] T. T. Böhlen et al., *Benchmarking nuclear models of FLUKA and GEANT4 for carbon ion therapy*, Physics in Medicine and Biology 55(19), 5833, (2010).
- [14] B. Braunn et al., *Comparisons of hadrontherapy-relevant data to nuclear interaction codes in the Geant4 toolkit*, Journal of Physics: Conference Series 420, 012163 (2013).
- [15] D. Schardt, T. Elsasser, D. Schulz-Ertner, *Heavy-ion tumor therapy: Physical and radiobiological benefits*, Rev.Mod.Phys, Vol. 82, No. 1, January-March 2010 383-425 (2010).
- [16] J. H. Heinbockel et al., *Comparison of the transport codes HZETRN, HETC and FLUKA for galactic cosmic rays*, Advances in Space Research 47, 1079, (2011).
- [17] J. W. Norbury, J. Miller et al., *Review of Nuclear Physics Experiments for Space Radiation*, NASA/TP-2011-217179, (2011).
- [18] M. De Napoli et al., *Carbon fragmentation measurements and validation of the GEANT4 nuclear reaction models for hadrontherapy*, Physics in Medicine and Biology 57, 7651-7671, (2012).
- [19] J. Dudouet et al., *Double-differential fragmentation cross-section measurements of 95 MeV/nucleon ^{12}C beams on thin targets for hadron therapy*, Physical Review C 88, 024606, (2013).

BIBLIOGRAPHY

- [20] J. Dudouet et al., *Zero-degree measurements of ^{12}C fragmentation at 95 MeV/nucleon on thin targets*, Phys. Rev. C 89, 064615 (2014).
- [21] R. Pleskac et al., *The FIRST experiment at GSI*, Nucl. Instrum. Methods Phys. Res. A 678, 130, (2012).
- [22] G. Kraft, *Tumor Therapy with Heavy Charged Particles*, Progress in Particle and Nuclear Physics 45, S473-S544, (2000).
- [23] R. R. Wilson, *Radiological Use of Fast Protons*, Radiology 47, 487-491 (1946).
- [24] M. Scholz, *Heavy ion tumor therapy*, Nuclear Instruments and Methods in Physics Research B 161-163, 76-82, (2000).
- [25] ICRU report 51: *Quantities and Units in Radiation Protection Dosimetry*, International Commission on Radiation Units and Measurements, Bethesda, MD (1993).
- [26] W. R. Leo, *Techniques for Nuclear and Particle Physics Experiments*, Springer-Verlag (1987).
- [27] D. H. Perkins, *Introduction to High Energy Physics*, Cambridge University Press (2000).
- [28] R. C. Fernow, *Introduction to experimental particle physics*, Cambridge University Press (1986).
- [29] H. Bichsel, D. E. Groom, S:R. Klein *Passage of particles through matter*, PDG revised January (2010).
- [30] U. Fano, *Penetration of protons, α particles and mesons*, Annu. Rev. Nucl. Sci. 13, 1-66 (1963).
- [31] H. Bichsel, T. Hiraoka, *Energy Loss of 70 MeV protons in elements*, Nucl. Instrum. Methods. Phys. Res. B 66, 345-351 (1992).

BIBLIOGRAPHY

- [32] H. Bichsel, T. Hiraoka, K. Omata *Aspect of fast-ion dosimetry*, Radiat. Res. 153, 208-213 (2000).
- [33] Y. Kumazaki, et al., *Determination of the mean excitation energy of water from proton beam ranges*, Radiat. Meas. 42, 1683-1691 (2007).
- [34] H. Paul, *The mean ionization potential of water, and its connection to the range of energetic carbon ions in water*, Nucl. Instrum. Methods Phys. Res. B 255, 435-437 (2007).
- [35] D. Schardt et al, *Precision Bragg-curve measurements for light-ion beams in water*, GSI-Report 2008-1 (GSI Scientific Report 2007). p.373 (unpublished) (2008).
- [36] B. Rossi and K. Greisen, *Cosmic-Ray Theory*, Rev. Mod Phys. Vol. 13, 240-309, (1941).
- [37] Y. S. Tsai, *Pair production and bremsstrahlung of charged leptons*, Rev. Mod Phys. 46, 815-851 (1974).
- [38] V. L. Highland, *Some practical remarks on multiple scattering*, Nucl. Instrum. Methods Phys. Res. 129, 497-499 (1975).
- [39] H. A. Bethe, *Moliere's Theory of Multiple Scattering*, Physical Review, Vol. 89, N. 6, 1256, (1953).
- [40] R. Serber, *Nuclear Reactions at High Energy*, Phys. Rev. 72, 1114, (1947).
- [41] J. J. Gaimard and K. H. Schmidt, *A reexamination of the abrasion-ablation model for the description of the nuclear fragmentation reaction*, Nuclear Physics A531, 709-745, (1991).
- [42] J. Hufner, K. Schafer and B. Schurmann, *Abrasion-ablation in reactions between relativistic heavy ions*, Phys. Rev. C12, 1888, (1975).
- [43] X. Campi and J. Hufner, *Nuclear spallation-fragmentation reactions induced by high-energy projectiles*, Phys. Rev. C24, 2199, (1981).

BIBLIOGRAPHY

- [44] V. Weisskopf, *Statistics and nuclear reactions*, Phys. Rev. 52, 295–303, (1937).
- [45] A. Ferrari, P. R. Sala, A. Fassò, J. Ranft, *FLUKA: A Multi Particle Transport Code*, Technical Report CERN-2005-10, INFN/TC05/11, SLAC-R-773, (2005).
- [46] G. Battistoni et al., *The FLUKA code: description and benchmarking*, Proc. Hadronic Shower Simulation Workshop, AIP Conf. Proc. vol 896, pp 31–49, (2007).
- [47] K. Niita et al., *PHITS: Particle and Heavy Ion Transport Code System Version 2.23* (JAEA-Data/code 2010-022), (2010).
- [48] S. Agostinelli et al., *G4—a simulation toolkit*, Nucl. Instrum. Methods A 506 250–303, (2003).
- [49] J. S. Hendricks et al., *MCNPX 2.6.0 Extensions*, LA-UR-08-2216, (2008).
- [50] I. Gudowska et al., *Ion beam transport in tissue-like media using the Monte Carlo code SHIELD-HIT*, Phys. Med. Biol. 49 1933–58, (2004).
- [51] A. Ferrari and P. R. Sala, *Proceeding of Workshop on Nuclear Reaction Data and Nuclear Reactors Physics*, Design and Safety (Trieste, April 1996) ed A Gandini and G Reffo 2 424, (1998).
- [52] A. Ferrari, P. R. Sala, *Nuclear reactions in Monte Carlo codes*, Radiat. Prot. Dosim. 99 (1-4), (2002).
- [53] A. Fassò et al., *The physics models of FLUKA: status and recent developments*, arXiv:hep-ph/0306267v1, (2003).
- [54] P. R. Sala et al., *The physics of the FLUKA code: Recent developments*, Advanced in Space Research 40, 1339-1349, (2007).
- [55] T. T. Böhlen, *Monte Carlo particle transport codes for ion beam therapy treatment planning*, PhD thesis, Stockholm University, (2012).

BIBLIOGRAPHY

- [56] A. Capella, U. Sukhatme, C. I. Tan and J. Tran Thanh Van, *Dual Parton Model*, Phys. Rep. 236 225, (1994).
- [57] R. J. Glauber and G. Matthiae, *High-energy scattering of protons by nuclei*, Nucl. Phys. B21, 135 (1970).
- [58] V. N. Gribov, *Glauber corrections and the interaction between high-energy hadrons and nuclei* Sov. Phys. JETP 29, N.3, 483 (1969).
- [59] V. N. Gribov, *Interaction of gamma quanta and electrons with nuclei at high energies* Sov. Phys. JETP 30, N.4, 709 (1970).
- [60] M. Blann, *Hybrid model for pre-equilibrium decay in nuclear reactions* Phys. Rev. Lett. 27, 337-340 (1971).
- [61] V. Weisskopf, D. H. Ewing, *On the yield of nuclear reactions with heavy elements*, Phys. Rev. 57, 472–485, (1940).
- [62] N. Bohr, J. A. Wheeler, *The mechanism of nuclear fission*, Phys. Rev. 56, 426–450, (1939).
- [63] M. Epherre, E. Gradsztajn, R. Klapisch, H. Reeves, *Comparison between the evaporation and the break-up models of nuclear de-excitation*, Nucl. Phys. A 139 (3), 545–553, (1969).
- [64] E. Fermi, *High energy nuclear events. Progress of Theoretical Physics*, 5, N.4, 570–583, (1950).
- [65] M. R. Bhat, *Procedures manual for the evaluated nuclear structure data file*, Tech. Rep. BNL-NCS-40503 INFORMAL REPORT (Brookhaven: The National Nuclear Data Center Brookhaven National Laboratory), (1987).
- [66] L. Sihver et al., *A comparison of total reaction cross section models used in FLUKA, GEANT4 and PHITS*, Proceedings IEEE Aerospace 2012, Big Sky, Montana, March 3-10, DOI: 10.1109/AERO.2012.6187014, (2012).

BIBLIOGRAPHY

- [67] R. K. Triparthi et al., *Accurate universal parameterization of absorption cross sections*, Nuclear Instruments and Methods in Physics Research B 117, 347-349, (1996).
- [68] R. K. Triparthi et al., *Accurate universal parameterization of absorption cross sections II - neutron absorption cross sections*, Nuclear Instruments and Methods in Physics Research B 129, 11-15, (1997).
- [69] R. K. Triparthi et al., *Accurate universal parameterization of absorption cross sections III - light systems*, Nuclear Instruments and Methods in Physics Research B 155, 349-356, (1999).
- [70] J. Aichelin, *Quantum Molecular Dynamics. A dynamical microscopic n-body approach to investigate fragment formation and the nuclear equation of state in heavy ion collisions*, Phys. Rep. 202 (5-6), 233-360, (1991).
- [71] G. Bertsch, S. D. Gupta, *A guide to microscopic models for intermediate energy heavy ion collisions*, Phys. Rep. 160 (4), 189-233, (1988).
- [72] V. Andersen et al., *The FLUKA code for space applications: recent developments*, Adv. Space Res. 34 1302-10, (2004).
- [73] H. Sorge et al., *Relativistic Quantum Molecular Dynamics Approach to Nuclear Collisions at Ultrarelativistic Energies*, Nuclear Physics A498 567c-576c (1989).
- [74] E. Gadioli et al., *Boltzmann master equation theory of angular distributions in heavy-ion reactions*, Nucl. Phys. A 643, 15 (1998).
- [75] F. Cerutti et al., *Contributions of complete fusion and break-up-fusion to intermediate mass fragment production in the low energy interaction of ^{12}C and ^{27}Al* , Nuclear Physics A 797, 1-32, (2007).
- [76] E. Gadioli et al., *Excitation functions of residues in the interaction of ^{12}C with ^{103}Rh up to an incident energy of 400 MeV*, Nucl. Phys. A 753, 29, (2005).

BIBLIOGRAPHY

- [77] E. Gadioli et al., *Excitation functions of evaporation residues in the interaction of ^{16}O with ^{103}Rh at incident energies up to 400 MeV*, Eur. Phys. J. A 28, 193, (2006).
- [78] F. Cerutti et al., *Low energy nucleus–nucleus reactions: the BME approach and its interface with FLUKA*, Proc. 11th Int. Conf. on Nuclear Reaction Mechanism (Varenna, Italy, 12–16 June) pp 507–11, (2006).
- [79] F. Cerutti et al., *Carbon induced reactions at low incident energies*, Journal of Physics: Conference Series 41, 212–218, (2006).
- [80] G. D. Westfall et al., *Fragmentation of relativistic ^{56}Fe* , Phys. Rev. C, Vol.19, N.4, (1979).
- [81] S. Kox et al., *Trends of total reaction cross sections for heavy ion collisions in the intermediate energy range*, Physical Review C 35, 1678, (1987).
- [82] W. R. Webber, J. C. Kish, and D. A. Schrier, *Total charge and mass changing cross sections of relativistic nuclei in hydrogen, helium, and carbon targets*, Phys. Rev. C, Vol.41, N.2 (1990).
- [83] I. Schall et al., *Charge-changing nuclear reactions of relativistic light-ion beams ($5 \leq Z \leq 10$) passing through thick absorbers*, Nuclear Instruments and Methods in Physics Research Section B, 117, 221–234, (1996).
- [84] B. Alpat et al., *Total and Partial Fragmentation Cross-Section of 500 MeV/nucleon Carbon Ions on Different Target Materials*, IEEE Transactions on Nuclear Science, Vol 60, N.6 (2013).
- [85] C. Zeitlin et al., *Fragmentation cross sections of 600 MeV/amu Ne-20 on elemental targets*, Phys. Rev. C, 64, 075007–075027, (2001).
- [86] C. Zeitlin et al., *Fragmentation cross sections of 290 and 400 MeV/nucleon ^{12}C beams on elemental targets*, Phys. Rev. C, 76, 014911 (2007).

BIBLIOGRAPHY

- [87] A. N. Golovchenko et al., *Total charge-changing and partial cross-section measurements in the reactions of ~ 110 – 250 MeV/nucleon ^{12}C in carbon, paraffin, and water*, Phys. Rev. C 66, 014609, (2002).
- [88] W. R. Webber, J. C. Kish, and D. A. Schrier, *Individual charge changing fragmentation cross sections of relativistic nuclei in hydrogen, helium, and carbon targets*, Phys. Rev. C, Vol.41, N.2, (1990).
- [89] W. R. Webber, J. C. Kish, and D. A. Schrier, *Individual isotopic fragmentation cross sections of relativistic nuclei in hydrogen, helium, and carbon targets*, Phys. Rev. C, Vol.41, N.2, (1990).
- [90] N. Matsufuji et al., *Influence of fragment reactions of relativistic heavy charged particles on heavy-ion radiotherapy*, Phys. Med. Biol. 48, 1605 (2003).
- [91] T. Toshito et al., *Measurements of total and partial charge-changing cross sections for 200 to 400 MeV/nucleon C-12 on water and polycarbonate*, Physical Review C, 75, 054606, (2007).
- [92] K. Gunzert-Marx, D. Schardt and R. S. Simon, *Fast neutrons produced by nuclear fragmentation in treatment irradiations with ^{12}C beam* Radiat. Prot. Dosim. 110 595–600, (2004).
- [93] K. Gunzert-Marx, H. Iwase, D. Schardt and R. S. Simon, *Secondary beam fragments produced by 200 MeV u^{-1} ^{12}C ions in water and their dose contributions in carbon ion therapy*, New Journal of Physics 10, 075003, (2008).
- [94] E. Haettner et al., *Experimental fragmentation studies with C-12 therapy beams*, Radiation Protection Dosimetry, 122, 485–487, (2006).
- [95] E. Haettner et al., *Experimental study of nuclear fragmentation of 200 and 400 MeV/u C-12 ions in water for applications in particle therapy*, Physics in Medicine and Biology, 58, 8265–8280, (2013).
- [96] T. Koi, *New native QMD code in Geant4*, IEEE Nuclear Science Symposium Conf. Record. (2008).

BIBLIOGRAPHY

- [97] G. Folger et al., *The Binary Cascade: nucleon nuclear reactions*, Eur. Phys. J.A 21, 407–17, (2004).
- [98] GEANT4, *Geant4 Physics Reference Manual version 9.3*, chapters 26, 29, 30, 31, 32, 33, (2009).
- [99] J. Dudouet, *Benchmarking GEANT4 nuclear models for hadron therapy with 95 MeV/nucleon carbon ions*, Phys. Rev. C 89, 054616 (2014).
- [100] M. Golovkov et al., *Fragmentation of 270 AMeV carbon ions in water*, Advances in Hadrontherapy, International Congress Series No. 1144 (Elsevier Science, New York), pp. 316–324, (1997).
- [101] A. Boudard et al., *New potentialities of the Liege intranuclear cascade model for reactions induced by nucleons and light charged particles*, Phys. Rev. C 87, 014606, (2013).
- [102] N. Matsufuji et al., *Spatial fragment distribution from a therapeutic pencil-like carbon beam in water*, Phys. Med. Biol. 50, 3393–3403, (2005).
- [103] A. Mairani, *Nucleus-nucleus interaction modelling and applications in ion therapy treatment planning*, Scientifica Acta 1, N.1, 129–132 (2007).
- [104] A. Mairani, *Nucleus-Nucleus interaction modelling and applications in ion therapy treatment planning*, PhD Thesis, Univesity of Pavia, (2007).
- [105] V. Patera, *Nuclear physics experiment for hadron therapy application*, Nuovo Cimento C 34 (6)(2011).
- [106] Z. Abou-Haidar et al., *Performance of upstream interaction region detectors for the FIRST experiment at GSI*, JINST, 7, P02006, (2012).
- [107] R. Rescigno et al., *Performance of the reconstruction algorithms of the FIRST experiment pixel sensors vertex detector*, Nucl. Instrum. Methods Phys. Res. A, 767, 34-40, (2014).

BIBLIOGRAPHY

- [108] E. Spiriti et al., *The FIRST experiment: interaction region and MAPS vertex detector*, Nucl. Phys. (Proc. Suppl.) B, 215, 157161, (2011).
- [109] A. Schuttauf et al., *Universality of spectator fragmentation at relativistic bombarding energies*, Nuclear Physics A607, 457, (1996).
- [110] R. Introzzi et al., *Experiment FIRST: Fragmentation of ^{12}C Beam at 400 MeV/u*, DOI:10.1109/NSSMIC.2013.682944, Conference: C13-10-26, (2013).
- [111] G. Bauer et al., *A multiple sampling time projection ionization chamber fragmentation tracking and charge measurement*, Nuclear Instruments and Methods in Physics Research A, 386, 249-253, (1997).
- [112] B. Golosio et al., *The FIRST experiment for nuclear fragmentation measurements at GSI*, 2011 IEEE Nuclear Science Symposium Conference Record, (2011).
- [113] A. Paoloni et al., *The upstream detectors of the FIRST experiment at GSI*, Physics Procedia, 37, 1466–1472, (2012).
- [114] <http://www.iphc.cnrs.fr/-CMOS-ILC-.html>
- [115] C. Hu-Guo et al., *First reticule size MAPS with digital output and integrated zero suppression for the EUDET-JRA1 beam telescope*, Nuclear Inst. and Methods in Physics Research, Vol. 623, p. 480-482, (2010.)
- [116] D. J. Jackson, *A topological vertex reconstruction algorithm for hadronic jets*, Nuclear Inst. and Methods in Physics Research A, Vol. 388, p. 247-253, (1997).
- [117] H. G. Essel, N. Kurz, IEEE Transactions on Nuclear Science NS-47 (2), 337, (2000).
- [118] R. Brun et.al., *Root an object oriented data analysis farmework*, Nuclear Instruments and Methods in Physics Research Section A: Accelerators, Spectrometers, Detectors and Associated Equipment, 389, 81–86, (1996).

BIBLIOGRAPHY

- [119] J. B. Birks, *Scintillations from Organic Crystals: Specific Fluorescence and Relative Response to Different Radiations*, Proceeding of the Physical Society, Sec. A, 874-877 (1951).
- [120] S. Schmitt, *TUnfold: an algorithm for correcting migration effects in high energy physics*, JINST 7, T10003, (2012) [arXiv:1205.6201].
- [121] K. S. Cranmer, *Kernel Estimation in High-Energy Physics*, Computer Physics Communications 136:198-207,2001. e-Print Archive: hep ex/0011057
- [122] W. Verkerke and D. P. Kirkby, *The RooFit toolkit for data modeling*, rXiv:physics/0306116.
- [123] M. Agnello et al., *The FINUDA Collaboration Report*, INFN Report LNF-95/024, (1995).
- [124] E. Botta et al., *A twin amplifier for drift chambers readout*, Nuclear Instruments and Methods in Physics Research A 383, 566-571, (1996).
- [125] M. Agnello et al., *The measurement of the coordinate along the sense wire with decoupling capacitors*, Nuclear Instruments and Methods in Physics Research A 398, 167-172, (1997).
- [126] L. Busso et al., *A linear gate and transmitter for improving localization using the charge division method*, Nuclear Instruments and Methods in Physics Research A 485, 640-644, (2002).